UNIVERSITY OF ALBERTA

CAPACITY OF A COHERENCE MULTIPLEXED TELECOMMUNICATIONS SYSTEM

BY

DARREN ALEXANDER BLAIR

A thesis submitted to the Faculty of Graduate Studies and Research in partial fulfillment of the requirements for the degree of **Master Of Science.**

DEPARTMENT OF ELECTRICAL ENGINEERING

Edmonton, Alberta

SPRING 1991

The author has granted an irrevocable non-exclusive licence allowing the National Library of Canada to reproduce, loan, distribute or sell copies of his/her thesis by any means and in any form or format, making this thesis available to interested persons.

The author retains ownership of the copyright in his/her thesis. Neither the thesis nor substantial extracts from it may be printed or otherwise reproduced without his/her permission.

L'auteur a accordé une licence irrévocable et non exclusive permettant à la Bibliothèque nationale du Canada de reproduire, prêter, distribuer ou vendre des copies de sa thèse de quelque manière et sous quelque forme que ce soit pour mettre des exemplaires de cette thèse à la disposition des personnes intéressées.

L'auteur conserve la propriété du droit d'auteur qui protège sa thèse. Ni la thèse ni des extraits substantiels de celle-ci ne doivent être imprimés ou autrement reproduits sans son autorisation.

Canada

UNIVERSITY OF ALBERTA

RELEASE FORM

NAME OF AUTHOR: **Darren Alexander Blair**
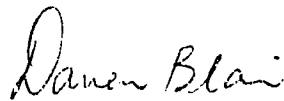
TITLE OF THESIS: **Capacity Of A Coherence Multiplexed**

Telecommunications System

DEGREE: **Master Of Science**

YEAR THIS DEGREE GRANTED: **Spring 1991**

#4 Huntington Hill

Edmonton, Alberta
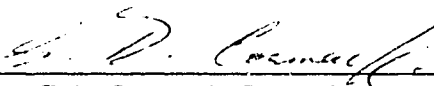
T6H 5S6

DATE: *April* 23 19 *91*

i
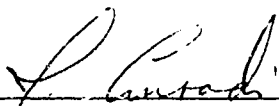
UNIVERSITY OF ALBERTA

FACULTY OF GRADUATE STUDIES AND RESEARCH

The undersigned certify that they have read, and recommend to the Faculty of Graduate Studies and Research for acceptance, a thesis entitled **CAPACITY OF A COHERENCE MULTIPLEXED TELECOMMUNICATIONS SYSTEM** submitted by **DARREN ALEXANDER BLAIR** in partial fulfillment of the requirements for the degree of **MASTER OF SCIENCE** in Electrical Engineering.

G.D. Cormack, Supervisor

J. Conradi, Internal Examiner

R.I. MacDonald, Internal Examiner

T.A. Marsland, External Examiner

Date: April 22 19 91

iii

DEDICATION

To my wife, Marianne,

who has always supported and encouraged me

and shared in my dreams.

ABSTRACT

A particular coherence multiplexing (CM) architecture, called the "extrinsic-reference ladder" (ERL) configuration is evaluated for its potential application in a "fiber to the home" (FTTH) broadband access system. A theoretical model is developed to predict the capacity of such a system and sections of the model are confirmed with measurements from an experimental two-channel system.

The effect of varying the optical power distribution within the system is studied and is found to have significant impact on system performance. Specifically, proper selection of the channel/reference power ratio is necessary to obtain optimum system performance. For systems with a large number of channels, performance of a power-optimized system can be substantially greater than that of a system with a channel/reference power ratio of unity.

The effect of differential length mismatches in the two fibers which connect the transmitter array to the receiver is studied. It is found that length mismatch has a significant effect on the system and may well impose the greatest limit on multiplexing capacity of an ERL CM system. It is determined that, for a given value of mismatch, there is an optimum value of laser linewidth which maximizes system performance and an analytic expression is derived for this optimum linewidth. Employment of a laser with a linewidth greater than this optimum value can seriously reduce the multiplexing capacity of the system.

While CM is considered for its feasibility in FTTH broadband access systems, it may also merit consideration for other applications where path length matching can be obtained with great accuracy. Namely, CM should be studied for application in areas such as computer backplanes and optical integrated circuits where there is tight control over system path lengths.

ACKNOWLEDGEMENTS

TABLE OF CONTENTS

LIST OF TABLES

LIST OF FIGURES

LIST OF ABBREVIATIONS

AM	Amplitude modulation
A/O	Acousto-optic
APD	Avalanche photodiode
AR	Anti-reflection
ASK	Amplitude shift keying
BER	Bit error rate
CM	Coherence multiplexing
CNR	Carrier to noise ratio
CNR_I	Carrier to interference noise ratio
CNR_{Rx}	Receiver carrier to noise ratio
CNR_{Tx}	Transmitter carrier to noise ratio
DFB	Distributed feedback
DSB	Double sideband
ERL	Extrinsic reference ladder
FDM	Frequency division multiplexing
FTTH	Fiber to the home
IF	Intermediate frequency
IRL	Intrinsic reference ladder
LED	Light emitting diode
LI	Light intensity vs. current
LC	Large carrier
LO	Local oscillator
LPF	Low pass filter
NA	Numerical aperature
NRZ	Non-return-to-zero

OOK	On-off keying
OPD	Optical path difference
PDF	Probability density function
PIN	Positive-intrinsic-negative photodiode
PSD	Power spectral density
RBW	Resolution bandwidth
RF	Radio frequency
RIN	Relative intensity noise
SCM	Subcarrier multiplexing
SLD	Superluminescent diode
SMF	Single-mode fiber
SOP	State of polarization
SNR	Signal to noise ratio
TEC	Thermo-electric cooler
WDM	Wavelength division multiplexing

1. INTRODUCTION

At present, only a fraction of the potential bandwidth of single mode optical fiber is being used in communication systems. Conventional multiplexing techniques typically combine signals electrically and drive the transmitting laser with the composite signal. Examples of this technique are subcarrier multiplexing (SCM), which is typically used for analog signals, and time-division-multiplexing (TDM) which is used for digital signals.

SCM involves direct modulation of an optical source with an electrical signal which has already been frequency-division-multiplexed using conventional electrical means. Total system bandwidth of this technique is typically limited by the modulation bandwidth of the laser and the electrical bandwidth of the photodetector and receiver circuits. In general, the electrical bandwidth of the transmitter and receiver components must be equal to or greater than that of the composite FDM signal.

Other techniques such as wavelength division multiplexing (WDM) split the optical spectrum into bands of operation. Present WDM techniques use very coarse frequency band allocation, exhibiting poor spectral efficiency. Coherent techniques using narrowband optical FDM are possible but require expensive, narrow linewidth lasers at the transmitters and receivers.

A relatively new coherent technique, called coherence multiplexing (CM), is not limited by the speed of the electronics nor does it require a local oscillator laser at the receiver. In addition, CM is inherently insensitive to the stability of the laser transmitter source and does not require a narrow linewidth at the head end of the system. CM also allows simultaneous transmission of channels (analog or digital) without synchronization.

CM takes advantage of the finite coherence of an optical source to perform multiplexing and demultiplexing in the optical domain using interferometric techniques.

Since CM uses a truly optical technique, the bandwidth of the opto-electronic and electrical components of the CM receiver only needs to be as large as that of a single channel and not the entire multiplexed bandwidth. As a result, the capacity of the system is theoretically limited only by the optical bandwidth, not the electrical bandwidth of the system.

CM was originally proposed as a method for multiplexing the signals from arrays of interferometric fiber sensors [1]. While CM seemed to be a viable technology for low-speed sensor systems, many were doubtful that it would ever be viable for high speed communications systems. Within the past few years, however, interest has grown in applying the CM technique to telecommunications systems [2, 3]. Some of the original issues have essentially been solved but a number of problems still remain. This thesis examines a particular CM architecture, called the "extrinsic reference ladder" (ERL) configuration, for its feasibility as a multiplexing method in a fiber-to-the-home (FTTH) broadband access system. In particular, two specific areas are addressed, that of optical power optimization and differential fiber path length mismatch effects.

The original work of Healey [4] suggested that the capacity of a CM system of the type analyzed in his paper would be severely limited by the large number of signal crossproducts that occur within such a system. Preliminary work for this thesis suggested that by adopting a slightly different CM architecture and optimizing the optical power distribution within the system, capacity of a multi-channel CM system could be substantially increased. The results and conclusions from this study of power optimization are presented in this thesis.

While it has been generally accepted that an ERL architecture potentially offers the most multiplexing capacity of all reported CM configurations [5], one significant issue has not been previously resolved. In the ERL architecture, two optical fibers are needed to connect the transmitter array to any given receiver. The CM technique requires that the path lengths of these two fibers be carefully matched and it has long been

suspected that differential mismatches in these lengths would degrade the performance of the system. This problem is explored in this thesis and the effects of mismatch are characterized.

Cormack and Waschuk [6] have examined a large number of broadband access optical fiber network topologies as options to replace the existing access network. In all, 77 different systems were analyzed with emphasis placed on coherent systems. Point-to-point coherent and direct detection schemes were evaluated as well as coherent and non-coherent broadband access systems. One particular coherent broadband access system which could be the "system of the future" is denoted by Cormack and Waschuk as *System 103* and is shown in Figure 1.1.
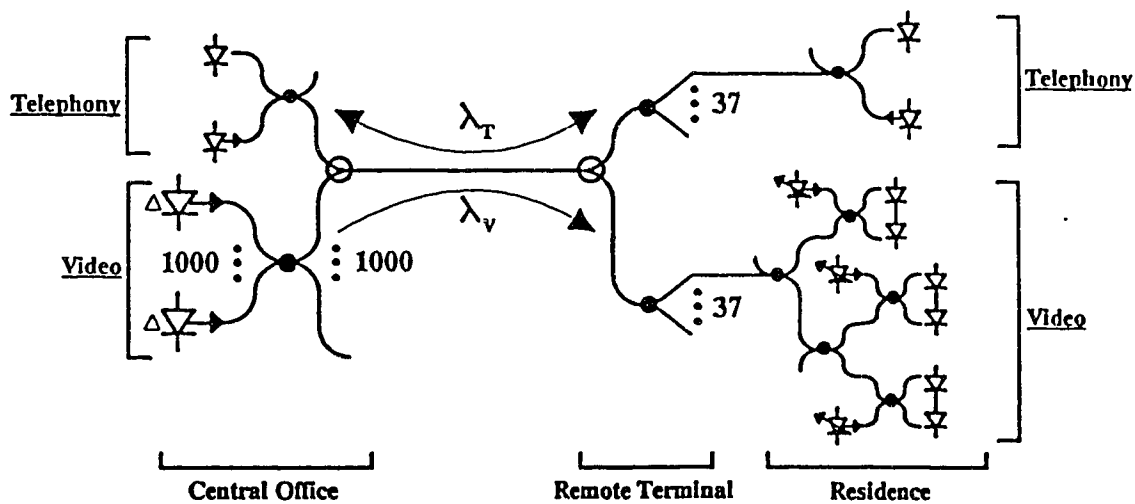
Figure 1.1 Fiber broadband access topology (System 103 from [6]).

Using coherent FDM, this system would provide both telephony and a large number of video channels without blocking. A tunable local oscillator laser at each receiver would then be used to demultiplex or "tune in" the desired video channel. Their analysis indicated that such a system would comprise a "high quality digital coherent network compatible with a digital HDTV format". However, due to the presently high

cost of optical components and tunable lasers required at the receiver, the system would not be as cost competitive as the centrally switched point-to-point systems. Cormack and Waschuk concluded that *if* and *only if* a low cost receiver were perfected, would this system provide "significant cost and service advantages relative to all other systems". Since a CM receiver is only slightly more complex than a direct detection receiver, requires low bandwidth electronics and does not require a local oscillator laser, it would appear to be an attractive multiplexing option for System 103. This thesis attempts to determine the fundamental performance limitations of the ERL CM architecture to determine if it should be considered as a potential multiplexing alternative to coherent FDM in a broadband access system of the form of System 103.

Chapter 2 provides an introduction to the fundamentals of CM and outlines three main architectures that can be used in a CM system.

The spectral characteristics of a single-mode laser diode are examined in Chapter 3 and a theoretical model is developed to predict the capacity of a hypothetical heterodyne ERL multi-channel CM system. We extend this analysis to determine the capacity of this system using a digital OOK modulation scheme.

Chapter 4 describes the experimental apparatus used to obtain measured results for the thesis. Experimental data are used to confirm portions of the theoretical model developed in Chapter 3. Chapter 4 concludes by simulating the multiplexing capacity of the hypothetical multi-channel CM system. We particularly look at the effects of differential path length mismatch and optical power optimization.

A summary of the entire thesis is provided in Chapter 5. Limitations on the capacity of the CM architecture examined are discussed and the application of such a technique to a FTTH system is assessed. Possible future directions for CM research are presented and other application areas that may benefit from CM are proposed.

2. PRINCIPLES OF COHERENCE MULTIPLEXING

2.1 Introduction

The technique of coherence multiplexing is similar in concept to the spread spectrum technique used in radio communications. In radio, an information signal is modulated with a random (or pseudo-random) reference signal and transmitted. The random signal is designed to produce a transmitted signal with a spectral width much wider than the original information signal. To recover the information signal, the receiver must correlate the received signal with an identical version of the random (or pseudo-random) reference signal. This causes the desired information signal to be "collapsed" to its original spectrum while leaving the unwanted signals spread over a much larger spectral width. The correlated signal is filtered by a matched filter resulting in a rejection of interference noise outside the filter passband. Hence it is possible to obtain a reasonable receiver SNR even with a number of interfering signals.

The same effect can be achieved if the information signal is used to modulate a random carrier signal. In coherence multiplexing, the information signal is used to modulate the light output of the laser diode externally. Phase noise in the laser creates random fluctuations in the frequency of the light output. Optical delay lines preceding the external modulators are used to decorrelate each channel with the optical reference signal. The modulated light from each transmitter is combined and transmitted down a common path called the bus path. To decode a particular channel, an optical delay which matches the transmitter delay of the desired channel is inserted in the reference fiber at the receiver. The delayed reference and bus signals are combined and mixed on a photodetector at the receiver. Only the desired channel will be "collapsed" to its original spectrum while leaving all others spread over a very large frequency range. Careful filtering of the photodetector output can therefore reject most interference noise and achieve a sufficient signal to noise ratio to recover the channel information.

2.2 Fiber Sensor Multiplexing

The idea of using optical coherence to separate the signals returning from a series of interferometric fiber sensors was first published by Al Chalabi *et al.* [7]. Since then, there has been much interest in using this technique as a method for multiplexing fiber sensor arrays.

Conventional sensor multiplexing methods include two main techniques. The first technique, time-division multiplexing, typically employs a pulsed optical source. The system geometry is arranged such that pulses from the optical sensors return to the receiver separated in time on a common fiber bus. The second approach, frequency-division multiplexing, typically uses a frequency ramped optical source. The system geometry is arranged such that the transit time of the light from the source to a sensor and back to the receiver is unique for each sensor. The delayed output from each sensor is mixed with the source's non-delayed signal producing a unique heterodyne frequency for each sensor.

The technique of coherence multiplexing was firmly established with a key paper published by Brooks *et al.* [1]. Their work built on the technique of Al-Chalabi and established a number of proposed fiber-based CM architectures. These architectures will be discussed in Section 2.4.

2.3 Interferometer Basics

Since coherence multiplexing has its basis in optical interferometry, it is appropriate to introduce the concepts of CM by examining the operation of the simple Mach-Zehnder[1] interferometer shown in Figure 2.1.

---

[1] A balanced Mach-Zehnder interferometer would have the observation screen in the upper right-hand corner so that the lengths of paths L2, and L1 would be equal. Here we show a slightly modified version of that configuration which is useful for illustration purposes.
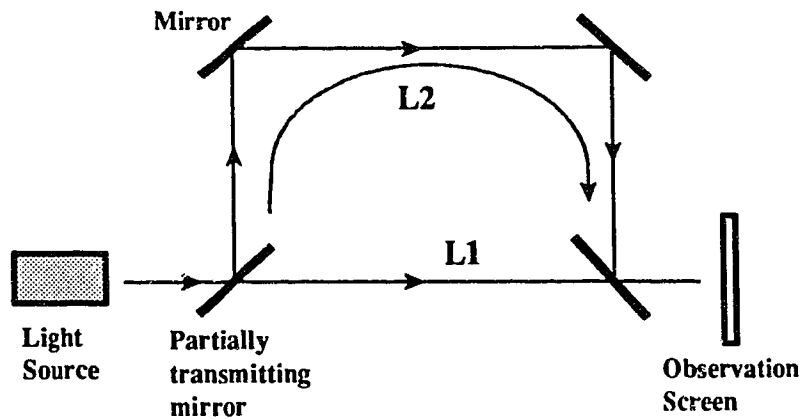
Figure 2.1 Modified Mach-Zehnder interferometer.

As the input to the system we have an arbitrary, visible light source which injects light into the interferometer. The first partially transmitting mirror splits the light along two paths, L2 and L1. After traversing distances L2 and L1, the two light components are then recombined and displayed on an observation screen. We denote the *optical path difference*(OPD), by ΔL where ΔL = L2 - L1. If we initially set ΔL = 0 and gradually start to increase ΔL, we will observe alternating periods of constructive and destructive interference. As we continue to increase ΔL, we will notice a reduction in the depth of this interference. Increasing ΔL further, we will eventually reach the point where no interference will be visible. It turns out that if ΔL is much greater than a quantity called the *coherence length*[2] of the source, L_c, interference fringes will not be observed. If, however, $\Delta L < L_c$, interference fringes will be observed [8]. The technique of CM capitalizes on this phenomenon and the operation of the CM system will become more clear in the following section.

---

[2] Coherence length is treated in detail in Section 3.1.1.

2.4 System Topologies

As stated previously, several fiber-based CM architectures were proposed in the original work by Brooks *et al.* [1]. The basic configurations are the "series", "extrinsic-reference ladder" and "intrinsic-reference ladder" systems. The "series" configuration is shown in Figure 2.2. Note that a two channel system is shown for simplicity.
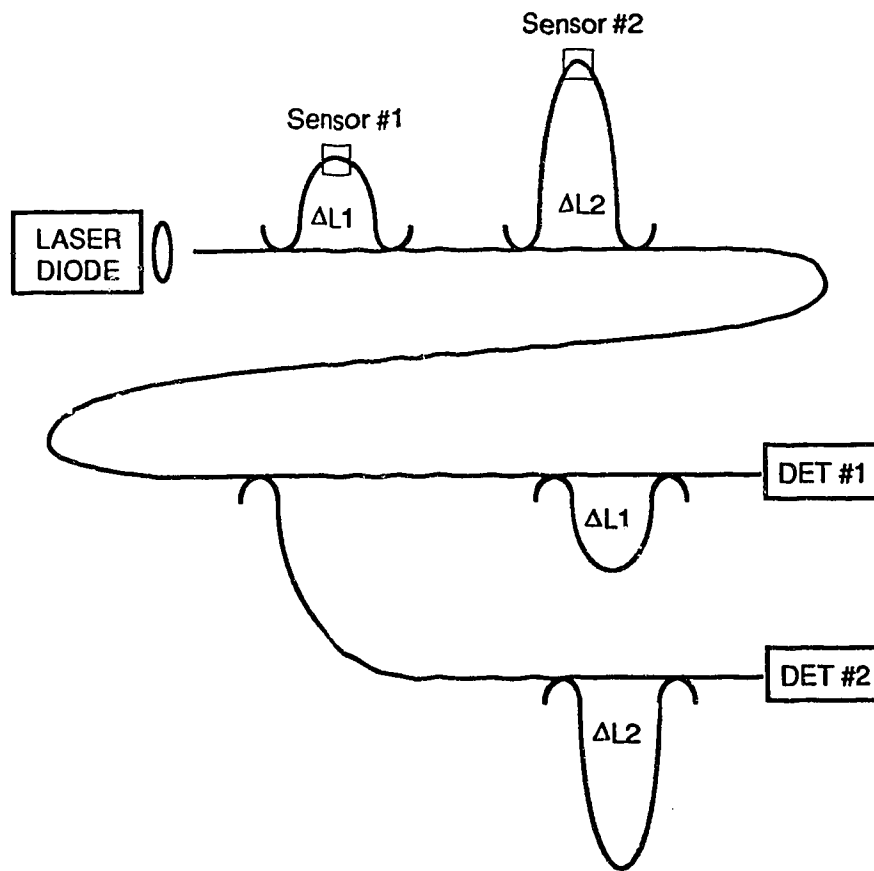
Figure 2.2 Schematic of a two channel "series" CM architecture.

We assume that the laser diode is characterized by a coherence length, L_c. Light is coupled into the fiber and is sent through two Mach Zehnder transmitter interferometers with OPD's, $\Delta L1$ and $\Delta L2$, respectively. The interferometers are constructed by using directional couplers and placing a fiber sensor in one of the interferometer paths. If the

OPD of a transmitter interferometer was hypothetically equal to zero and the fiber sensor modulated the phase of the light, the phase modulation would be converted to intensity modulation at the output of the interferometer. The OPD's of the interferometers, however, are selected to be much larger than the coherence length of the source such that phase modulation in one arm will not produce detectable intensity modulation at the interferometer output. However, after the light passes through the receiver interferometers, intensity modulation will be observed at the photodetectors. Intensity modulation at photodetector #1 (DET #1) will be due to the phase modulation of Sensor #1 only and the same situation applies for Sensor #2 and photodetector #2.

The series architecture has the advantage that only one fiber is required to connect the transmitter array to the receivers. Changes in this fiber length due to thermal fluctuations or mechanical stress will generally not effect the operation of the system.

The second architecture, the "extrinsic-reference ladder" (ERL) configuration, is a parallel configuration and is shown in Figure 2.3. The ERL system derives its name from the separate reference "arm" or fiber that is required in addition to the channel bus to recover signals at the receiver. The light from the laser is coupled into the fiber and split along two paths by a directional coupler. Part of the light feeds the transmitter sensors and the other part (through the reference arm) feeds the receiver photodetectors through a series of tapped delay lines. The difference between the path lengths of the sensing loops is arranged to be much larger than the coherence length of the source. The delay lines are arranged such that the fiber path length from the laser to a photodetector is equal to the distance traversed from the laser, through the associated sensor, to the photodetector. As in the "series" system, intensity modulation produced at photodetector #1 (DET #1) is due only to phase modulation produced by Sensor #1 and the same behavior applies for Sensor #2 and photodetector # 2.
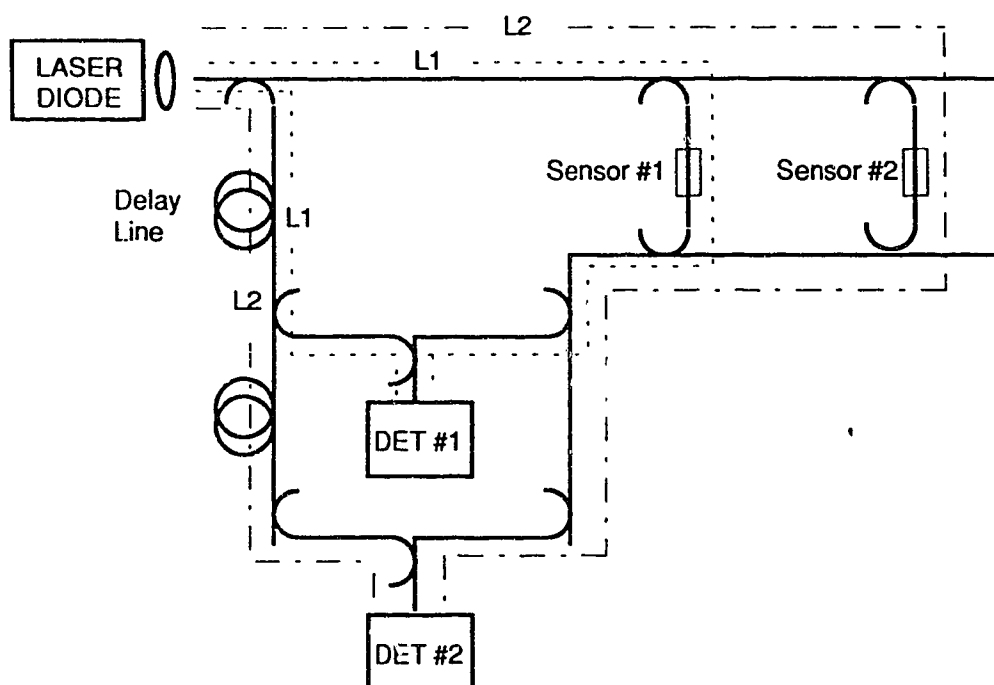
Figure 2.3 Schematic of a two channel "extrinsic-reference ladder" CM architecture.

The "intrinsic-reference ladder" (IRL) system, shown in Figure 2.4, is essentially a hybrid of the ERL and series architectures. The IRL system has the advantage of a single interconnection fiber (as in the series system) but allows greater flexibility in the selection of OPD values in the system. However, the analysis of Wentworth [5] has shown that the performance of the IRL topology is generally poorer than that of either the series or ERL system. It is suspected that this is due in part to higher splitting losses in the IRL topology.

The greatest advantage of the series and IRL configurations is that only a single fiber is required to connect the transmitter array with the receiver array. The disadvantage of the ERL configuration is that it requires two fibers to make this connection and is therefore sensitive to differential changes in fiber length due to environmental effects. Several researchers have suspected that this may impose a physical limit on the capacity of an ERL system but no results have yet appeared in the

literature. Analysis contained in this thesis will address this problem and characterize the effect of fiber length mismatches on the system capacity. One possible way to reduce the
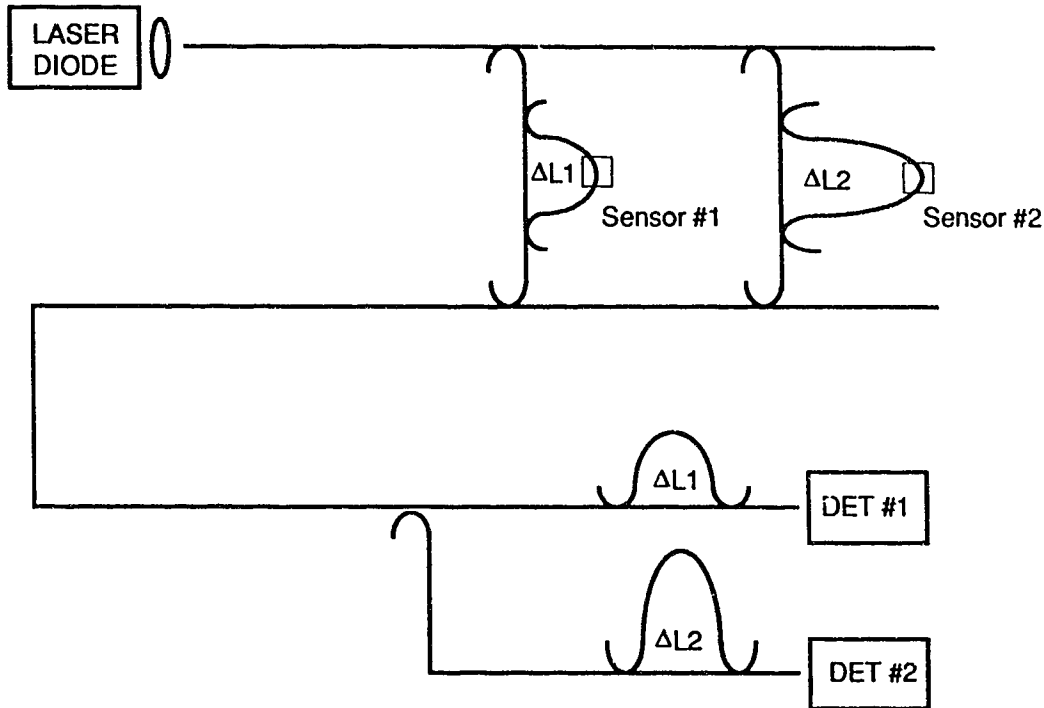
Figure 2.4 Schematic of a two channel "intrinsic-reference ladder" CM architecture.

sensitivity of differential length changes to environmental fluctuations (such as thermal variations or cable stress) would be to use two physically adjacent fibers in a telecommunications cable[3] as the interconnection fibers.

The series system does suffer from one major limitation, however, in that selection of OPD's in a series system becomes increasingly difficult as the number of channels, N, increases. When selecting OPD's for the transmitters in the ERL system, it is only necessary to ensure that each successive path length (from the transmitter, through the sensor to the receiver) differs from the previous one by at least an amount, L_d, where $L_d \gg L_c$. For example, in Figure 2.3, L1 would be equal to L_d and L2 would be equal to

---

[3] Telecommunications cables typically consist of many fibers bundled together and enclosed in a common outer casing.

$2L_d$. In general, for an N channel system we would have $L_n = nL_d$. Hence, the total delay line length required, increases linearly with the number of channels in the system.

In a series system, however, there are multiple path combinations through the transmitter interferometers that may produce identical path lengths. Brooks *et al.* have shown that to avoid this situation, only certain sequences of OPD's are permissible. The permissible delay sequence which is presently known is based on a recursive relation [1]. Using this relation, the length of the maximum OPD in the series system grows exponentially with the number of channels in the system, imposing a significant limit to the implementation of the series system.

An additional advantage of the ERL system is that, in a perfectly matched system, the ERL architecture appears to exhibit superior noise performance over the other architectures regardless of the number of channels in the system [5]. This can be intuitively understood by noting that in the series and IRL systems, multiple path combinations increase the number of light components which may interfere with each other, effectively increasing the noise level at the receiver.

One of the requirements of a FTTH telecommunications system is to provide the end user with the ability to select from a large number of signal channels. Since the ERL system employs realistic delay sequences and offers the greatest multiplexing capacity, it was chosen a basis for the system analyzed in this thesis.

2.4.1 Homodyne/Heterodyne Receiver Structures

All of the sensor system architectures previously discussed are homodyne systems. In homodyne systems, a baseband signal is produced by the mixing of two light fields with the same average frequency. A phenomenon called *signal fading* can be a significant problem in a homodyne system. If relative phases between light components are allowed to wander (due to low frequency environmental effects), the interference may change from constructive to destructive, resulting in a complete loss of signal. This

problem can be avoided by using a heterodyne scheme instead. Heterodyne operation can be obtained by shifting the frequency of one of the light fields by a constant value. The mixing of light fields at the receiver will then produce a signal spectrum which is centered on a difference frequency equal to the frequency shift. Standard radio techniques can then be used to phase-lock a local oscillator to this carrier and synchronously demodulate the signal.

Smith *et al.* have proposed a heterodyne variant of the original ERL system of Brooks for telecommunication applications [2]. In their original work, they used acousto-optic A/O modulators in the transmitter section to modulate the intensity of the light and simultaneously perform the frequency shifting function. The system architecture examined in this thesis is based on their system and will be discussed in detail in Section 3.3.

3. THEORETICAL ANALYSIS OF A CM SYSTEM

3.1 Output Spectrum of a Laser

To characterize the performance of a CM system, it is necessary to understand the spectral properties of the head end light source. Several options are available as sources for a fiber-based CM system. These include:

i) Semiconductor laser - laser diodes are generally used because of the high degree of temporal coherence[1] in their output.

ii) Superluminescent diode (SLD) - SLD' s generally possess more temporal coherence than that of an LED but less than that of a laser diode.

iii) Light emitting diode (LED) - LED's produce highly incoherent light with a resulting spectral width which is relatively large.

Goedgebuer et al. [11] have measured and characterized the spectral properties of certain multi-mode lasers and SLD's. They found that highly multi-moded lasers exhibit a Lorentzian spectral envelope while lasers producing only a few modes have a $\cos^2$ power spectrum. SLD's exhibited a Gaussian spectral profile.

In the theoretical analysis and experimental measurements reported in this thesis, an InGaAsP DFB laser diode was employed as the source. The spectral properties of an InGaAsP distributed feedback (DFB) laser are generally well understood [9, 10] and the output spectrum is characterized by oscillation in a single longitudinal mode with a Lorentzian line shape. The theoretical justification for the Lorentzian lineshape is given in [12] and is summarized over the next several pages.

---

[1] Temporal coherence is treated in section 3.1.1.

If a laser were a perfectly monochromatic source, the optical radiation field could be represented by

$$e(t) = E_o \cos(\omega_o t + \phi) \tag{3.1.1}$$

where E_o is a constant electric field amplitude, ω_o is the oscillation frequency and ϕ is a constant phase shift. However, in a practical laser diode the field undergoes random changes in amplitude and phase which can be represented by

$$e(t) = E(t) \cos\{\omega_o t + \phi(t)\} \tag{3.1.2}$$

or equivalently,

$$e(t) = \text{Re} \left[E(t) \, e^{j(\omega_o t + \phi(t))} \right] \tag{3.1.3}$$

where $E(t)$ and $\phi(t)$ vary only slightly during one optical period and are real functions.

In the lasing cavity, any photons which are generated by stimulated emission will add energy which is phase and frequency synchronous with the existing field. In laser diodes, $E(t)$ and $\phi(t)$ are largely due to quantum noise which results from spontaneous emission. Photons generated by spontaneous emission add energy which has a random phase component. As a result, fluctuations in the phase and intensity of the lasing field occur. Figure 3.1 shows how spontaneous emission alters the phase and amplitude of the optical field.
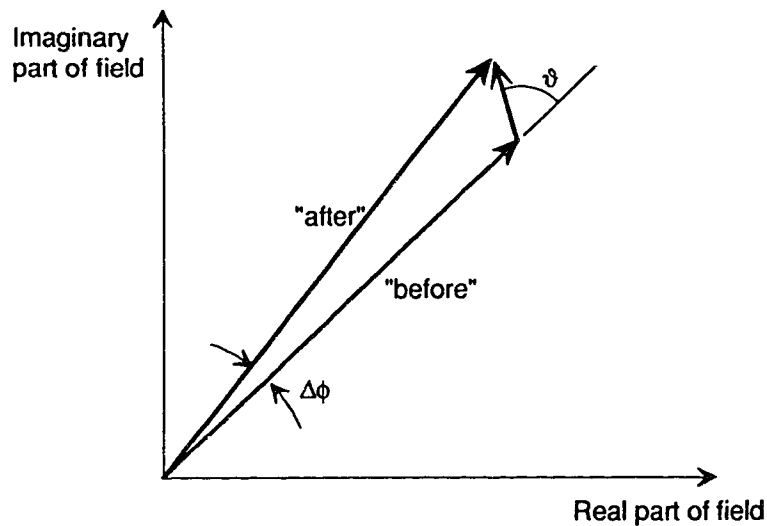
Figure 3.1 Phasor diagram showing instantaneous change in the phase and intensity of the optical field caused by a spontaneous emission event.

The field can be represented by a phasor rotating at a radian frequency, ω_0. If we have one spontaneous emission event which adds one photon to the existing field incoherently, the angle and amplitude of the new field are changed by $\Delta\phi$ and $\cos\vartheta$ respectively. The phase angle, ϑ, that the additional photon may assume, is any value between 0 and 2π with equal probability and $\phi(t)$ can therefore be described as a 2-dimensional random walk process[2]. In the real laser, the change in field phase, $\Delta\phi$, is the net result of many small, statistically independent spontaneous emissions. Consequently, the central limit theorem applies and $\phi(t)$ can be treated as a Wiener random process[3] which possesses the following three properties:

1. The initial position is zero:

$$\phi(0) = 0.$$

2. The mean is zero:

$$E\{\phi(t)\} = 0, \quad t > 0.$$

---

[2] See reference [13], pp. 74 - 75.
[3] See reference [13], pp. 108 - 112.

3. The increments of $\phi(t)$, $\phi(t_2) - \phi(t_1)$, are independent, stationary and Gaussian.

The field amplitude, E(t), varies slightly due to gain saturation and this variation has negligible effect on the laser spectrum. Therefore, E(t) is assumed to be constant in the following treatment (the effects of variation in field amplitude will be treated later in section 3.4). We therefore have

$$e(t) = E_o \cos \{\omega_o + \phi(t)\}. \tag{3.1.4}$$

It can be shown that the autocorrelation function for this expression is of the form

$$R(\tau) = < e(t)\, e(t + \tau) > = \exp(-\pi\delta f\, |\tau|)\, \cos(2\pi f_o \tau) \tag{3.1.5}$$

where a multiplicative constant has been omitted [14]. Applying the Wiener-Khintchine theorem, the power density spectrum of the field is found by taking the Fourier transform of the autocorrelation function. Hence,

$$S(f) = \int_{-\infty}^{\infty} R(\tau)\, e^{-j2\pi f\tau}\, d\tau \;=\; \frac{\delta f}{2\pi[\,(f - f_o)^2 + (\delta f/2)^2\,]} \tag{3.1.6}$$

corresponds to a *Lorentzian* power spectrum. The Lorentzian spectral envelope is characterized by its peak amplitude and its Full Width at Half Maximum (FWHM), δf. When dealing with single-mode lasers, δf is usually referred to as the spectral width or *linewidth*.

Experimentally measured linewidths are actually several orders of magnitude greater than that predicted by the preceding theory. Henry [15] determined that fluctuations of the index of refraction of the laser medium are responsible for this additional broadening. Spontaneous emissions momentarily alter the electron density in

the lasing medium and, as a result, the real and imaginary components of the index of refraction are altered. This has the effect of increasing the linewidth by the linewidth enhancement factor [15], α, where

$$\alpha = 1 + \left(\frac{\Delta n_r}{\Delta n_i}\right)^2 \tag{3.1.7}$$

where Δn_r and Δn_i are the changes in the real and imaginary parts of the index of refraction.

In certain single-mode lasers, the lineshape is not exactly Lorentzian and exhibits satellite peaks which are separated from the main peak by the laser relaxation resonance frequency and multiples thereof. Daino *et al.* [16] have analyzed this behavior and have determined that these satellite peaks are due to relaxation oscillations which are triggered by spontaneous emission events. This behavior is not observed if the relaxation oscillations are well damped.

3.1.1 Coherence Time

It is useful to characterize an optical source by its *temporal coherence*. Temporal coherence refers to the ability of a light beam to interfere with a time-delayed version of itself. If the beam is highly coherent, interference will be observed over relatively long delay times. If the beam is highly incoherent, interference will only be observed during very short delay times. Following the definition used by Goodman [17], *coherence time* is given as

$$\tau_c = \int_{-\infty}^{\infty} |\gamma(\tau)|^2 \, d\tau \tag{3.1.8}$$

where $\gamma(\tau)$ is the *complex degree of coherence*. The real part of the complex degree of coherence is the temporal autocorrelation function of the light field. For a Gaussian spectral shape, the complex degree of coherence would be [17]

$$\gamma(\tau) = \exp\left[-\left(\frac{\pi\delta f\tau}{2\sqrt{\ln 2}}\right)^2\right]\exp(-j2\pi f_o\tau) \tag{3.1.9}$$

yielding a coherence time of

$$\tau_c = \sqrt{\frac{2\ln 2}{\pi}}\frac{1}{\delta f} \tag{3.1.10}$$

where δf is the spectral linewidth and f_o is the average oscillation frequency. For a Lorentzian spectral shape, the complex degree of coherence is [17]

$$\gamma(\tau) = \exp[-\pi\delta f|\tau|]\exp[-j2\pi f_o\tau] \tag{3.1.11}$$

which yields the coherence time

$$\tau_c = \frac{1}{\pi\delta f}. \tag{3.1.12}$$

Both (3.1.10) and (3.1.12) show that the product of the spectral linewidth and the coherence time of the light source is constant. It is also useful to define the coherence *length*, L_c, of the source as

$$L_c = \frac{c}{n}\tau_c \tag{3.1.13}$$

where c = the speed of light in vacuum and n = the refractive index of the optical medium.

The concept of coherence time (or length) is useful in the analysis of interferometric systems. For example, if we examine the output of a Michelson interferometer we observe a change in the depth of fringe visibility as we vary the mismatch length in the interferometer arms. If the mismatch length is set to some value less than the coherence length of the source, fringe visibility is very good. If the mismatch length is set to a value much greater than the coherence length of the source, no fringes will be visible.

3.2 Interferometric Noise

The SNR performance of a CM system is primarily limited by phase-induced intensity noise. Knowledge of the noise power spectrum is therefore necessary to determine the SNR of such a system. Kikuchi and Okoshi [14] provide a model for determining the power spectrum of this interference noise when the optical source has a Lorentzian lineshape. Due to the fundamental importance of their work to this thesis, their treatment will now be summarized.

Figure 3.2 shows the setup that Kikuchi and Okoshi developed to measure the spectral linewidth of a single longitudinal mode laser. The laser light is divided into the two paths, labelled Branch 1 and Branch 2. The light in branch 1 passes through an acousto-optic (A/O) modulator which shifts its frequency up by ω_s. The light in branch 2 passes through a length of single-mode fiber creating a time delay, τ_d. The outputs of branches 1 and 2 are then combined and mixed on a photodetector. The photocurrent of the photodetector is amplified and fed to an RF spectrum analyzer. If the delay, τ_d, is selected to be much larger that the coherence time of the source, τ_c, the two output signals are uncorrelated and a beatspectrum will be observed on the spectrum analyzer.
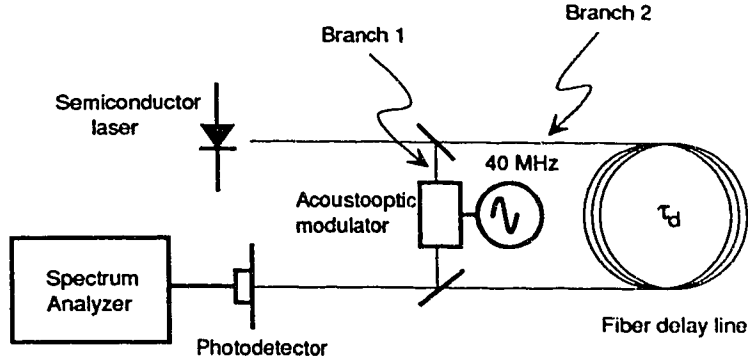
Figure 3.2 Delayed self-heterodyne setup.

If the following assumptions are made, the photodetector output spectrum can be obtained using Kikuchi and Okoshi's method [14]. The remainder of this section, 3.2, is taken from their paper.

i) The spectral spread of the laser is primarily due to *phase fluctuations* in the optical field and

ii) The spectral shape is Lorentzian.

As stated previously in Section 3.1, these assumptions generally apply for an InGaAsP DFB laser. Under these assumptions, then, the electric field intensity of the laser light can be expressed as

$$e(t) = E(t)e^{j2\pi f_o t} + E^*(t)e^{-j2\pi f_o t} \qquad (3.2.1)$$

where f_o is the average oscillation frequency and * denotes the complex conjugate. $E(t)$ is assumed to vary much more slowly than $e^{j2\pi f_o t}$. Spontaneous emission randomly disturbs the laser oscillator and can be represented as $\gamma(t)e^{j2\pi f_o t}$ where $\gamma(t)$ represents the random disturbance. $E(t)$ contains both amplitude and phase fluctuations but if the laser is operated well above threshold, the phase fluctuation dominates and $E(t)$ can be expressed as

$$E(t) = A_o e^{j\phi_n(t)} \tag{3.2.2}$$

where A_o denotes a constant amplitude and $\phi_n(t)$ represents a random phase fluctuation. $\phi_n(t)$ is a Wiener random process as described in section 3.1. Hence,

$$< \phi_n(t) > = 0$$

where $<...>$ denotes time averaging and

$$A_o \frac{d\phi_n}{dt} = \gamma_i \tag{3.2.3}$$

where γ_i is the imaginary component of γ and is Gaussian. The electric field at the output of branch 1 is

$$e_1(t) = A_1 \cos\{2\pi(f_o + f_s)t + \phi_n(t)\} \tag{3.2.4}$$

where f_s is acousto-optic modulator shift frequency. Branch 2 delays the optical signal by the fiber delay line transit time, τ_d. The field at the output of branch 2 is

$$e_2(t) = A_2 \cos\{2\pi f_o(t - \tau_d) + \phi_n(t - \tau_d)\}. \tag{3.2.5}$$

The output signals of branches 1 and 2 are combined in a coupler which is coupled to the photodetector. Neglecting a constant factor and components at the sum frequency, the output photocurrent is given by

$$i(t) = A_1^2 + A_2^2 + 2A_1 A_2 \cos\{2\pi f_s t + 2\pi f_o \tau_d + \phi_n(t) - \phi_n(t - \tau_d)\} \tag{3.2.6}$$

The autocorrelation function of the complex amplitude of the photocurrent (which Kikuchi and Okoshi refer to as the *IF signal*) can be obtained as

$$R(t) = \begin{cases} \exp(-2\pi\delta f|\tau|) & |\tau| <= \tau_d \\ \exp(-2\pi\delta f\tau_d) & |\tau| > \tau_d \end{cases}$$

(3.2.7)

where δf is the linewidth (FWHM) of the laser spectrum. The power spectrum of the envelope of the IF signal is obtained by taking the Fourier transform of the autocorrelation function:

$$S(f) = \int_{-\infty}^{\infty} R(t)\, e^{-j2\pi f\tau}\, d\tau$$

$$= e^{-2\pi\delta f\tau_d}\,\delta(f) + \frac{\delta f}{\pi\{f^2 + \delta f^2\}}\,[1 - e^{-2\pi\delta f\tau_d}\,(\cos 2\pi\tau_d f + \frac{\delta f}{f}\sin 2\pi\tau_d f)]$$

(3.2.8)

Note that an error in the original equation has been corrected [18] in (3.2.8). Including the frequency shift of the A/O modulator, the two sided power spectrum is obtained as

$$S(f) = \frac{1}{2}\left\{ e^{-2\pi\delta f\tau_d}\,\delta(f-f_s) + \frac{\delta f}{\pi\{(f-f_s)^2 + \delta f^2\}}\left[1 - e^{-2\pi\delta f\tau_d}\{\cos 2\pi\tau_d(f-f_s) + \frac{\delta f}{f}\sin 2\pi\tau_d(f-f_s)\}\right]\right\}$$
$$+ \frac{1}{2}\left\{ e^{-2\pi\delta f\tau_d}\,\delta(f+f_s) + \frac{\delta f}{\pi\{(f+f_s)^2 + \delta f^2\}}\left[1 - e^{-2\pi\delta f\tau_d}\{\cos 2\pi\tau_d(f+f_s) + \frac{\delta f}{f}\sin 2\pi\tau_d(f+f_s)\}\right]\right\}$$ (3.2.9)

Leading constants are not included in Kikuchi and Okoshi's published result nor do they appear in (3.2.8). If these constants are included, the beatspectrum is given by

$$S_{abs}(f) = 2R_o^2\, P_1 P_2\, S(f)$$

(3.2.10)

where P_1 and P_2 are the time averaged optical powers incident on the photodetector from branches 1 and 2 respectively and R_o is the responsivity of the photodetector.

Several important observations can be deduced from (3.2.8):

1) For values of $\tau_d \delta f \gg 1$, $S(f)$ reduces to

$$S(f) = \frac{\delta f}{\pi\{(f-f_s)^2 + \delta f^2\}}$$

(3.2.11)

which consists of a Lorentzian power spectrum centered on f_s with a FWHM which is *twice* that of the laser linewidth (see Figure 3.3 (a)). This relation is the basis behind the delayed self-heterodyne technique (DSH) [14] for measuring laser linewidths.

2) For values of $\tau_d \delta f \sim 1$, $S(f)$ consists of a broad "noise" pedestal with a delta function at f_s (Figure 3.3 (b)).

3) For values of $\tau_d \delta f \ll 1$, $S(f)$ is dominated by a delta function at f_s (Figure 3.3 (c)).
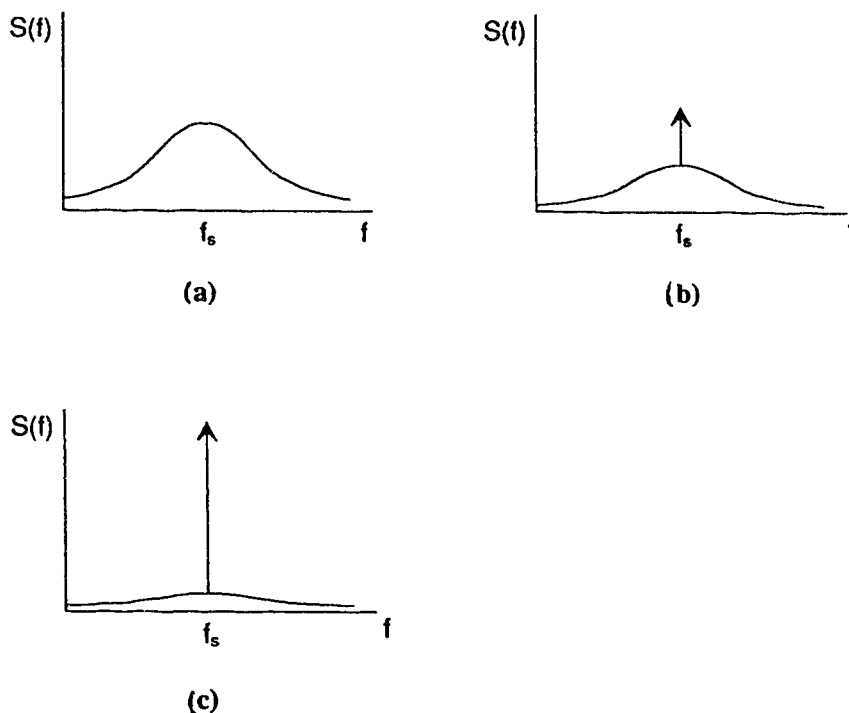
Figure 3.3 Power spectrum of detector signal for delay regimes, (a) $\tau_d \delta f \gg 1$, (b) $\tau_d \delta f \sim 1$, and (c) $\tau_d \delta f \ll 1$.

By varying the value of the product, $\tau_d \delta f$, it is apparent that the distribution of power in the beatspectrum can be varied between a single frequency "carrier" tone (Figure 3.3 (c)) and a broad-band noise spectrum (Figure 3.3 (a)). This variation is the key principle behind coherence multiplexing and the results obtained here will be used in Section 3.3 to develop an expression for the signal to interference noise ratio.

3.3 System Configuration

For the reasons cited in Section 2.4.1, a heterodyne ERL topology was chosen as most appropriate for a fiber-based CM communications system. The multichannel ERL CM system analyzed in this thesis is based on the ERL heterodyne system of Smith *et al.* [2] with the exception that the laser source is not frequency chirped. The multichannel ERL CM transmitter multiplexer is shown in Figure 3.4.

A continuous wave (CW) laser drives the system at the head end. The light from the laser is split into two paths, the reference arm[4] and the channel arm. The reference arm is connected to the receiver. The channel arm is split further and coupled into N acousto-optic (A/O) modulators[5]. The A/O modulators imprint channel information onto the light by on/off intensity modulation, also called on-off keying or OOK. In addition, they impart a fixed frequency shift to the modulated light. The light from each modulator travels through a delay line whose length is unique to that particular channel. The delay of each additional channel is longer than that of the preceding channel by τ_d. For example, the delay of channel 1 is zero seconds, the delay of channel 2 is τ_d seconds, the delay of channel 3 is $2\tau_d$ seconds, etc.
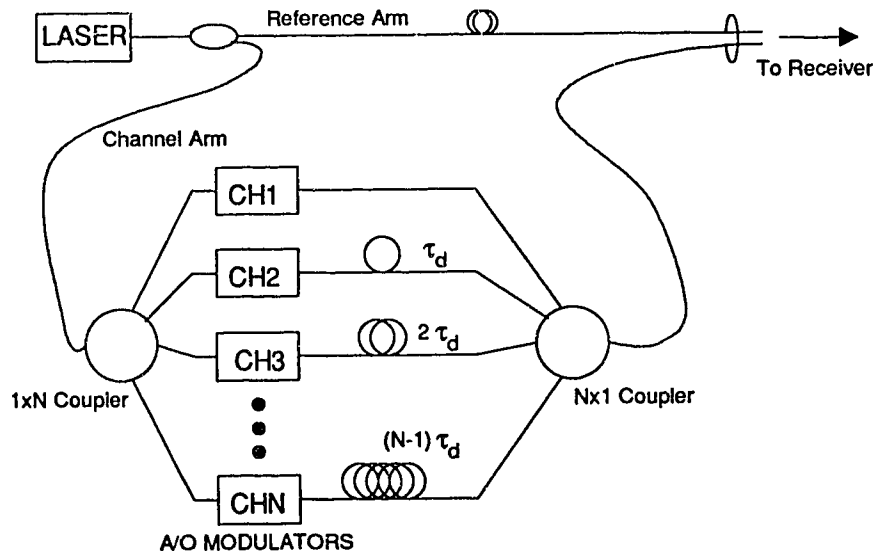
Figure 3.4 Multichannel ERL heterodyne CM transmitter array

The outputs of the channel delay lines are combined with an Nx1 coupler[6]. The output of this coupler, the channel "bus", is routed to the receiver. At the receiver, (Figure 3.5), the reference arm light is passed through a variable delay and combined with the light from the channel bus. The output of the coupler is coupled to a PIN photodiode as shown in Figure 3.5 or for higher gain, to a balanced detector. The receiver processing electronics consist of amplification stages, an RF local oscillator, phase-locked loop (PLL), mixer, and a noise filter characterized by a noise equivalent bandwidth, B. In the case of a digital system, additional stages would provide clock recovery and decision slicing.
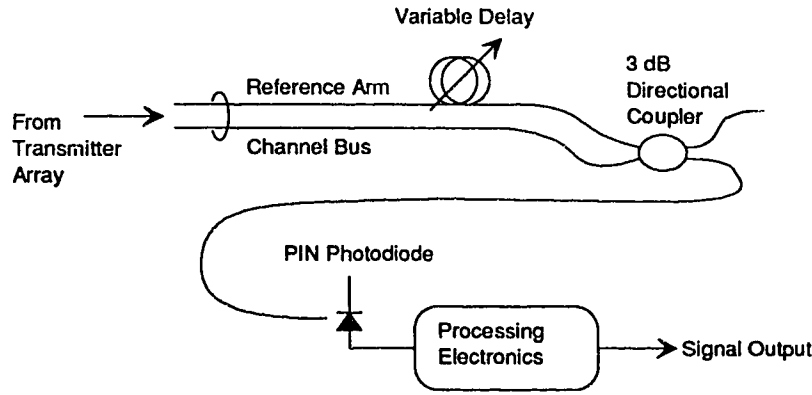
Figure 3.5 ERL heterodyne CM receiver

As stated previously, the semiconductor laser in the transmitter is assumed to oscillate in a single longitudinal mode with a Lorentzian lineshape. The output electric field is given by:

$$e(t) = E(t)\cos(\omega_0 t + \phi(t))$$ (3.3.1)

6 In a multi-receiver system, an NxN coupler could actually be used. This would allow an additional (N-1) receivers to be serviced in addition to the one shown in Figure 3.5.

where E(t) is the slowly varying function responsible for light intensity fluctuations and $\phi(t)$ is the time-varying random phase of the light modeled as a Wiener random process. ω_0 is the average oscillation frequency of the laser light. Again we assume that E(t) is relatively constant[7] and has negligible contribution to the laser spectrum. Neglecting coupler losses, the expression for the electric field in the reference arm is

$$e_r(t) = E_r \cos(\omega_0 t + \phi(t)). \tag{3.3.2}$$

Each transmitter channel contains an A/O modulator which intensity modulates the light. In addition, the A/O modulator shifts the frequency of the light up by a fixed acoustic frequency, ω_s. In the following analysis, we assume that the input signal to the modulators consists of only a DC component which turns the modulators fully on. This assumption will not affect the generality of these initial theoretical results because any arbitrary modulation spectrum can be accounted for by convolving it with the spectral components for the DC case. This DC analysis will lead to an expression for the carrier to noise ratio (CNR) instead of the SNR. SNR can then be determined *a priori* by applying an appropriate scaling factor based on the modulation scheme employed.

If we first consider a two channel system and set the delay at the receiver equal to zero, the expression for the signal transmitted from channel #1 is

$$e_1(t) = E_1 \cos\{(\omega_0 + \omega_s)(t-\tau_d) + \phi(t-\tau_d)\}$$

$$= E_1 \cos\{(\omega_0 + \omega_s)t + \phi(t-\tau_d) - (\omega_0 + \omega_s)\tau_d\} \tag{3.3.3}$$

---

[7] For laser diodes operated well above threshold, intensity noise is low and has negligible contribution to the linewidth. [19]

and the expression for the signal transmitted from channel #2 is

$$e_2(t) = E_2 \cos\{(\omega_o + \omega_s)(t-2\tau_d) + \phi(t-2\tau_d)\}$$

$$= E_2 \cos\{(\omega_o + \omega_s)t + \phi(t-2\tau_d) - 2(\omega_o + \omega_s)\tau_d\} \qquad (3.3.4)$$

where we will assume that $\tau_d \gg \tau_c$, the coherence time of the source. After travelling equal distances, the reference light is combined with the light from the channel bus and mixed on the photodetector. Neglecting coupler losses, the output of the photodetector $i_{ph}(t)$ is given by

$$i_{ph}(t) = R <(e_r(t) + e_1(t) + e_2(t))^2>$$

$$= R <e_r(t)^2 + e_1(t)^2 + e_2(t)^2 + 2e_r(t)e_1(t) + 2e_r(t)e_2(t) + 2e_1(t)e_2(t)>$$

$$= R\,[E_r^2/2 + E_1^2/2 + E_2^2/2$$

$$+ E_r E_1 \cos\{\omega_s t + \phi(t-\tau_d) - \phi(t) - \omega_o\tau_d)$$

$$+ E_r E_2 \cos\{\omega_s t + \phi(t-2\tau_d) - \phi(t) - 2\omega_o\tau_d\}$$

$$+ E_1 E_2 \cos\{\phi(t-2\tau_d) - \phi(t-\tau_d) - \omega_o\tau_d\}] \qquad (3.3.5)$$

where R is equal to the responsivity of the PIN detector divided by the intrinsic impedance of the photosensitive medium. Note that $<...>$ denotes time averaging. If we make $\tau_d \gg \tau_c$ and assume that the laser has a Lorentzian lineshape, we can apply (3.2.9) and the last three terms yield a power spectrum which is Lorentzian in shape with a FWHM twice that of the laser linewidth.

If we wish to receive the signal from channel #1, an optical delay of duration τ_d is inserted in the reference arm at the receiver. The field in the reference arm becomes

$$e_r(t) = E_r \cos\{\omega_o(t-\tau_d) + \phi(t-\tau_d)\} \qquad (3.3.6)$$

and the output of the photodetector becomes

$$i_{ph}(t) = R \, [E_r^2/2 + E_1^2/2 + E_2^2/2$$

$$+ E_r E_1 \cos(\omega_s t)$$

$$+ E_r E_2 \cos\{\omega_s t + \phi(t-2\tau_d) - \phi(t-\tau_d) - \omega_o \tau_d\}$$

$$+ E_1 E_2 \cos\{\phi(t-2\tau_d) - \phi(t-\tau_d) - \omega_o \tau_d\}]. \qquad (3.3.7)$$

The fourth term in (3.3.7) now yields the heterodyne carrier for the baseband information spectrum of channel #1 while the last two terms yield a Lorentzian power density spectrum and are responsible for interference noise from unwanted channels. The first three terms appear at DC and will contribute only to shot noise. If channels 1 and 2 were modulated with a signal, the second and third terms would also yield the baseband components which would be used in a direct detection system. If we generalize this situation to N transmitters and N receivers, we have the following summation of cross-products:

$$(e_R + e_1 + e_2 + ... + e_N)^2 = e_R^2 + 2\sum_{i=1}^{N} e_R e_i + \sum_{\substack{j=1}}^{N} \sum_{k=1}^{N} e_j e_k \qquad (3.3.8)$$

The cross products can be tabulated in matrix form as shown in Figure 3.6. To simplify this representation, only the element indices are shown in this table.

31

	R	1	2	...	N
R	R^2	R1	R2	...	RN
1	1R	1^2	12	...	1N
2	2R	21	2^2	...	2N
...	...	...	...	...	...
N	NR	N1	N2	...	N^2

Figure 3.6 Matrix representation of cross-product terms

Crossproducts along the main diagonal (R^2, 1^2, etc.) are self-beat products and produce terms of the form

$$\frac{E_R^2}{2} + \frac{E_R^2}{2}\cos\{2\omega_o t + 2\phi(t)\} \qquad \text{and}$$

$$\frac{E_i^2}{2} + \frac{E_i^2}{2}\cos\{2\omega_o t + 2\phi(t)\} \qquad i = 1,2,3,...,N. \qquad (3.3.9)$$

The zero frequency components will contribute to shot noise and the $2\omega_o$ frequency components appear at two times the light frequency and are time averaged to zero by the photodetector. Note that in the case of intensity modulation, the first term in (3.3.9) would also include the baseband signal components. In total there is one reference self-product and N channel self-products.

If we assume that one of the channel path lengths (channel 1 for example) is perfectly matched to that of the reference arm, two of the reference-channel cross

products (R1 and 1R) will yield the desired signal information. The two terms, R1 and 1R will add coherently and the resulting signal carrier term will be of the form:

$$[E_R E_1 \cos(\omega_s t) + E_R E_1 \cos\{\omega_s t + 2\omega_o t + 2\phi(t)\}]. \qquad (3.3.10)$$

The first term of (3.3.10) comprises the heterodyne carrier which carries the signal information. The second term appears at light frequencies and is time averaged to zero by the photodetector. In actual fact, we will not be able to match the path lengths exactly and some finite differential error will occur. We call this error the *mismatch length*, L_m. Allowing for the mismatch length, (3.3.11) becomes

$$[E_R E_1 \cos\{\omega_s t + \phi(t - \tau_m) - \phi(t)\} + E_R E_1 \cos\{\omega_s t + 2\omega_o t + \phi(t - \tau_m) + \phi(t)\}] (3.3.11)$$

where $\tau_m = nL_m/c$, n is the refractive index of the fiber and c is the speed of light in vacuum. In the derivation that follows, we will use this more general expression, (3.3.11), which will allow for mismatch errors in the system.

The channel-channel cross products (12, 13, etc.) generate coherent pairs (for example, 12 and 21) which, when added together, form the terms

$$2\,E_i \cos\{(\omega_o + \omega_s)t + \phi(t)\}\, E_j \cos [\,(\omega_o + \omega_s)\{t - (j-i)\tau_d\} + \phi\{t - (j-i)\tau_d\}]$$

$$= E_i E_j \cos [\phi\{t-(j-i)\tau_d\} - \phi(t) - (\omega_o + \omega_s)(j-i)\tau_d] +$$

$$+ E_i E_j \cos [2(\omega_o + \omega_s)t - (\omega_o + \omega_s)(j-i)\tau_d + \phi(t - (j-i)\tau_d) + \phi(t)]$$

$$i = 1,2,...,N, \quad j = 1,2,...,N, \quad j > i \qquad (3.3.12)$$

The first term generates a Lorentzian shaped power spectral density (PSD) centered at zero frequency. The second term generates components at light frequencies. There are $(N^2 - N)/2$ of these components.

The non-correlated reference-channel cross products (R2, R3, 2R, etc) generate coherent pairs of components (for example R2 and 2R) which, when added together, form the following terms:

$$E_R E_i \cos[\omega_s t + \phi\{t-(i-1)\tau_d\} - \phi(t)]$$

$$+ E_R E_i \cos[2\omega_o t + \omega_s t + \phi\{t-(i-1)\tau_d\} + \phi(t)] \qquad i = 2,3,...,N \qquad (3.3.13)$$

There are $(N-1)$ of these components. Note that for $i = 1$ (corresponding to the desired channel), (3.3.13) reduces to (3.3.1(?). A tally of the number of cross-product components is summarized in Table 3.1.

Table 3.1 Summary of Cross-Product Components

Component	Quantity	Multiplier	Spectral Content
Signal carrier (R1+1R)	1	$E_R E_1$	Delta fn. centered on $\omega = \omega_s$
Reference self-product	1	$0.5 E_R^2$	Delta fn. centered on $\omega = 0$
Channel self-products	N	$0.5 E_i^2$	Delta fn. centered on $\omega = 0$
Chan.-Chan. Products	$(N^2 - N)/2$	E_i^2	Lorentzian centered on $\omega = 0$
Ref.-Chan. Products	$(N-1)$	$E_R E_i$	Lorentzian centered on $\omega = \omega_s$

We now derive the signal carrier and noise powers produced by each of the cross-products.

We recall that the photodetector output PSD for the Kikuchi and Okoshi experiment was obtained as

$$\Phi(f) = \frac{1}{2} \left\{ e^{-2\pi\delta f \tau_d} \delta(f-f_s) + \frac{\delta f}{\pi \{(f-f_s)^2 + \delta f^2\}} \left[1 - e^{-2\pi\delta f \tau_d} \{\cos2\pi\tau_d (f-f_s) + \frac{\delta f}{f} \sin2\pi\tau_d (f-f_s)\} \right] \right\}$$

$$+ \frac{1}{2} \left\{ e^{-2\pi\delta f \tau_d} \delta(f+f_s) + \frac{\delta f}{\pi \{(f+f_s)^2 + \delta f^2\}} \left[1 - e^{-2\pi\delta f \tau_d} \{\cos2\pi\tau_d (f+f_s) + \frac{\delta f}{f} \sin2\pi\tau_d (f+f_s)\} \right] \right\}$$

$$(3.2.9)$$

with a leading multiplicative constant of $2R_o^2 P_i P_j$. The noise power for each spectral noise component is obtained by integrating the double-sided PSD function, $\Phi(f)$, over the equivalent noise bandwidth, B, of the IF filter in the receiver[8]:

$$N_{xx} = \int_{f_s - B}^{f_s + B} \Phi_{xx}(f) \, df \ + \ \int_{-f_s - B}^{-f_s + B} \Phi_{xx}(f) \, df. \qquad (3.3.14)$$

Here, the subscript xx indicates a reference to a particular component. The cross product between the reference field and the desired channel field, (3.3.11), will produce a PSD of the form, (3.2.9), which consists of a delta function and a broadband noise pedestal. The delta function is the carrier that we desire but the noise pedestal will produce an unwanted noise component which we will call *self-generated mismatch noise* and denote by N_{RCS}. The double-sided PSD for the signal carrier is therefore

$$\Phi_{RS}(f) = R_o^2 \, P_R P_C \exp\left[-2 \frac{\tau_m}{\tau_c}\right] \delta(f-f_s)$$

$$+ R_o^2 \, P_R P_C \exp\left[-2 \frac{\tau_m}{\tau_c}\right] \delta(f+f_s) \qquad (3.3.15)$$

---

[8] Here we have assumed that the noise filtering takes place in the passband portion of the receiver. Alternatively, the received signal could be first heterodyned down to baseband and then filtered by a low pass filter (LPF). In this case, B would be the noise equivalent bandwidth of the LPF.

where τ_m is the unavoidable mismatch delay that occurs in the "matched path". R_o is the responsivity of the photodetector and P_R and P_C are the received average reference and channel powers[9], respectively. Recall that the coherence time of the laser, $\tau_c = \dfrac{1}{\pi\delta f}$.

Performing the integration as in (3.3.14), the carrier power is obtained as

$$S = 2R_o{}^2\, P_R P_C \exp\left[-2\frac{\tau_m}{\tau_c}\right].$$

(3.3.16)

The self-generated mismatch noise PSD is given by

$$\Phi_{RCS}(f) =$$

$$R_o{}^2\, P_R P_C\, \frac{\delta f}{\pi\{(f-f_s)^2 + \delta f^2\}}\, [1 - e^{-2\pi\delta f\tau_m}\{\cos 2\pi\tau_m(f-f_s) + \frac{\delta f}{f}\sin 2\pi\tau_m(f-f_s)\}]$$

$$+\ R_o{}^2\, P_R P_C\, \frac{\delta f}{\pi\{(f+f_s)^2 + \delta f^2\}}\, [1 - e^{-2\pi\delta f\tau_m}\{\cos 2\pi\tau_m(f+f_s) + \frac{\delta f}{f}\sin 2\pi\tau_m(f+f_s)\}]\ (3.3.17)$$

and the noise power, N_{RCS}, must be determined by numerical integration of (3.3.14) where (3.3.17) is the integrand.

By design, the delay time, τ_d, is always much larger than the coherence time of the source in a CM system. As indicated in Section 3.2, (3.2.8) reduces to (3.2.11) under this condition. The PSD for the channel-channel cross product interference noise is therefore

$$\Phi_{CC}(f) = 2R_o{}^2\, P_C{}^2 \left\{\delta(f)\exp\left[-2\frac{\tau_d}{\tau_c}\right] + \frac{\delta f}{\pi\{f^2 + \delta f^2\}}\right\}.$$

(3.3.18)

---

[9] For the rest of the analysis in this thesis, it is assumed that all received average optical channel powers are made equal to a quantity which will be denoted by P_C and called the channel power. Specifically, $P_1 = P_2 = ... = P_N = P_C$ where N = no. of channels.

Note that this particular beatspectrum, (3.3.18) has its center frequency at f=0. Solving the noise integral we obtain

$$N_{CC} = 4R_o{}^2\, P_C{}^2\, \frac{1}{\pi} \tan^{-1}\left[\frac{2B}{\delta f + \dfrac{f_s{}^2}{\delta f} - \dfrac{B^2}{\delta f}}\right] \tag{3.3.19}$$

with the restriction that $\delta f^2 + f_s{}^2 > B$. Assuming that $B \ll \delta f$, (3.3.19) reduces to

$$N_{CC} = 4R_o{}^2\, P_C{}^2\, \frac{1}{\pi}\left[\frac{2B}{\delta f + \dfrac{f_s{}^2}{\delta f}}\right]. \tag{3.3.20}$$

The PSD for the reference-channel cross product interference noise is given by

$$\Phi_{RC}(f) = R_o{}^2\, P_R P_C\,\left\{\delta(f\text{-}f_s)\exp\left[-2\frac{\tau_d}{\tau_c}\right] + \frac{\delta f}{\pi\{(f\text{-}f_s)^2 + \delta f^2\}}\right\}$$

$$+ R_o{}^2\, P_R P_C\,\left\{\delta(f\text{-}f_s)\exp\left[-2\frac{\tau_d}{\tau_c}\right] + \frac{\delta f}{\pi\{(f\text{+}f_s)^2 + \delta f^2\}}\right\}. \tag{3.3.21}$$

Solving the noise integral we obtain

$$N_{RC} = 2R_o{}^2\, P_R P_C\,\left\{\exp\left[-2\frac{\tau_d}{\tau_c}\right] + \frac{2}{\pi}\tan^{-1}\left[\frac{B}{\delta f}\right] + \frac{1}{\pi}\tan^{-1}\left[\frac{2B}{\delta f + \dfrac{4f_s{}^2}{\delta f} + \dfrac{B^2}{\delta f}}\right]\right\} \tag{3.3.22}$$

Assuming that $B \ll \delta f$, (3.3.22) reduces to

$$N_{RC} = 2R_o{}^2\, P_R P_C\,\left\{\exp\left[-2\frac{\tau_d}{\tau_c}\right] + \frac{2B}{\pi\delta f} + \frac{1}{\pi}\left[\frac{2B}{\delta f + \dfrac{4f_s{}^2}{\delta f}}\right]\right\}. \tag{3.3.23}$$

The cross-product spectral components are uncorrelated with each other. As a result, the total noise power is obtained by the linear superposition of the individual noise powers. Using the results from Table 3.1, an expression is easily obtained for the system carrier to interference noise ratio, CNR_I.

$$CNR_I = \frac{S}{N_{RCS} + (N-1)N_{RC} + \left[\frac{N^2-N}{2}\right] N_{CC}} \qquad (3.3.24)$$

where N is the number of simultaneously transmitting channels in the system. Substitution of expressions (3.3.20) and (3.3.23) into (3.3.24) results in the system CNR_I equation.

$CNR_I =$

$$\frac{\exp\left[-2\frac{\tau_m}{\tau_c}\right]}{\frac{N_{RCS}}{2R_o^2 P_R P_C} + (N-1)\left\{\exp\left[-2\frac{\tau_d}{\tau_c}\right] + \frac{2B}{\pi\delta f} + \frac{1}{\pi}\left[\frac{2B}{\delta f + \frac{4f_s^2}{\delta f}}\right]\right\} + \frac{(N^2-N)P_C}{P_R}\frac{1}{\pi}\left[\frac{2B}{\delta f + \frac{f_s^2}{\delta f}}\right]} \qquad (3.3.25)$$

It should be noted that the only assumptions made in the derivation of (3.3.25) were

$$B << \delta f$$

and

$$\tau_d >> \tau_c .$$

Assuming that $B << \delta f$ has three important implications:

1. The computation of (3.3.19) and (3.3.22) is greatly simplified.

2. The effect of an arbitrary ASK modulation spectrum on the width of the noise spectral components is negligible and (3.3.25) can be applied directly to an ASK CM system.

3. It allowed the time-averaged model developed by Kikuchi and Okoshi to be used to model the laser phase noise spectrum. We can alternatively think of the assumption, $B \ll \delta f$, as imposing a constraint that time averaging of the signals at the receiver must be much greater than the coherence time of the laser [3]. This will turn out to be a very realistic assumption as we will see in Chapter 4.

Some physical insight can be gained from (3.3.25) by making some simplifying assumptions. If we assume that $P_R \gg NP_C$ we have

$$CNR_1 = \frac{\exp\left[-2\frac{\tau_m}{\tau_c}\right]}{\dfrac{N_{RCS}}{2R_o{}^2 P_R P_C} + (N-1)\left\{\dfrac{2B}{\pi\delta f} + \dfrac{1}{\pi}\left[\dfrac{2B}{\delta f + \dfrac{4f_s{}^2}{\delta f}}\right]\right\}} \qquad (3.3.26)$$

If $f_s \ll \delta f$, (3.3.26) reduces to

$$CNR_1 = \frac{\exp\left[-2\frac{\tau_m}{\tau_c}\right]}{\dfrac{N_{RCS}}{2R_o{}^2 P_R P_C} + (N-1)\dfrac{4B}{\pi\delta f}} \qquad (3.3.27)$$

If we further assume that $N > 10$, the noise power contribution of N_{RCS} will be negligible with respect to the interference power generated by the other channels. We can also assume that $(N-1) \cong N$. Hence, for $N > 10$ we have

$$CNR_1 = \frac{\exp\left[-2\frac{\tau_m}{\tau_c}\right]}{N\dfrac{4B}{\pi\delta f}}$$

$$= \frac{\pi\delta f \exp\left[-2\frac{\tau_m}{\tau_c}\right]}{4NB} \qquad (3.3.28)$$

If we further assume that the "matched" path is perfectly matched (i.e. $\tau_m = 0$), we have the simple relation

$$CNR_I = \frac{\pi\delta f}{4NB} \qquad (3.3.29)$$

which is essentially the upper bound on performance in this system[10] for perfectly matched paths. In the case where the paths are not perfectly matched, (3.3.28), we find that for any given value of mismatch length, L_m, there is an optimum value of linewidth which maximizes the CNR_I. (3.3.28) can be rewritten as

$$CNR_I = \frac{\pi\delta f \exp\left[-2\frac{L_m}{L_c}\right]}{4NB} \qquad (3.3.30)$$

where $L_m = \tau_m c/n$, $L_c = \tau_c c/n$, $\tau_c = 1/(\pi\delta f)$ and c/n equals the speed of light in the fiber. By setting the first derivative of (3.3.30), with respect to δf, equal to zero, we can solve for the value of laser coherence length, L_c, (or linewidth, δf) that will maximize the CNR_I for a given mismatch length, L_m. The resulting equation,

$$\frac{dCNR_I}{dL_c} = \left[1 - 2\frac{L_m}{L_c}\right] \exp\left[-2\frac{L_m}{L_c}\right] = 0 \qquad (3.3.31)$$

---

[10] Strictly speaking, (3.3.29) is the upper performance bound for the system assuming that $\delta f \gg f_s$. If, instead, we have $\delta f \ll f_s$, (3.3.29) becomes $CNR_I = \pi\delta f/(2NB)$. The use of the more conservative expression, (3.3.29), is due to practical considerations: keeping the heterodyne carrier frequency relatively low and assuring compatibility with practical A/O modulator devices.

has one solution at $L_m/L_c = 0.5$ and another at $L_m/L_c = $ infinity. The solution at $L_m/L_c = $ 0.5 is the one which maximizes the CNR_I and provides the optimum linewidth, δf_{opt}. Figure 3.7 shows a graph of CNR_I' plotted as a function of linewidth for $L_m = 0.01$ m.
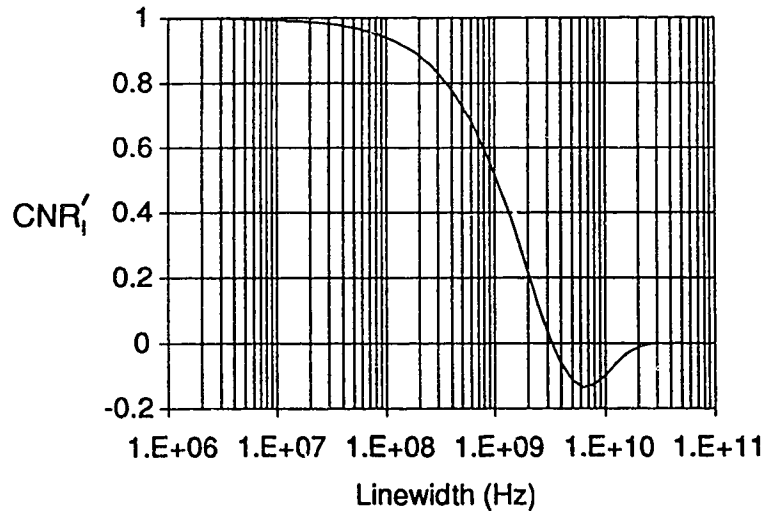
Figure 3.7 First derivative of CNR_I (with respect to coherence length) as a function of linewidth (Lm = 0.01 m.).

The optimum linewidth is given by

$$\delta f_{opt} = \frac{c}{2\pi n L_m}$$

(3.3.32)

where c/n is the speed of light in the fiber. In Figure 3.7, δf_{opt} occurs where the slope of the curve is negative and crosses the linewidth-axis. Note that below this value of linewidth, an increase in linewidth leads to an increase in CNR_I while above this value, an increase in linewidth causes a *decrease* in CNR_I. If we substitute (3.3.32) into (3.3.30) we obtain

$$CNR_{1\ (opt.)} = \frac{c\ e^{-1}}{8\ n\ L_m\ N\ B} \qquad (3.3.33)$$

which gives us the maximum CNR_1 obtainable for a given mismatch length.

3.4 Laser Intensity Noise

While fluctuations in the laser field amplitude have negligible effect on the width of the laser power spectrum, their contribution to system amplitude noise can be significant and must be included in the system CNR relation. Laser intensity noise is generally classified as *relative intensity noise* (RIN) [19] and is defined as

$$RIN = \frac{\{\Delta P^2(f)\}}{<P_o>^2} \qquad (3.4.1)$$

where $\{\Delta P^2(f)\}$ is the spectral density of the mean-square deviation of the light output of the laser (W^2/Hz) and $<P_o>$ is the average light intensity of the laser (W). The units of RIN are Hz^{-1}. The level of RIN is dependent upon such factors as the laser bias current, external optical feedback and frequency. RIN, therefore, is usually specified at a specific frequency and bias current.

At the output of the receiver's photodetector, RIN is observed as a fluctuation about the average photocurrent, I_o, and (3.4.1) can be rewritten as

$$RIN = \frac{\{i_L^2\}}{I_o^2} \qquad (3.4.2)$$

where $\{i_L^2\}$ is the mean-squared noise current density introduced by the laser [19]. CNR due to laser noise is given by

$$CNR_{Tx} = \frac{<i_s^2>}{B\{i_L^2\}} = \frac{<i_s^2>}{B \cdot RIN \cdot I_o^2}$$ (3.4.3)

where

$$<i_s^2> = <4 R_o^2 P_R P_C \cos^2(2\pi f_s t)>$$
$$= 2 R_o^2 P_R P_C$$ (3.4.4)

and

$$I_o^2 = R_o^2 (P_R + NP_C)^2$$ (3.4.5)

Note that as in section 3.3.2, we have assumed in (3.4.5) that all other interfering channels transmit a continuous wave (CW) signal. We therefore have

$$CNR_{Tx} = \frac{2 P_R P_C}{B \cdot RIN (P_R + NP_C)^2}$$ (3.4.6)

It is convenient at this point to define a parameter, Γ, which will be called the *channel/reference power ratio* where

$$\Gamma = \frac{P_C}{P_R}$$ (3.4.7)

(3.4.6) can then be written as

$$CNR_{Tx} = \frac{2 \Gamma}{B \cdot RIN (1 + N\Gamma)^2}$$ (3.4.8)

If we assume that $P_R \gg NP_C$, (3.4.8) further reduces to

$$CNR_{Tx} = \frac{2\Gamma}{B \cdot RIN} \qquad (3.4.9)$$

3.5 Receiver Noise

The two main sources of noise in the receiver are photodetector shot noise and amplifier noise.

3.5.1 Shot Noise

In Section 3.3 we determined that the "D.C." optical components incident on the photodetector were the terms appearing along the diagonal of Figure 3.5. The mean photocurrent is therefore given by

$$I_{ph} = <i_{ph}> = R \left[\frac{E_R{}^2}{2} + \frac{E_1{}^2}{2} + ... + \frac{E_N{}^2}{2} \right]$$

$$= R \left[\frac{E_R{}^2}{2} + N \frac{E_C{}^2}{2} \right]$$

$$= R_o (P_R + NP_C) \qquad (3.5.1)$$

since channel powers are equal. Note that, as in section 3.3.2, we have assumed in (3.5.1) that all other channels transmit a continuous series of 1's. R_o is the responsivity of the photodetector and R includes the responsivity and the constants necessary in the conversion from watts to $(V/m)^2$. Hence, $R = R_o/\eta$ where η is the intrinsic impedance of the photosensitive region. The shot noise power is given by

$$<i_{sh}{}^2> = 2q(I_{ph} + I_d)B \qquad (3.5.2)$$

Where q = the electronic charge, 1.6 x 10^{-19}, and I_d is the dark current of the photodetector. Substituting (3.5.1) into (3.5.2), we obtain

$$< i_{sh}^2 > = 2q\{R_o (P_R + NP_C) + I_d\}B \qquad (3.5.3)$$

3.5.2 Amplifier Noise

Amplifier noise is due to various sources. Shot and thermal noise is produced in semiconductor components. Resistors generate thermal noise. These various noise components are usually lumped together and the noise performance of an amplifier given as an equivalent input noise voltage or current. In the case of a photoreceiver, amplifier noise is usually reflected back to the output of the photodetector and expressed as an equivalent noise current. The amplifier noise power is then given by

$$< i_a^2 > = \{i_a^2\} B \qquad (3.5.4)$$

where $\{i_a^2\}$ is an equivalent single-sided, frequency independent (white) amplifier input noise current PSD.

3.5.3 Receiver Carrier to Noise Ratio (CNR)

Receiver CNR is given by

$$CNR_{Rx} = \frac{< i_s^2 >}{< i_{sh}^2 > + < i_a^2 >} \qquad (3.5.5)$$

Using (3.4.4), (3.5.3) and (3.5.4), we obtain

$$CNR_{R_\tau} = \frac{2 R_o^2 P_R P_C}{2q\{R_o (P_R + NP_C) + I_d\}B + \{i_a^2\} B}$$

$$= \frac{2 R_o^2 P_R P_C}{[2q\{R_o (P_R + NP_C) + I_d\} + \{i_a^2\}] B} \tag{3.5.6}$$

If we make P_R sufficiently strong such that the shot noise dominates over thermal noise we have

$$CNR_{Rx} = \frac{R_o P_C}{q (1 + N\Gamma) B} \tag{3.5.7}$$

If $P_R \gg NP_C$, (3.5.7) reduces to

$$CNR_{Rx} = \frac{R_o P_C}{qB} \tag{3.5.8}$$

3.6 System CNR Equation

A CNR equation which characterizes performance for the entire CM system can be now developed by combining the results of Sections 3.3, 3.4 and 3.5. Writing the system CNR in terms of the interference CNR, the transmitter CNR, and the receiver CNR, we obtain [20]:

$$\frac{1}{CNR_{sys}} = \frac{1}{CNR_I} + \frac{1}{CNR_{Tx}} + \frac{1}{CNR_{Rx}} \tag{3.6.1}$$

This is final system CNR equation and will be used to predict CM system performance in Chapter 4.

3.7 SNR$_i$ of a Digital OOK CM System

The signal to interference noise ratio for a simple digital OOK CM system can now be obtained from our CNR expressions. To simplify the treatment, we ignore the effects of transmitter noise and receiver noise, considering only interference noise. In a CM system which supports a large number of transmitter channels, interference noise will generally be dominant and this is a realistic assumption.

The composite interference noise generated at the receiver will be the sum of the individual interference noise components generated by all of the interfering channels. We assume a large number of interfering channels, and therefore assume that the total interference noise generated by interfering channels has a Gaussian probability density function (PDF) by way of the central limit theorem.

In each transmitter we send an NRZ "1" bit by applying maximum RF power to the A/O modulator for a duration of one bit time. Conversely, an NRZ "0" bit is sent by removing RF power from the A/O modulator for the same duration. For the worst case condition, *we assume that no line coding is used and that all interfering channels transmit a continuous series of 1's*. We modulate the signal carrier with a 100% modulation depth and assume an equal probability of 1's and 0's.

$i_S, i_N \longrightarrow \bigotimes \longrightarrow$

$LO \;\bigcirc\!\!\!\!\!\sqrt{\ }$

$\sqrt{2} \cos (\omega_s t + \phi)$
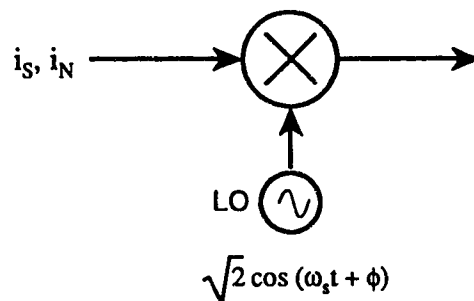
Figure 3.8 Electrical mixer block diagram

At the receiver (following the photodetector), we multiply the component of the photocurrent that represents the desired signal,

$$i_s = 2 R_o \sqrt{P_R P_C} \cos(\omega_s t + \phi) \qquad (3.7.1)$$

with the local oscillator (LO) signal,

$$i_{LO} = \sqrt{2} \cos(\omega_s t + \phi) \qquad (3.7.2)$$

and obtain the mixer output signal,

$$i_{SO} = s(t)\sqrt{2} \, R_o\sqrt{P_R P_C} + s(t)\sqrt{2} \, R_o\sqrt{P_R P_C} \cos(2\omega_s t + 2\phi) \qquad (3.7.3)$$

where we have assumed that the phase of the LO signal is locked to that of the heterodyne carrier signal. s(t) is the OOK modulation signal and has a value of 1 or 0. The amplitude of the LO signal (3.7.2) has been chosen such that the amplitude of the interference noise power at the input and at the output of the mixer are equal. The baseband waveform that appears at the output of the mixer is shown in Figure 3.9. Since, $P_R \gg P_C$, interference noise power is not dependent upon the signal amplitude and the optimum level for the decision threshold, i_{th}, is halfway between the "1" level and the "0" level at the position indicated [21].
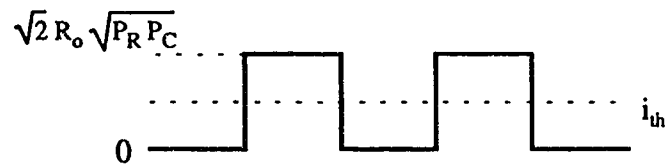
Figure 3.9 Baseband NRZ signal waveform.

We define the following parameter

$$x = \frac{i_p - i_{th}}{\sigma} = \frac{\frac{R_o}{\sqrt{2}}\sqrt{P_R P_C}}{\sigma} \qquad (3.7.4)$$

where σ is the rms noise current and i_p is the peak value of the signal at the sampling instant. If we assume an equal probability of one's and zero's and a Gaussian noise probability density function (PDF), we can obtain the bit error rate (BER) as

$$BER = Q(x) \qquad (3.7.5)$$

where $Q(x)$ is the standard Q-function. Squaring x, we obtain,

$$x^2 = \frac{R_o^2 P_R P_C}{2\sigma^2} \qquad (3.7.6)$$

The carrier power at the input to the mixer is $2R_o^2 P_R P_C$. It can be shown that

$$CNR_I = \frac{2R_o^2 P_R P_C}{\sigma^2} \qquad (3.7.7)$$

Using (3.7.6) and (3.7.7) we obtain

$$x^2 = \frac{CNR_I}{4} \qquad (3.7.8)$$

For a BER of 10^{-9}, $x = 6$. Hence, $CNR_I = 144$ (21.6 dB). Using the optimized expression (3.3.33), we obtain the following relation:

$$144 = \frac{c}{n} \frac{e^{-1}}{8 L_m N B} \qquad (3.7.9)$$

We now assume a 1st order low pass filter (LPF) at the output of the mixer for our receiver noise filter. For this filter, the bit rate, R can be less than or equal to the noise equivalent bandwidth of the filter, B, without introducing significant eye closure [22]. An eye diagram was simulated for a 1st order LPF using 70 non-return-to-zero (NRZ), 10 bit sequences and is shown in Figure 3.10. The LPF corner frequency is set to 0.64 of the bit rate R which corresponds to B = R. This implies that R must be less than or equal to 0.64 of the LPF corner frequency.
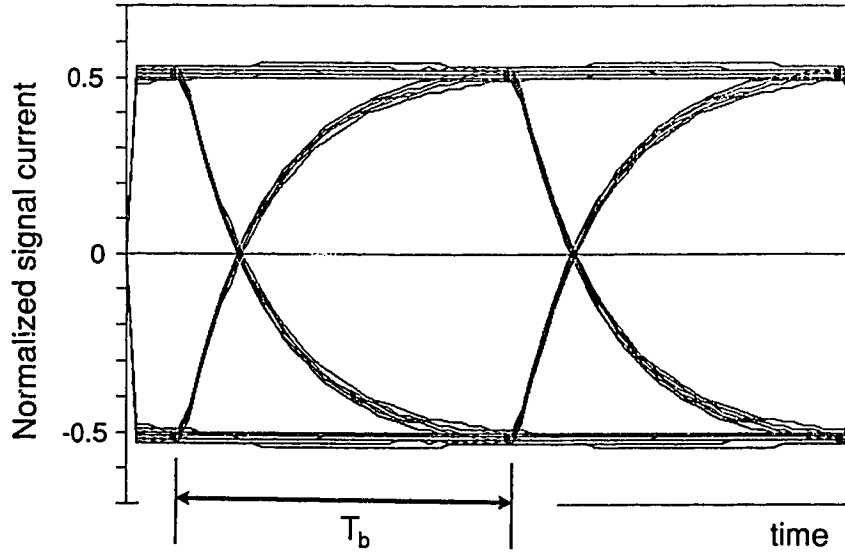
Figure 3.10 Signal eye diagram for a first order LPF with bit rate, R, equal to the filter noise equivalent bandwidth, B.

We can now rewrite (3.7.9) as

$$N \cdot R = \frac{(66,529)}{L_m}$$

(3.7.10)

where N·R is the product of the number of channels, N, and the per-channel bit rate, R. (3.7.10) indicates that the mismatch length imposes a fundamental limit on the maximum system capacity and that there is a tradeoff between the number of channels, N, and the

per-channel bit rate. Values of N·R are tabulated for various assumed values of mismatch

length in Section 4.7.

4. RESULTS

4.1 Experimental Setup

The experimental setup shown in Figure 4.1 was used to obtain experimental data for this thesis. The architecture matches that of the two channel CM system discussed in section 3.3 but excludes the receiver's RF local oscillator, mixer and noise filter.

The head end laser was a Hitachi HL1341 InGaAsP DFB semiconductor laser operating at a nominal wavelength of 1.3 μm. The temperature of the laser chip was maintained at a constant 25°C by a thermoelectric cooler (TEC) and thermistor based feedback circuit. The output beam of the laser was collimated by an anti-reflection (AR) coated, 0.22 pitch, plano-convex GRIN lens. The plano-convex lens has a convex face at one end which faces the laser, increasing the NA of the lens and improving coupling to the laser output. Laser to fiber coupling efficiencies as high as 35 % were obtainable with this configuration but were not stable for more than a minute or so. Typical coupling efficiencies were around 20 - 25 %.

The analysis of Schunk and Petermann [23] shows that, for a certain single-mode laser diode, levels of external feedback greater than -40 dB result in monotonically increasing levels of RIN. In addition, it is well known that the spectral characteristics are strongly influenced by external feedback [19]. When setting up the experiment, it was found that two stages of optical isolation were required to avoid substantially altering the laser's spectral characteristics. The collimated beam of the laser was therefore passed through two optical isolators in series providing a total return loss of better than 50 dB.

The output of the isolators was collected by a Newport AR coated 40X[1] microscope objective lens (NA = 0.65, focal length = 4.3 mm, single-layer AR coated) and coupled to a single-mode fiber (SMF) mode stripper which was included to prevent the propagation of cladding modes in the fiber. The mode stripper was constructed by removing the plastic coating from a portion of the input fiber, forming a 90° bend of radius 2 cm, and immersing the bend in fiber core index matching epoxy. The output of the mode stripper was fusion spliced to the input of Coupler #1.

The A/O modulators (IntraAction Corp AOM-40N) consisted of packaged, bulk devices with broadband anti-reflection (AR) coated faces. Newport 40X objective lenses were used on both sides of the A/O modulators. The input beam to each A/O modulator was oriented at the Bragg angle[2] (6.7 mrad or 0.38°) in an upshifted[3] configuration. Fine adjustment was achieved by applying approximately 4 watts of RF power to each modulator and varying the input beam angle until the light intensity in the first diffraction order was maximized. The zeroeth order was then masked off and the output fiber was coupled to the first order diffracted beam through an objective lens. Newport F-915 single mode fiber coupler stages were used to position the fiber and objective lens and greatly improved beam-to-fiber coupling efficiency and long-term stability over the use of X-Y-Z positioners. Using this configuration, a stable insertion loss (assuming a diffraction efficiency of 100%) as low as 4.5 dB was obtained. Typical values were around 5 dB. The frequency of the modulator RF carrier was set to 40 Mhz and RF drive power was variable from 0 - 5.5 watts for channel #1 (using the ME-40R driver) and 0 - 4 watts for channel #2 (using the DE-40B driver). By varying the input voltage to the

---

[1] The fiber mode field diameter was calculated to be 9.2 µm (dia.) using the expression in [24]. The Newport 40X objective lens provides a 0.77 mm beam waist diameter at the lens for a 9.2 µm beam waist diameter at the fiber face.
[2] See Appendix A for the definition of Bragg angle.
[3] See Appendix A for an explanation of the upshifted configuration.

53
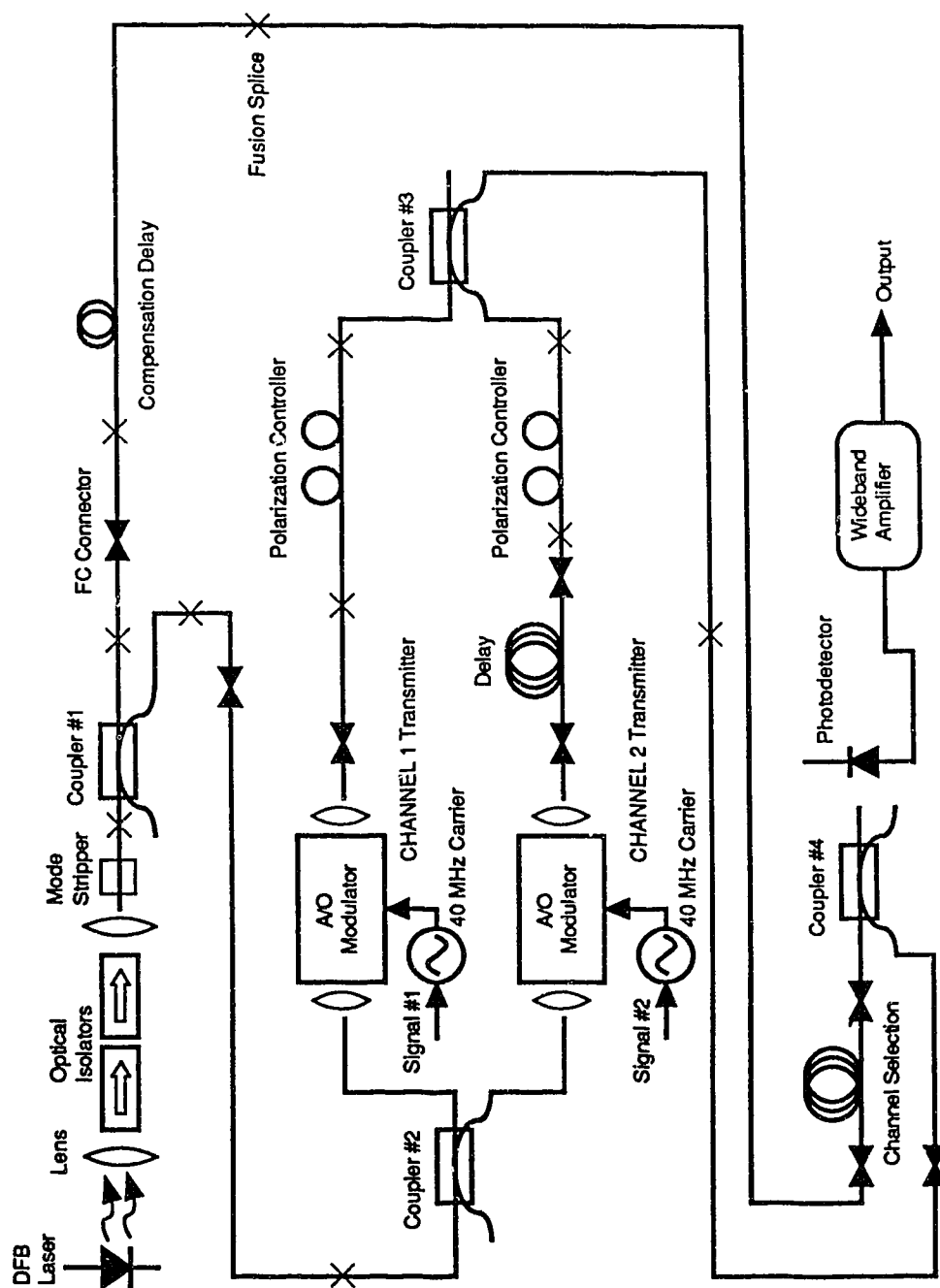
Figure 4.1 Experimental two-channel system.

drivers, the amplitude of the RF carrier power applied to each A/O modulator could be varied. This allowed the intensity of the light in the first diffraction order of each device to be varied. The measured diffraction efficiency[4] (see Appendix A), as a function of RF drive power, (channel #1) has been plotted as a series of discrete data points in Figure 4.2. The continuous curve is a plot of the theoretical diffraction efficiency expression, $\sin^2 (K \sqrt{P_a})$ [12] where K has been experimentally determined to be 0.43 for this particular modulator. Here K is comprised of several constants and P_a is the RF power applied to the modulator.
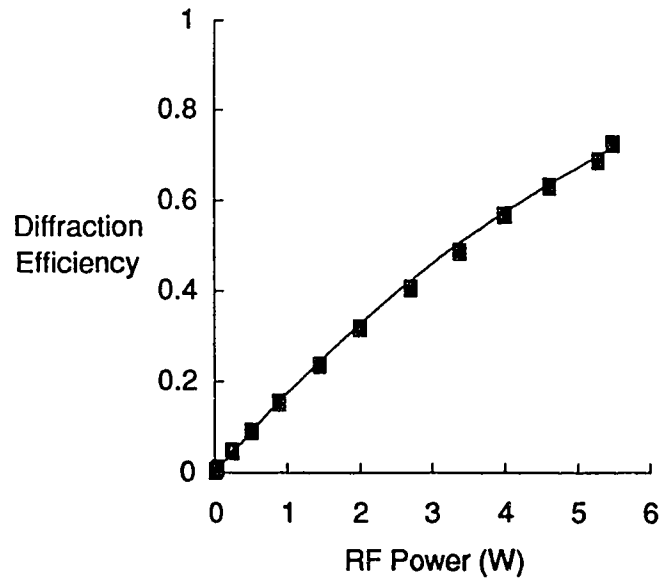
Figure 4.2 A/O modulator transfer characteristic. Measured data is plotted as discrete points while the theoretical function is shown as a continuous curve.

While RF power to the modulators could be varied with a front panel control, it was also possible to intensity modulate the RF output of the A/O drivers with an input voltage. The DC transfer characteristic of the channel #1 A/O driver was measured and plotted in

---

[4] If we assume no static losses in the device, diffraction efficiency can be loosely defined as the ratio of the intensity in the first diffraction order to the intensity of the incident input light.

Figure 4.3 as a series of discrete points. P_a is the RF output power of the driver which drives the A/O modulator and V_{in} is the driver input DC voltage. A fifth-order polynomial was fitted to the data and appears as a continuous curve in Figure 4.3. The fitting function is $P_a = 0.00676 - 0.440 \ V_{in} + 8.27 \ V_{in}^2 - 4.92 \ V_{in}^3 + 4.24 \ V_{in}^4 - 2.47 \ V_{in}^5$ where P_a is in watts and V_{in} is in DC volts.
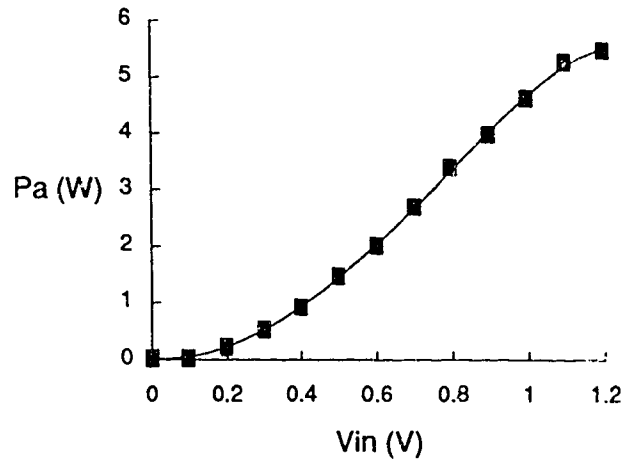
Figure 4.3 Transfer function for A/O driver. Measured data is plotted as discrete points while the fitting function is shown as a continuous curve.

The modulation bandwidth[5] of the A/O modulators was estimated to be 4 MHz (assuming a spot size of 0.8 mm). Modulation bandwidths of the A/O drivers was specified to be 10 MHz.

Polarization controllers were constructed from specifications published by Koehler and Bowers [25]. Each controller consisted of two 0.75" diameter fiber loops in series which were individually rotatable. This allowed the state of polarization (SOP) of the light from each A/O modulator to be closely matched to that of the reference light at coupler #4. The reference to channel SOP matching was maximized by observing the heterodyne carrier or interference noise on an oscilloscope and rotating the fiber loops until the signal amplitude was maximized. This adjustment procedure was executed

---

[5] See Appendix A for a definition of modulation bandwidth.

whenever fiber lengths were altered or the setup was otherwise disturbed. It was found that, once adjusted, the SOP of the channel paths and the reference path were quite stable over long periods of time.

All directional couplers/splitters were Canstar single-mode fiber directional couplers. Couplers in the system had the following coupling ratios (see Figure 4.1):

Coupler #1:   Reference arm = 76.6% of coupler input.

Input of Coupler #2 = 23.4% of coupler input

Coupler #2:   A/O modulator Ch #1   = 51% of coupler input.

A/O modulator Ch #2   = 49% of coupler input.

Coupler #3:   Output = 50.5% of channel #1 + 49.5% of channel #2.

Coupler #4:   Output = 47.5% of channel bus + 52.5% of reference bus.

All permanent fiber connections were fusion spliced with a Northern Telecom automated fusion splicer. Typical insertion loss for these fusion splices was around 0.2 dB. Fusion splice locations are shown in Figure 4.1.

Temporary fiber connections in the system were implemented with non-physical contact FC type connectors. While insertion loss for these connectors is nominally specified as 0.5 dB, losses as high as 5 dB were actually observed during the experiment. While not measured, it was assumed that the return loss for these connectors could be as low as 9 dB (13%) due to the existence of two fiber core-air interfaces.

For the photodetector, two different devices were used. Wideband spectral measurements (10 MHz - 1 GHz) were taken using an Antel AR-G20 germanium avalanche photodiode (APD) which had a signal bandwidth of several GHz. Due to its extremely small photosensitive area (.002 mm^2), light from the output fiber of coupler #4 was coupled to the APD through a 0.23 pitch GRIN lens.

For low speed measurements (0 - 200 MHz) or where it was necessary to know the responsivity of the detector accurately, a calibrated Fujitsu FID13S81WS InGaAsP PIN photodiode was electrically terminated and used as the photodetector (see Figure 4.14 for a detailed circuit schematic). In this case the output fiber was butt coupled to the photosensitive area.

Two different post-detector amplifiers were used. For low speed measurements, (0 - 200 MHz) two amplifiers constructed by a colleague [26] at ATRC were used in series. The S parameters and noise spectrum of the series combination were measured and provided a total forward midband gain of 44 dB, a 6 dB noise figure, a lower corner frequency of less than 300 kHz and an upper corner frequency of 1.05 GHz. For high speed measurements (0 - 1 GHz), an amplifier constructed by another colleague was used [18]. This measured characteristics of this amplifier yielded a 36 dB midband gain, 6dB noise figure, lower corner frequency of 7 MHz and an upper corner frequency of 1.7 GHz. Both amplifiers exhibited flat midband response with very little ripple.

An HP71000 series spectrum analyzer was used to measure the amplified photocurrent spectra while a Tektronix 2465A (350 MHz) oscilloscope was used to observe time domain waveforms (see Figure 4.4). Measured data were acquired from the spectrum analyzer using an IBM PC/XT computer with an IEEE 488 interface card and "Datapro" [27] data acquisition software. An HP 8753A network analyzer and HP 85046A S-parameter test set were used to measure amplifier S-parameters.

A McPherson 270 scanning monochromator with a Stanford SR530 lock-in amplifier and Bentham 218F signal chopper were used to measure the spectral characteristics of the laser (see Figure 4.6). A Tektronix 2430 digital oscilloscope was used to store the monochromator scans and the IBM computer was used to acquire the data from the oscilloscope using the "Sigpro" [27] data acquisition program.
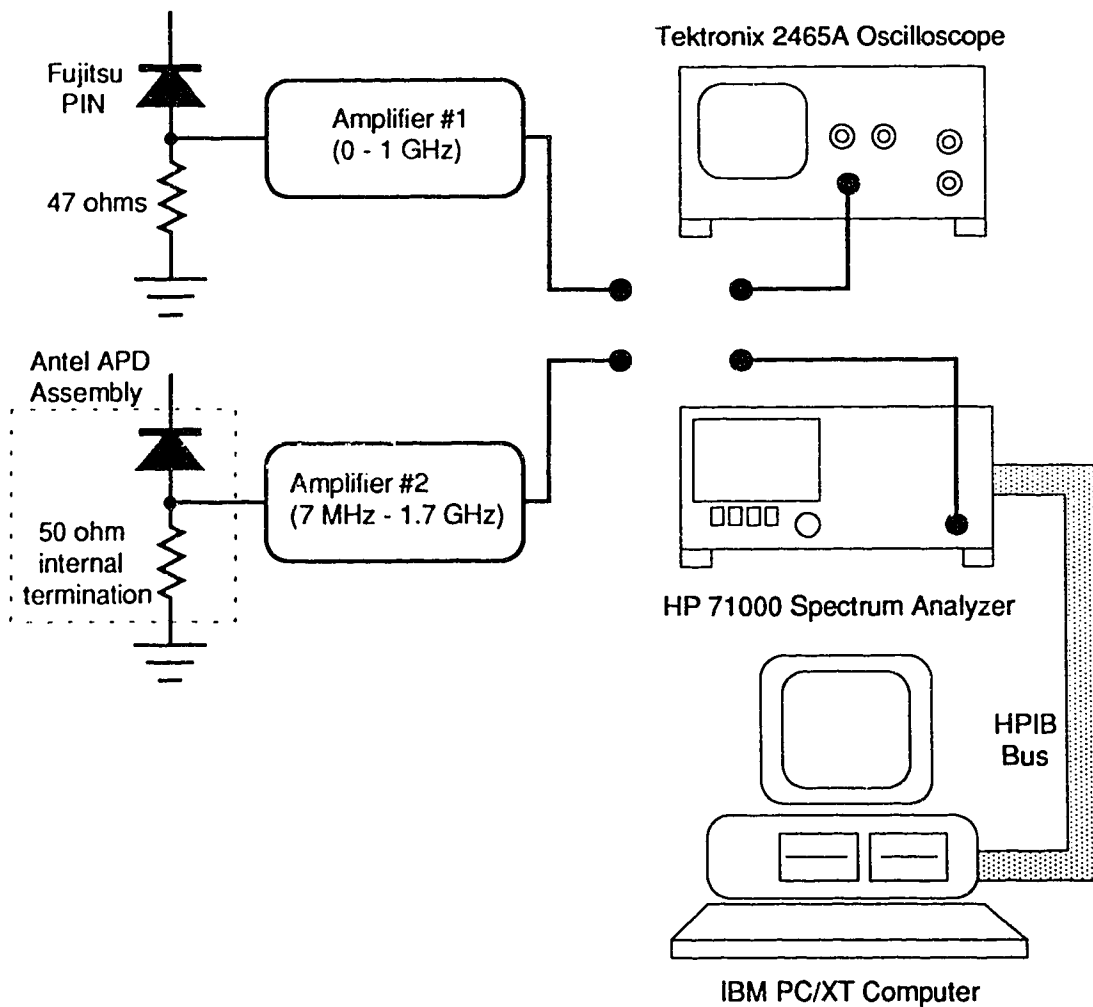
Figure 4.4 Equipment setup for measuring photocurrent beatspectra.

4.2 Laser Characteristics

4.2.1 Output Power Curve

To determine the nominal bias current for the laser diode, the front facet output power, L, vs. bias current, I_F, characteristic was measured. To determine the L vs. I_F characteristic, the intensity of the collimated light beam formed at the output of the first GRIN lens was measured as a function of forward current. The resulting curve is shown in Figure 4.5.
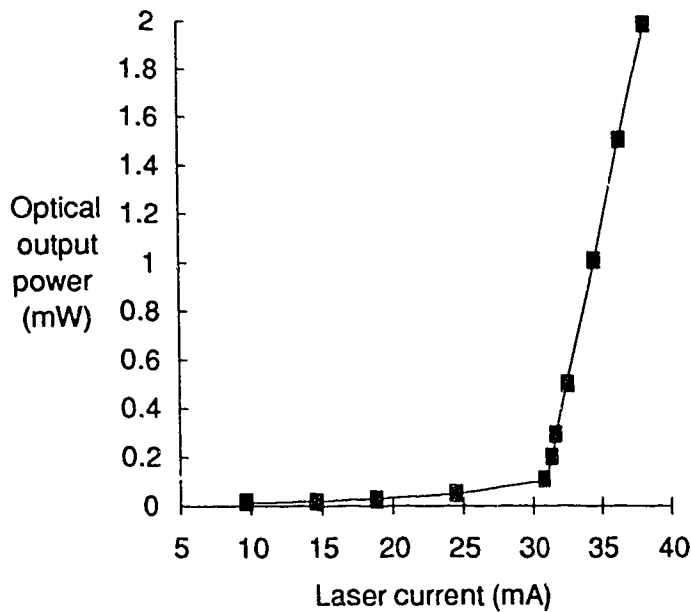
Figure 4.5 Laser optical output power as a function of forward bias current.

The threshold current, I_{th}, was observed to be 30.6 mA and a value of 36.5 mA (I_f/I_{th} = 1.2) was selected as a nominal bias current for relatively long laser life. All experimental measurements were taken at this bias level unless otherwise specified.

4.2.2 Longitudinal Mode Structure

The apparatus used to measure the laser output spectrum is shown in Figure 4.6. The scanning monochromator was used to measure the spectral characteristics of the laser at a bias current of 36.5 mA. The monochromator slit width was set to 40 μm for this measurement which yielded a measured spectral resolution (response FWHM) of 0.19 nm (34 GHz at a center wavelength of 1.3 μm). Relative output intensity as a function of wavelength is shown in Figure 4.7 where it can be seen that the spectral profile is characterized by a single dominant mode with sidemodes more than 13 dB down from the main peak. The dominant mode is situated at 1.3017 μm. The wavelength

of the dominant mode was observed to stay within a 0.14 nm window for bias currents between 32 and 40 mA.
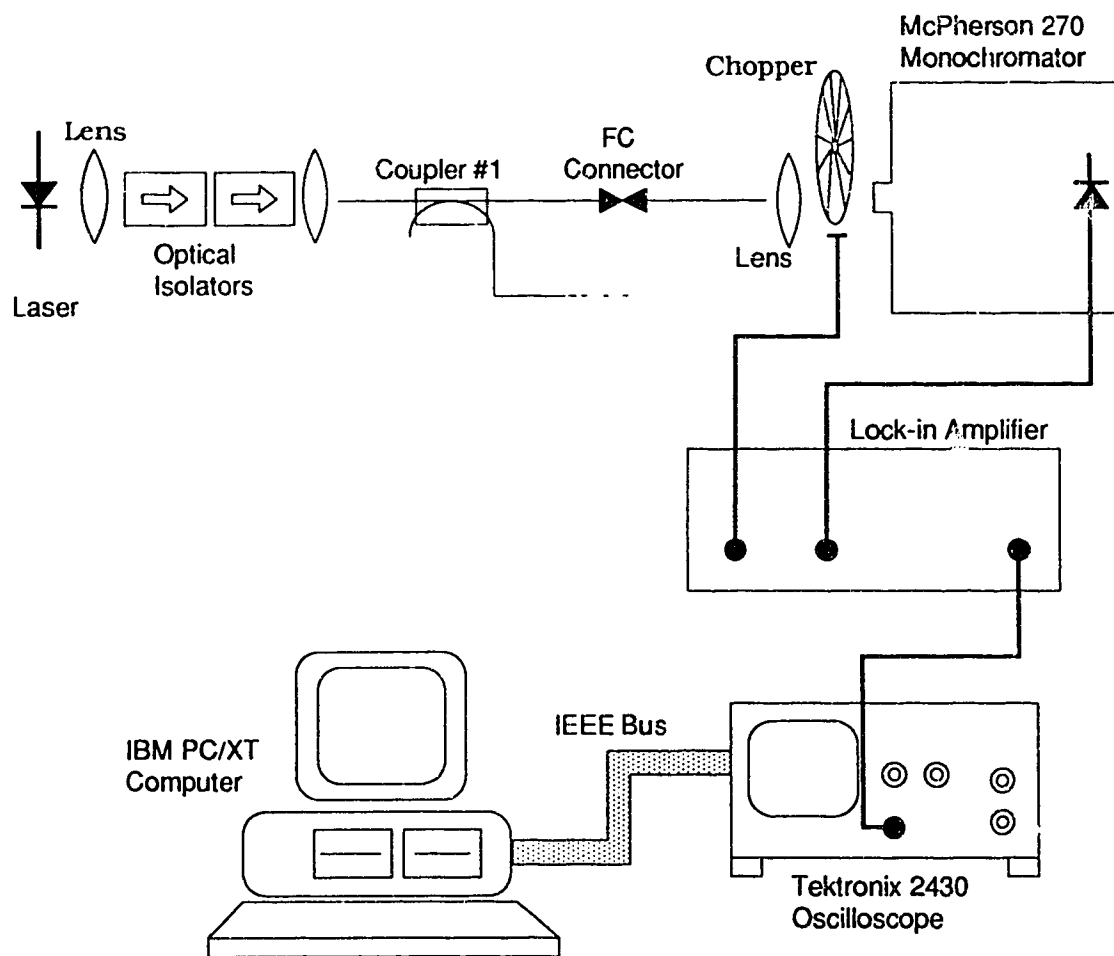
Figure 4.6 Laser spectral measurement apparatus.
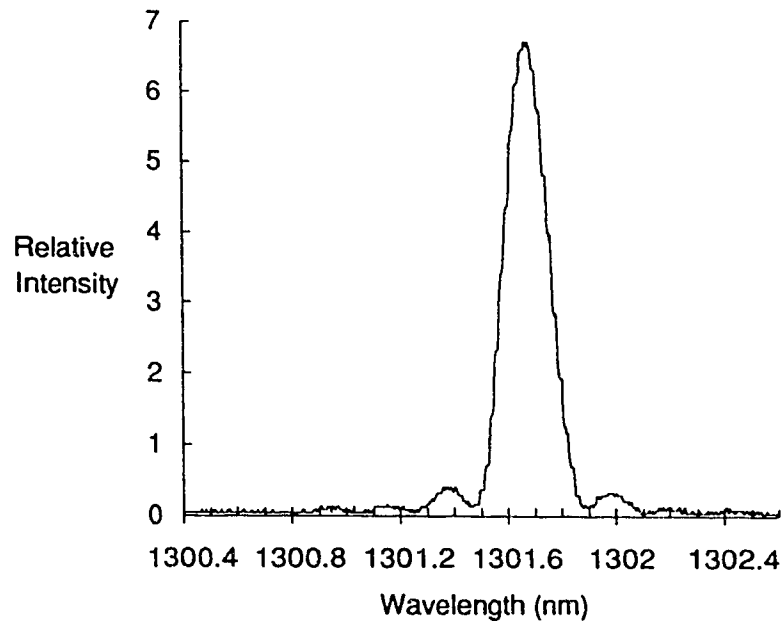
Figure 4.7 Output spectrum of the DFB laser measured by a scanning monochromator ($I_F = 36.5$ mA).

Note that the shape of the spectral lines in Figure 4.7 is strongly influenced by the response of the monochromator. At a wavelength of 1.3 µm, a linewidth of 200 MHz would correspond to 0.001 nm of wavelength. Therefore, on the scale shown in this figure, the actual laser spectral lines would appear only as very narrow spikes. To determine the lineshape of the laser some other instrument with greater resolution was obviously required. Provided that the laser spectrum is single-moded, the DSH technique of Kikuchi and Okoshi [14] is capable of providing much greater spectral resolution than that obtained with the monochromator or a scanning Fabry-Perot interferometer. Therefore, Kikuchi and Okoshi's technique, as described in the following section (4.2.3), was used to determine laser linewidth.

4.2.3 Linewidth

The setup of Figure 4.8 was used to measure the linewidth of the laser. Using channel #1 of the overall system, the apparatus was configured as a Mach-Zehnder interferometer with an A/O modulator in one arm and a 200 m. fiber delay line in the other. With a delay line length, L_d, of 200 m. the spectral resolution of this apparatus (using Kikuchi and Okoshi's approach) is approximately 520 kHz. This value was obtained by noting that for values of δf greater than $0.5/\tau_d$, the laser linewidth is given by one-half of the FWHM of the photodiode output signal current power spectrum [14]. Hence the minimum measurable linewidth is obtained by,

$$\delta f > \frac{1}{2\tau_d}$$

$$> \frac{c}{2nL_d} \qquad (4.2.3.1)$$

where c is the speed of light in vacuum, n is the refractive index of the fiber core, and L_d is the length of the delay line. For an n of 1.44 and an L_d of 200 m., δf must be greater than 520 kHz. However, smaller linewidths can be measured by curve-fitting the complete expression (3.2.9) to the measured data [28].
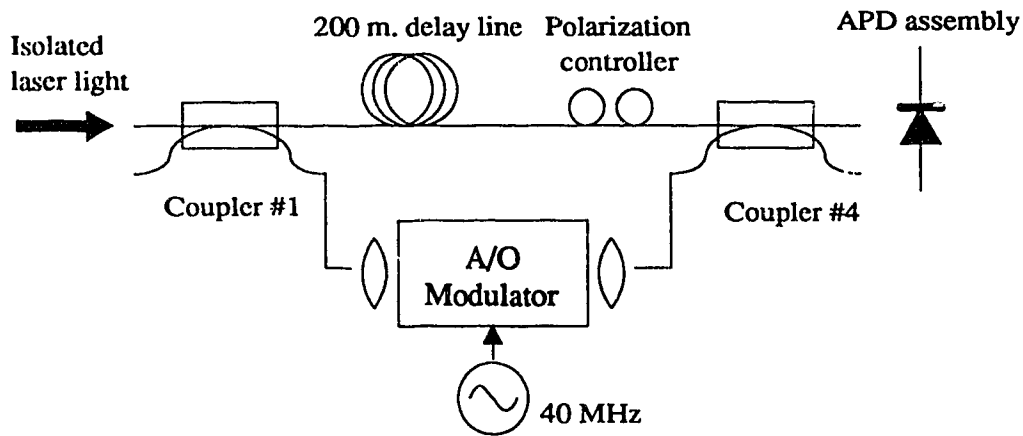
Figure 4.8 Setup for determining laser linewidth.

The output of the terminated APD was amplified with a wideband 36 dB amplifier and fed to the spectrum analyzer which was set to scan a frequency range from 0 Hz to 1 GHz. With the A/O modulator turned off, the amplifier output spectrum was scanned, effectively measuring the noise floor of the system[6]. With the A/O modulator turned on, the amplifier output spectrum was again scanned and recorded. Given that the reference power was much greater than that in the A/O path, the noise floor of the system (due to detector shot noise, amplifier noise and RIN) could then be effectively removed by numerically subtracting the results of the first scan from that of the second. The result was a beatspectrum which was essentially due only to the phase noise of the laser. The C program, *Superfit2* (see Appendix B), was written to fit (3.2.9) to the measured data by minimizing the sum of the squares of the errors. The fitting parameters were laser linewidth, δf, and the spectral amplitude.

4.2.4 Laser Relative Intensity Noise (RIN)

Relative intensity noise of the laser was measured using the configuration of Figure 4.1. Both modulators were turned off and laser bias current was maintained at 36.5 mA. The PIN assembly of Figure 4.4 and 4.14 was used in conjunction with the 44.5 dB amplifier chain and the amplified photocurrent noise spectrum was measured as a function of frequency using the spectrum analyzer. The laser RIN spectrum was then obtained by subtracting measured amplifier and theoretical shot noise floors from the photocurrent spectrum. At a frequency of 50 MHz, RIN was determined to be -117.5 dB/Hz. The RIN spectrum was observed to exhibit the characteristic amplitude peak which occurs at the relaxation resonance frequency [19]. Using the high frequency detector configuration, the

---

[6] This noise floor includes detector shot noise due to light in the reference arm, amplifier noise, and laser RIN.

resonance frequency was measured to be greater than 1.4 GHz for bias currents greater than 33.5 mA.

4.3 Laser Phase Noise Spectrum

The next step in the experiment consisted of comparing the spectral shape of the measured beatspectra produced by the 1.3 μm InGaAsP DFB laser to that predicted by the theoretical expression, (3.2.9). Richter *et al.* [28] have shown that the measured spectrum of a certain 0.82 μm, external-cavity laser closely resembles their theoretical model which has the same form as (3.2.9). Using the configuration of Figure 4.8, the photodetector beatspectrum was measured for a range of fiber delay line lengths, L_d. This was accomplished by removing the 200 m delay line and performing individual spectral scans for a 0 m, 0.59 m, 1.15 m and 20 m delay line. The ratio of reference power to channel power was maintained at approximately 10:1 so that shot and thermal noise contributions could be subtracted from the measured data. The measured beatspectra are shown in Figures 4.9 through 4.12, inclusive. Also shown on the same graphs are fitted curves having a form similar to (3.2.9). Resolution bandwidth of the spectrum analyzer was set to 300 kHz for all spectral scans in these figures.

The measured data for Figure 4.9 were obtained by removing the delay line from the system, with the intention of making $L_d = 0$. The measured data are shown by the jagged curve and the relatively high delta function at 40 MHz. The fitting function is shown by the smooth line and a delta function which is essentially overlaid with the measured spike. If the two curves were separated, it would be seen that the fitted and measured spikes have approximately the same amplitude. The fitted parameters for this case are $L_d = 0.04$ m and $\delta f = 230$ MHz. However, from estimates of mismatch error in the system, it was expected that L_d would have been less than 0.01 m. It is suspected that this discrepancy is due to optical power fluctuations that occurred between spectral scans.

These optical power fluctuations were due to the long term coupling stability problem that was noted in Section 4.1 and Appendix C.
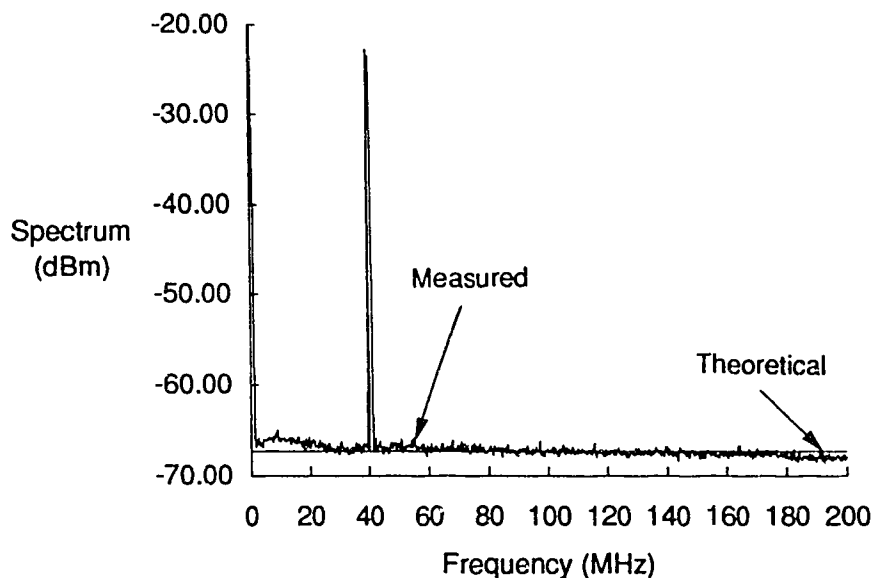
Figure 4.9 Photodetector beatspectrum for $L_d \cong 0$. Fitted parameters are $L_d = 0.04$ m., $\delta f = 230$ MHz and $L_m/L_c = 0.14$.

The beatspectrum shown in Figure 4.10 was obtained using the 0.59 m delay line. Once again, the jagged line represents the measured data while the smooth curve represents the fitting function. The fitted delta function is overlaid with the measured delta function at 40 MHz, appearing as one spike. The peak value of the measured delta function is approximately 2 dB less than that of the calculated one.

Figure 4.11 shows the measured data and fitted function for the 1.15 m delay line. While a small delta function is observed in the fitted function, it is absent from the measured spectrum.
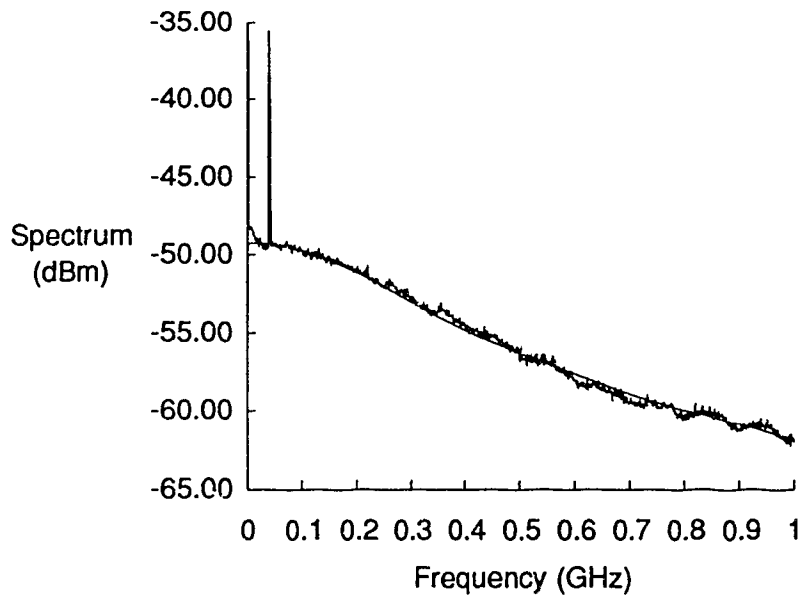
Figure 4.10 Photodetector beatspectrum for L_d = 0.59 m. Fitted parameters are L_d = 0.59m., δf = 230 MHz, and L_d/L_c = 2.0.
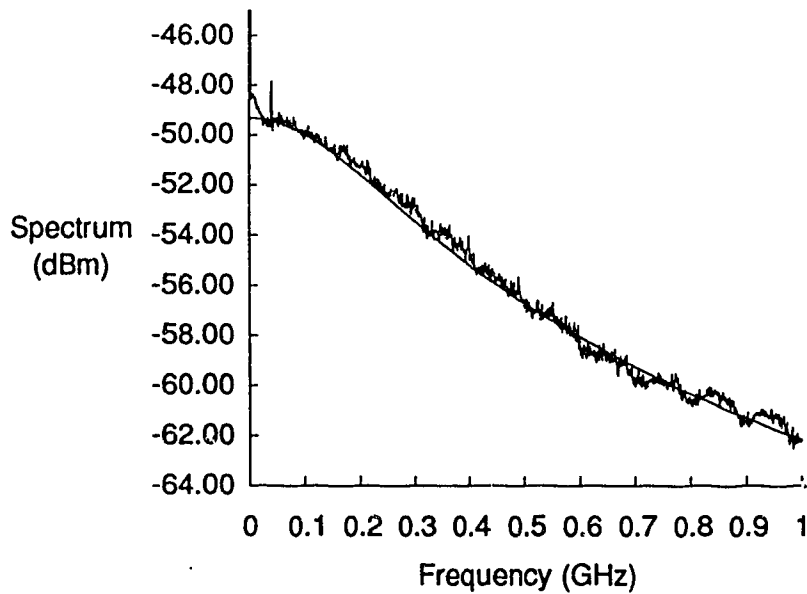
Figure 4.11 Photodetector beatspectrum for L_d = 1.15 m. Fitted parameters are L_d = 1.15 m., δf = 230 MHz, and L_d/L_c = 4.0.

Figure 4.12 shows measured and fitted spectrums for the 20 m delay line.
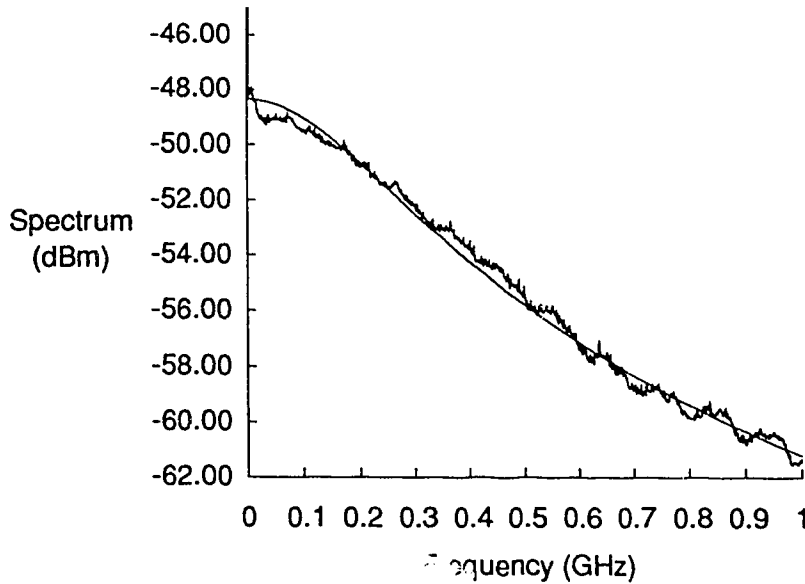
Figure 4.12 Photodetector ... for $L_d = 20$ m. Fitted parameters are $L_d = 20$
m., $\delta f = $ ... $/L_c = 69.4$.

In general, the fitting function matched the measured data for the various delay regimes reasonably well, strengthening the validity of Kikuchi and Okoshi's spectral model. Note that for the spectral measurements of Figures 4.9 through 4.12, the resolution bandwidth (RBW) of the spectrum analyzer was set to 300 kHz. The RBW is considered to be equivalent to the noise equivalent bandwidth, B, used in the analysis performed in Chapter 3. Since, the laser linewidth, δf, was nominally 230 MHz, and B was set to 300 kHz, we have $B/\delta f = 0.0013$. Hence, it must be stressed that Kikuchi and Okoshi's model has only been experimentally confirmed here for the regime where $B/\delta f < 0.0013$. It is anticipated that if the ratio, $B/\delta f$, were to be increased from this value, eventually the point would be reached where we could no longer assume time-averaging and the Kikuchi and Okoshi spectral model would break down. Fortunately, for an optimum system supporting more than a few channels, the constraint, $B/\delta f < 0.0013$, is easily satisfied. For example, in Section 4.7 it is shown that for a digital OOK CM

system, B/δf = 0.002 for a 10 channel system and B/δf = 0.0002 for a 100 channel system.

4.4 Interference Noise Correlation Between Two Channels

The next stage of the experiment sought to examine the correlation between interference noise generated by channels #1 and #2. Channel #1 was decorrelated from the reference with a 10 m delay line (L_d/L_c = 35). Channel #2 was decorrelated from the reference with a 20 m delay line (L_d/L_c = 70). The delay spacing between channels was therefore, 10 m (L_d/L_c = 35). Photodetector power spectra were then obtained individually for i) channel #1 transmitting alone, ii) channel #2 transmitting alone, and iii) channels #1 and #2 transmitting simultaneously. Data obtained from cases i) and ii) were used to determine the sum of the noise spectra that would occur for a completely correlated case and a completely uncorrelated case[7]. The spectra for correlated and uncorrelated cases are shown in Figure 4.13 along with the measured data from case iii). It can be seen that the curve for measured data closely matches that of the curve of the uncorrelated case. It has been previously assumed in the literature that interference noise from separate channels would be uncorrelated if channel transmitters were separated by a distance much greater than the coherence length of the source [5]. The results presented here confirm this assumption.

---

[7] Correlation, as used here, refers to the correlation between the interference noise generated by channel #1 (which is uncorrelated from the reference) and the interference noise generated by channel #2 (which is also uncorrelated from the reference).
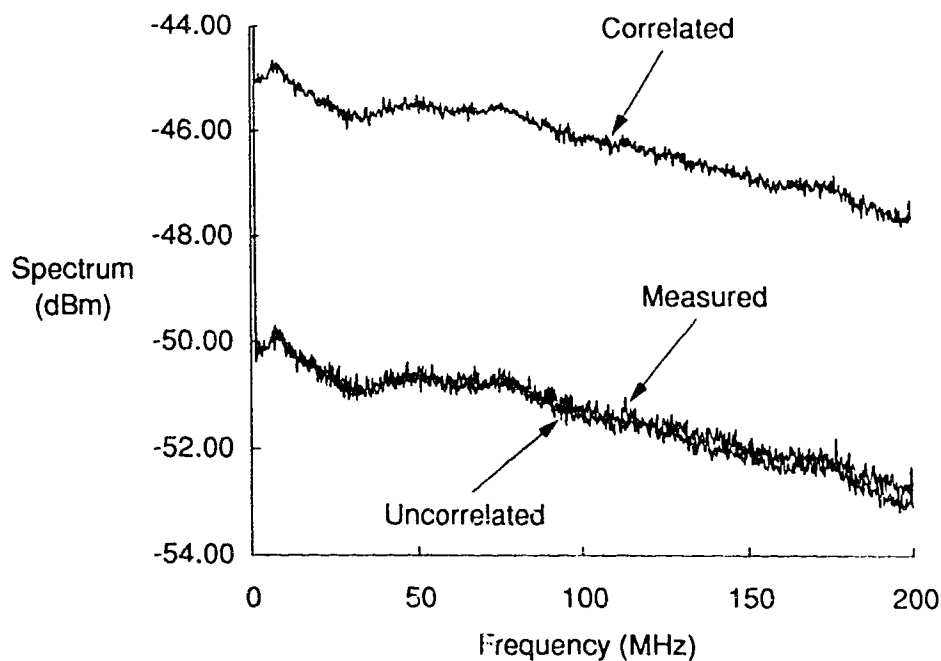
Figure 4.13 Measured power spectrum for channels 1 and 2 simultaneously transmitting. Also shown are theoretically calculated power spectra for the two cases, i) channel 1 uncorrelated with channel 2, and ii) channel 1 correlated with channel 2.

4.5 Absolute Power Measurements

Absolute power measurements were taken to determine the degree of loss that might occur in the system due to optical state of polarization (SOP) mismatch between the reference field and the channel field (in this case, channel #2).

A circuit diagram of the bias circuit constructed for the calibrated PIN photodiode is shown in Figure 4.14. The circuit schematic and detector head mechanical components were supplied courtesy of Bell Northern Research, Ottawa. R1 is a current sampling resistor selected to provide a voltage to optical power sensitivity of 1mV/10nW. Using a Fluke model 75 high input impedance DVM, this gave a measurable optical power range of 0 - 100 μW with a minimum resolution of 0.01 μW.
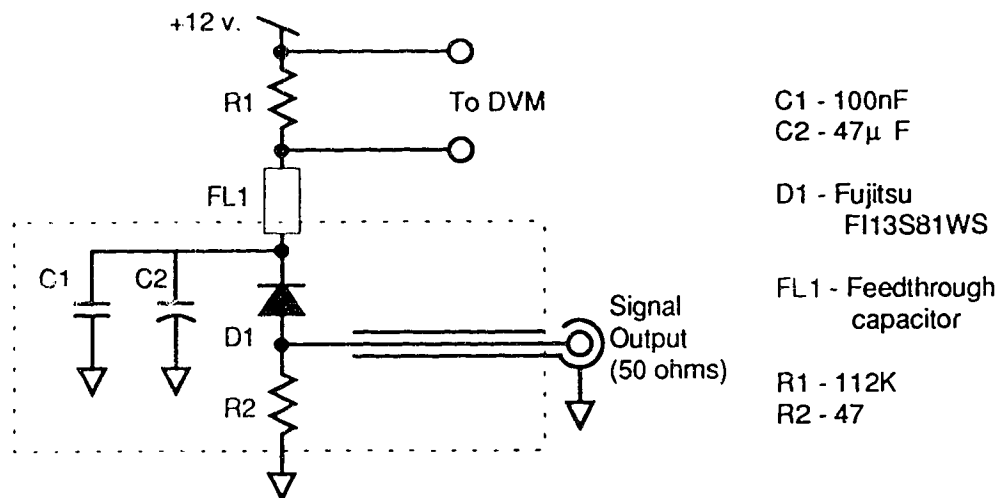
Figure 4.14 Detail of PIN termination circuit.

Channel #2 was decorrelated with the reference using the 10 m delay line. Average optical power incident on the PIN was determined individually for the reference and channel path contributions by measuring the PIN photocurrent. The average optical power for the reference, P_R, was 24.81 μW. The average optical power for channel #2, P_2, was 1.58 μW. With channel #2 enabled, the state of polarization match between the channel and reference was maximized by observing the beat noise on an oscilloscope and adjusting the polarization controller to maximize the noise amplitude. The beatspectrum was then recorded and a theoretical curve fit was performed. The curve fit yielded a measured linewidth of 265 MHz and a spectral amplitude peak of -110.38 dBm/Hz. The theoretical spectral peak for the same linewidth and average optical powers, P_R and P_2, would be -105.8 dBm/Hz. This difference between these two values corresponds to an SOP mismatch loss of 0.35 or 4.6 dB. Through the course of measurements, this was found to be a typical value in this system and indicates that there is room for improvement in the polarization matching technique that was used. Much research is presently taking place in the area of SOP matching for coherent systems [29] and it is anticipated that the SOP matching problem will be eventually be solved.

4.6 Carrier to Noise Ratio

The previous stages in this experiment served to develop confidence in the theoretical model developed in section 3.3. Measured power spectra for the two-channel experimental system agreed reasonably well with theoretical spectral shapes and amplitudes. In addition, it has been shown that grossly mismatched channels are truly uncorrelated with each other. The results presented in this section will attempt to predict CNR_1 and CNR performance for a hypothetical multi-channel CM system using the model developed in sections 3.3 through 3.6. Since CNR_1 is usually the dominant factor in a CM system it will first be analyzed independently. Transmitter and receiver noise will then be included to determine their overall effects on the system. We assume at all times that polarization states of all channel fields are perfectly matched to that of the reference field at the receiver.

The work of Healey [4] has suggested that the capacity of a CM system would be seriously affected by the large number of interference cross-products present in the system and that system SNR would be inversely proportional to the number of channels squared. Preliminary research for this thesis suggested that this constraint could be relaxed substantially by decreasing the channel/reference power ratio (see Section 3.4) in an ERL CM system. Specifically, the noise power could be shifted from a dependency on N^2 to a dependency on N, where N is the number of channels in the system. We therefore begin by examining the effect of changes in this ratio. We recall the definition of the channel/reference power ratio from (3.4.7) where $\Gamma = P_C/P_R$. Using the CNR_1 expression, (3.3.25), the effect of varying Γ on CNR_1 was examined and CNR_1 is shown as a function of Γ in Figure 4.15. L_m for this simulation was arbitrarily chosen as 0.01 m yielding a corresponding δf_{opt} of 3.32 GHz which was used for δf.
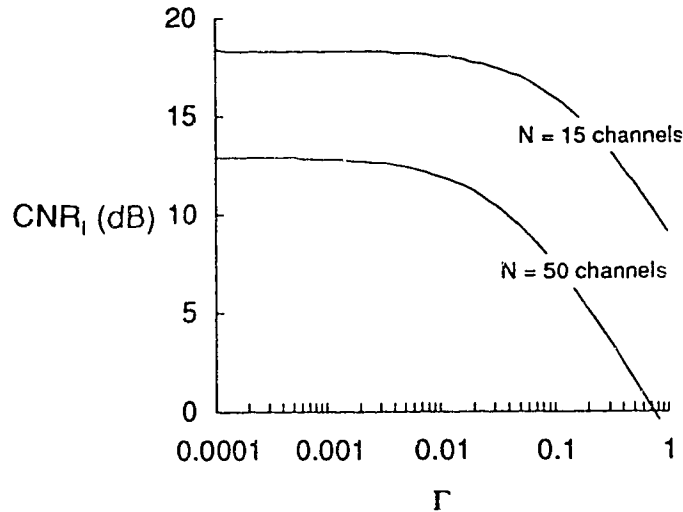
Figure 4.15 Effect of channel/reference power ratio on CNR_I. $L_m = 0.01$ m and $\delta f = \delta f_{opt} = 3.32$ GHz.

As suspected, CNR_I monotonically decreases with an increase in Γ. It can also be noted that CNR_I is more sensitive to changes in Γ for a higher number of channels. Therefore, to maximize the capacity of the CM system in terms of the CNR_I alone, Γ should be made as small as possible. In Figure 4.15 we note that for N=50 channels, we incur a 3 dB CNR_I penalty for $\Gamma = 0.04$.

Using (3.3.25), the effect of varying the A/O carrier frequency, f_s, on the CNR_I was then investigated. A/O devices are presently available with carrier frequencies ranging from 40 MHz to 500 MHz for commercial devices and higher for experimental and military devices. The results are plotted in Figure 4.16 for $L_m = 0.01$ m, $\delta f = 230$ MHz, B = 1 MHz and $\Gamma = 0.01$.
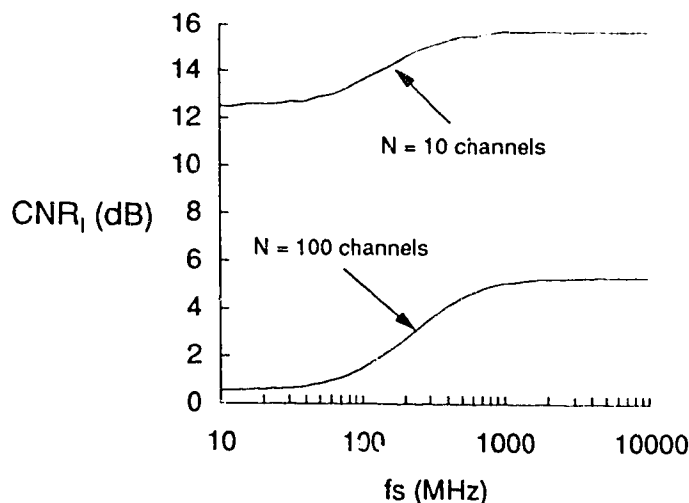
Figure 4.16 Effect of var... center frequency, f_s.

Two general tendencies can be noted from the curves.

i) CNR_1 is higher in the regime, $f_s \gg \delta f$, than it is in the regime, $f_s \ll \delta f$. This is primarily due to the spectral 'folding' that occurs when the width of the noise spectrum is larger than twice the center frequency. In addition, noise contribution from the channel-channel beatspectra (which is centered at baseband) becomes more significant as f_s is decreased.

ii) The difference in CNR_1 for the two regimes mentioned in i) above is more pronounced for 100 channels than it is for 10 channels. This is due, once again, to the noise contribution of the channel-channel beatspectra which increase as the square of N for large N.

Using (3.3.25), the effect of varying the laser linewidth is now examined. Note that in the simulations which follow, $f_s = 40$ MHz, which was used in the experimental system, is assumed. For this simulation, $\Gamma = 0.02$, $B = 1$ MHz and N = 50 simultaneously transmitting channels. The predicted CNR_1 performance as a function of δf is shown for several values of L_m in Figure 4.17. Note that for each value of L_m, there is an optimum value of δf which maximizes the CNR_1. The value of δf_{opt} from the graph is consistent

with that predicted by (3.3.32). Any change in the channel bandwidth, B, or the number of channels, N. would cause a corresponding vertical shift in these curves.
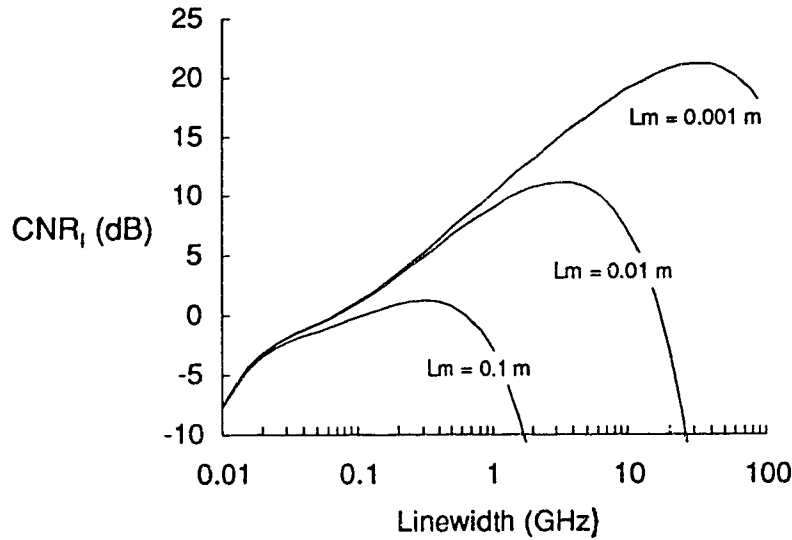
Figure 4.17 Carrier to interference noise ratio as a function of laser linewidth for a 50 channel system with a 1 MHz channel bandwidth. The CNR_I response is shown for three different mismatch lengths.

As previously reported in the literature, we note that below the optimum linewidth, an increase in linewidth causes a corresponding increase in CNR_I. However, above the optimum linewidth, CNR rapidly decreases and it is obvious that the use of a laser linewidth which is larger than the optimum linewidth can seriously degrade the CNR_I of the system. Hence, when considering the effects of interference noise, the mismatch length, L_m, places a fundamental constraint on the maximum multiplexing capacity which is obtainable in the ERL CM system.

We now include the CNR contributions of the transmitter and receiver to determine the overall system CNR. For this analysis the input optical power to the system was held constant and coupler excess loss and fiber attenuation were neglected. Coupler excess loss within the transmitter array is essentially negligible and attenuation in the interconnection fibers between the transmitter array and the receivers could be accounted

for by reducing the system input optical power by an amount equal to the fiber attenuation. Figure D.1 of Appendix D shows an optical power budget diagram of the complete multi-channel ERL CM system. The following equations,

$$P_C = \frac{k^2}{N^2 \alpha} Pin \qquad (D.6)$$

and,

$$\Gamma = \frac{P_C}{P_R} = \frac{k^2}{(1-k)^2 N \alpha} \qquad (D.7)$$

were derived in Appendix D and define P_C and Γ in terms of the system parameters, k, N, and α. The independent variable, k, is the coupling ratio of the head-end directional coupler and the directional couplers at the receivers (Figure D.1). k has an allowable range from 0 to 1 where 1 represents a coupling ratio of 100%. The parameter, α, refers to the insertion loss of the A/O modulators (Figure D.1) and is assumed to be equal for all modulators. N is the number of channels supported by the system.

It is assumed throughout the following analysis that the laser linewidth is equal to the optimum value. The system parameters for the simulation were:

$f_s = 40\ MHz$ $\qquad$ $B = 1\ MHz$

$L_m = 0.01\ m$ $\qquad$ $L_d = 10\ m$ $\qquad$ $\delta f = \delta f_{opt} = 3.3\ GHz$

$Pin = 1\ mW$ $\qquad$ $R_o = 0.89\ A/W$

$RIN = -100\ dB/Hz$

where Pin is the optical power coupled into the head end of the system and R_o is the responsivity of the photodetector in a receiver. Two sets of graphs were produced. The first set is for $\alpha=4$ (6 dB) and consists of graphs of Γ, CNR_I, CNR_{Rx} and CNR_{Tx}, all as a

function of k. The second set consists of the same set of graphs with the exception that α is increased by a factor of 10 to α=40 (16 dB). Figures 4.18 through 4.22 correspond to α=4 while Figures 4.23 through 4.27 correspond to α=40.

Figure 4.18 shows a plot of the channel/reference power ratio, Γ, as a function of the coupling ratio, k.
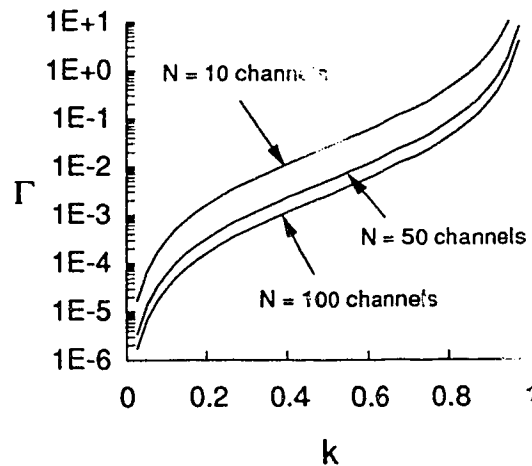
Figure 4.18 Channel/reference power ratio, Γ, as a function of coupling ratio, k, for an A/O loss, α, of 4 (6 dB).

We see that Γ varies non-linearly, increasing monotonically, with k. Note that Γ is shown on a logarithmic scale while k is shown on a linear scale. In Figure 4.19, we see a similar behavior to that shown in Figure 4.15 with CNR_I decreasing monotonically with increasing k.
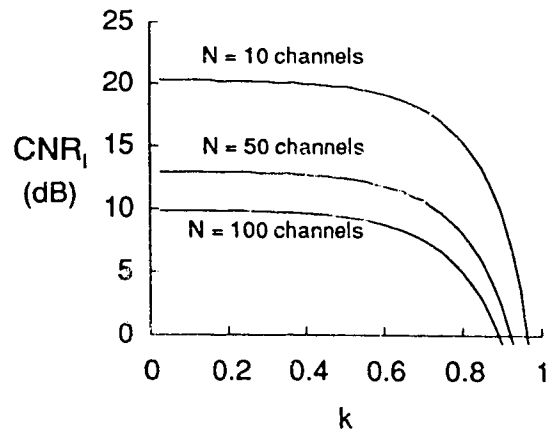
Figure 4.19 CNR$_I$ as a function of coupling ratio, k, for α=4 (6 dB).

Figure 4.20 shows the carrier to noise ratio of the receiver as a function of k.
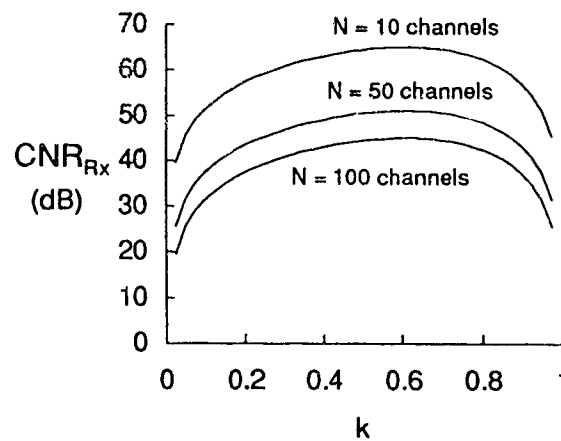
Figure 4.20 CNR$_{Rx}$ as a function of coupling ratio, k, for α=4 (6 dB).

Here we see the CNR$_{Rx}$ reaching a maximum value for an optimum value of k. Substitution of (D.6) and (D.7) into (3.5.7) reveals that the optimum value of k is only dependent upon the A/O insertion loss, α. Figure 4.21 shows the effect of varying k on the transmitter CNR.
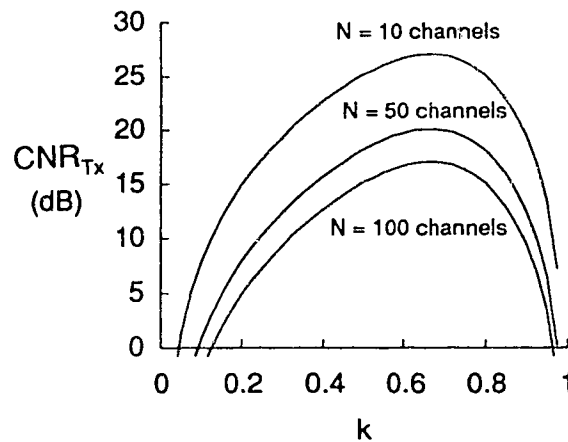
Figure 4.21 CNR_{Tx} as a function of coupling ratio, k, for $\alpha=4$ (6 dB).

As with the receiver CNR, we see the transmitter CNR reaching a maximum value for an optimum value of k. Once again, substitution of (D.7) into (3.4.8) reveals that the optimum value of k is only dependent upon α. Figure 4.22 shows the composite system CNR response as a function of k.
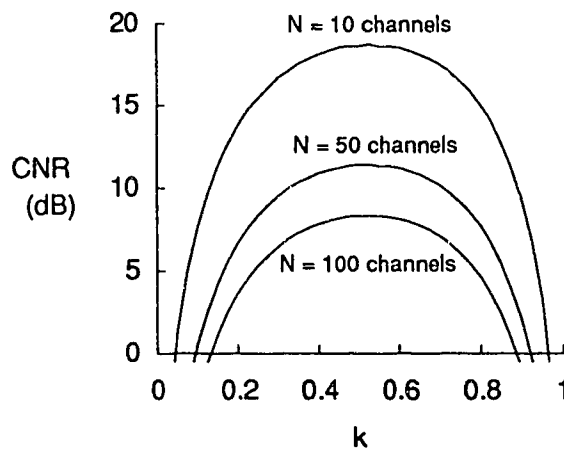
Figure 4.22 System CNR as a function of coupling ratio, k, for $\alpha=4$ (6 dB).

Here we see a relatively broad maximum in the CNR curves occurring around k = 0.5. Note that the system CNR response is essentially formed by the combination of the interference CNR and the transmitter CNR since the receiver noise is relatively

insignificant in this case. Additional analysis, which is not included in this thesis, showed

that only receiver CNR is dependent upon the level of system input optical power, Pin.

Hence, if we were to either decrease the input power to the system or introduce

attenuation into the interconnection fibers, we would see an overall decrease in the

receiver CNR. If enough attenuation were introduced, the point would be reached where

receiver CNR would have a significant effect on the system and the maximum CNR level

would be decreased.

Figure 4.23 shows Γ as a function of k with α increased tenfold to a value of 40.
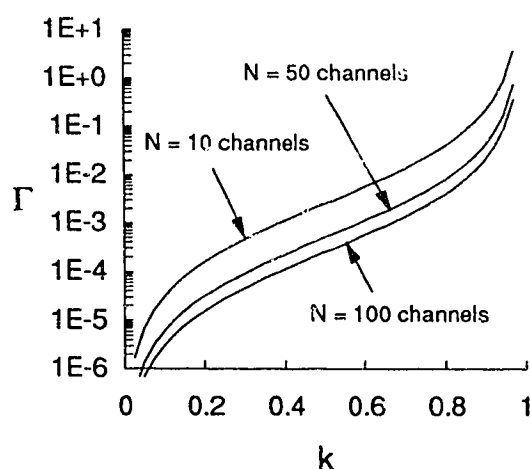
Figure 4.23 Channel/reference power ratio, Γ, as a function of coupling ratio, k, for an A/O loss, α, of 40 (16 dB).

We see a similar behavior to the case where $\alpha=4$ except that the curves have shifted

down. As one would anticipate, this causes the CNR_I curves to "roll off" at a higher value

of k as shown in Figure 4.24.
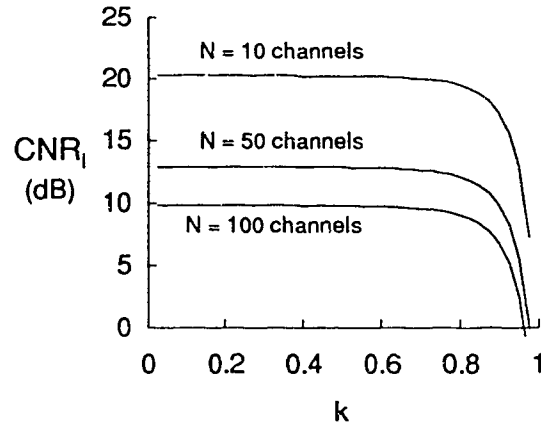
Figure 4.24 CNR_I as a function of coupling ratio, k, for $\alpha=40$ (16 dB).

In Figure 4.25, we observe that the optimum value of k for the CNR_{R_x} curves has increased and that the curves have shifted down by almost 10 dB.
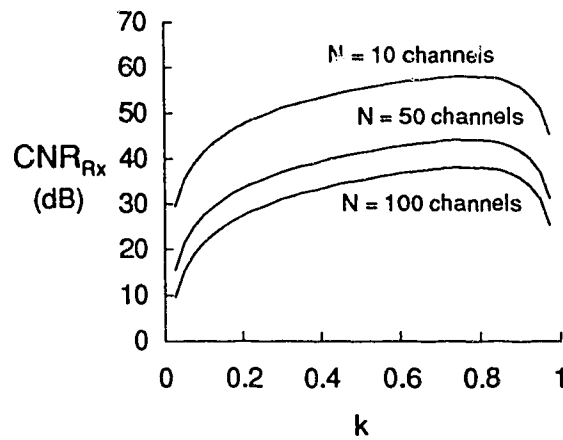
Figure 4.25 CNR_{R_x} as a function of coupling ratio, k, for $\alpha=40$ (16 dB).

In Figure 4.26, we see that the optimum value of k has increased for the transmitter CNR, but there is essentially no vertical shift in the curves.
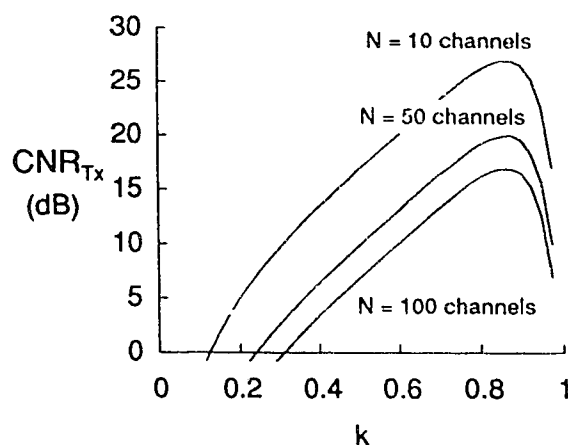
Figure 4.26 CNR_{Tx} as a function of coupling ratio, k, for $\alpha=40$ (16 dB).

In Figure 4.27, the optimum value of k for the system CNR has also increased. It is interesting to note, however, that despite the fact that the A/O insertion loss has been increased tenfold, there has been almost no change in the maximum value of system CNR.
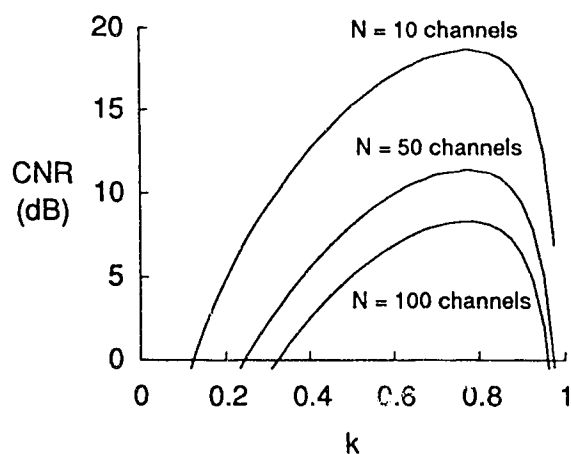
Figure 4.27 System CNR as a function of coupling ratio, k, for $\alpha=40$ (16 dB).

In summary, an analysis of the individual CNR components and overall system CNR has enabled us to not only determine the multiplexing capacity of the ERL CM

system, but to also make informed decisions when selecting certain system parameters. We have seen that differential fiber mismatch places a constraint on the maximum linewidth of the head end laser. If we consider only the effects of interference noise, we see that CNR is maximized by minimizing the channel/reference power ratio. However, when transmitter and receiver noise contributions are included, this is not necessarily the case. We find that for a given level of A/O insertion loss, there is an optimum value of coupling coefficient that should be used to maximize the system CNR. We also find that receiver CNR is the only component that is dependent upon the level of system input optical power. We can make the generalization that an excessive number of channels will cause interference noise to be dominant, insufficient system input optical power will cause receiver noise to be dominant, and excessive RIN level will cause transmitter noise to be dominant.

In the next section, we determine the multiplexing capacity of a digital OOK system of the type analyzed in Section 3.7. For this analysis it was assumed that noise contributions from the receiver and transmitter were negligible which is a reasonable assumption for a system supporting a large number of channels.

4.7 Capacity of a Digital OOK CM System

The primary physical constraint on the performance of the ERL CM system is the ability to match the length of the reference path accurately to that of the desired signal path. From the digital OOK system analyzed in section 3.7 we obtained the expression

$$N \cdot R = \frac{(66,529)}{L_m} \tag{3.7.8}$$

where we have excluded all noise sources except interference noise. The simulated results for this system are summarized in Table 4.1 where various different mismatch

lengths, L_m, have been assumed. Recall that N·R is the product of the number of transmitter channels and the per-channel bit rate. In addition to L_m and N·R, the optimized linewidth, δf, and the minimum delay tolerable in an unmatched path, L_d, are also shown. L_m represents the maximum differential path length for the desired channel and L_d represents the minimum differential path length for all of the other, unwanted, channels. L_d has been calculated for $L_m/L_c > 7$ to ensure a Lorentzian noise spectrum and a 60 dB suppression of unwanted channel carriers.

Table 4.1 Performance of a digital OOK system for 10^{-9} BER.

L_m	L_d	δf	N·R
1 m	> 14 m	33.2 MHz	66.5 kb/s
10 cm	> 1.4 m	332 MHz	665 kb/s
1 cm	> 14 cm	3.32 GHz	6.65 Mb/s
1 mm	> 1.4 cm	33.2 GHz	66.5 Mb/s
100 μm	> 1.4 mm	332 GHz	665 Mb/s
10 μm	> 140 μm	3.32 THz	6.65 Gb/s

We can see from the table that in order to compete with existing technologies, path mismatch lengths less than 100 μm are required. It is also interesting to note that for a properly designed system, the receiver *optical delay line tuning ratio*[8] must be greater than 14:1 in a two channel system, 28:1 in a three channel system 42:1 for a four channel system, etc. These constraints present a number of practical problems. One possible way of implementing a variable optical delay device would be to switch in various lengths of fiber mechanically. By applying binary weights to the lengths of fiber, 2^N different

---

[8] We define the optical delay line tuning ratio as the ratio of the length required for full mismatch to the length required for full matching to a given channel.

values of length would be possible with N discrete fiber lengths. Another way that the switching function could be implemented is through the use of acousto-optic deflectors. Huang *et al.* [30] have successfully demonstrated a 4 x 4 crossbar switch which uses commercially available A/O deflectors and lenses to perform space switching of optical signals. The optimal solution would be to have an electrically variable optical delay device for the CM receiver. In this way, any desired transmitter channel could be selected and a feedback loop could be employed to maintain a strong signal in the midst of environmental fluctuations.

4.8 Amplitude Modulation Demonstration

To demonstrate the overall operation of the experimental system, a 2 MHz sine wave signal, shown in Figure 4.28, was applied to the A\O driver for modulator #1.
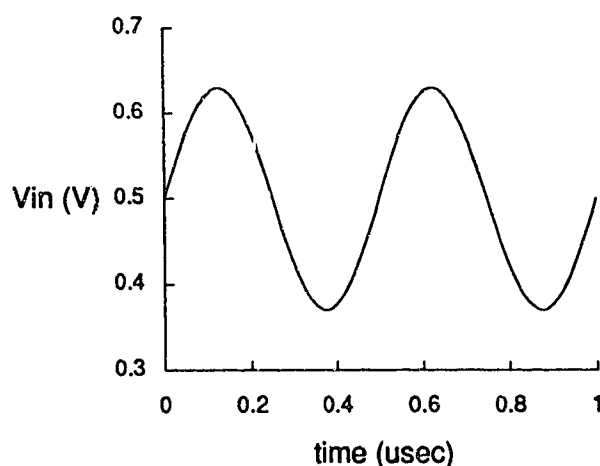
Figure 4.28 2 MHz sine wave signal applied to A/O driver.

Due to the non-linear transfer characteristics of the A/O driver (Figure 4.3) and the A/O modulator (Figure 4.2), the corresponding diffraction efficiency (Figure 4.29) is slightly distorted.

0.4

0.3

Diffraction
Efficiency

0.2

0.1

0   0.2   0.4   0.6   0.8   1

time (usec)
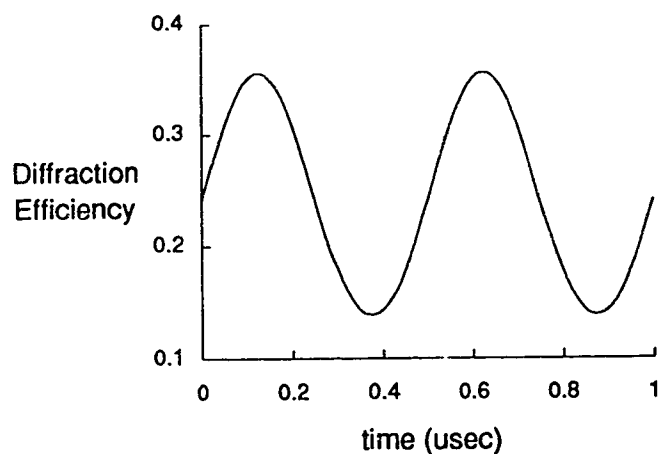
Figure 4.29 Normalized diffraction efficiency of A/O modulator #1 for modulating signal shown in Figure 4.28.

In addition, we note that the signal current amplitude at the receiver output will be proportional to the electric field amplitude of the light at the output of the A/O modulator (see Section 3.7). As a result, the received signal amplitude will be proportional to the root of the diffraction efficiency. We therefore show a plot of the A/O modulator transmissivity which corresponds to the modulating signal in Figure 4.28.

0.7

0.6

Transmis
sivity   0.5

0.4

0.3

0   0.2   0.4   0.6   0.8   1

t (usec)
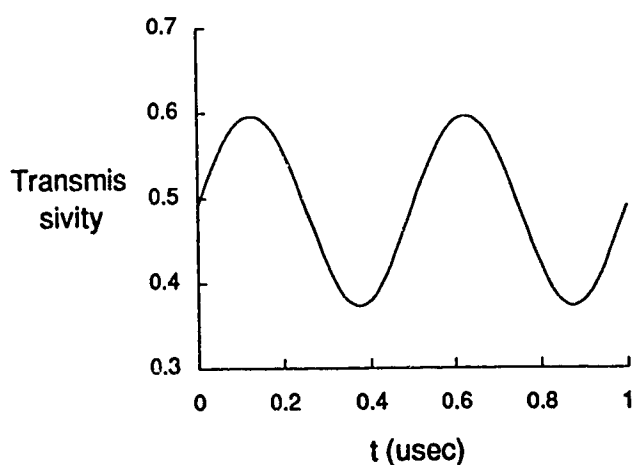
Figure 4.30 Normalized transmissivity of A/O modulator for modulating signal shown in Figure 4.28.

Note that the non-linear transfer characteristic between received and transmitted signals is not necessarily objectionable in a digital OOK system. In an analog system, however, it would be necess'ry to use an A/O driver designed to compensate for the non-linear transfer characteristic of the modulator. The power spectrum of the amplified photocurrent at the receiver is shown in Figure 4.31. The carrier can clearly be seen at approximately 40 MHz with the associated sidebands spaced 2 MHz from the carrier. In addition, a component is visible at 2 MHz. This is a baseband component due to the intensity modulation imprinted on the light from the A/O modulator.

Power
(dBm)

-20
-25
-30
-35
-40
-45
-50
-55
-60
-65
-70

0 5 10 15 20 25 30 35 40 45 50

Frequency (MHz)
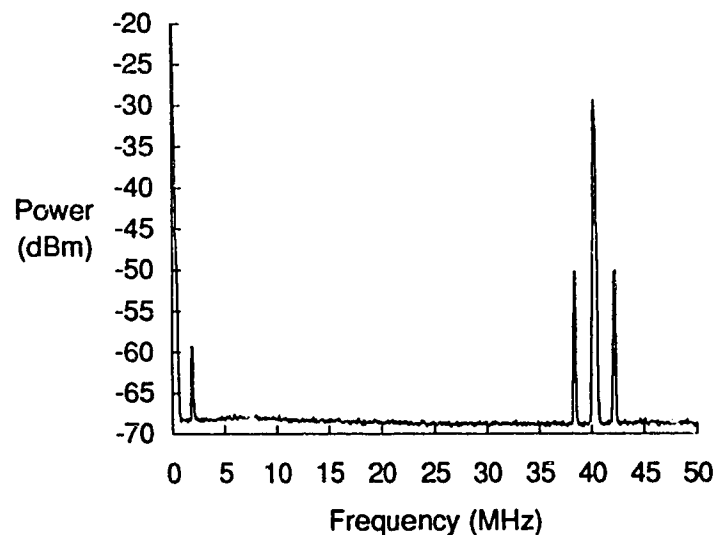
Figure 4.31 Photodetector power spectrum for large carrier, amplitude modulation (AM-DSB-LC) signal shown in Figure 4.28.

If the carrier and sidebands were now mixed down to baseband and low pass filtered, we would recover a signal proportional to that shown in Figure 4.30. The effect of other transmitting channels would be to add interference noise to the receiver output signal.

5. CONCLUSIONS

The purpose of this thesis has been to examine the feasibility of using an ERL CM system architecture in a "Fiber to the Home" broadcast system. To this end, a model has been developed to predict the performance of a multi-channel system of this type. Experimental measurements from a two-channel system have confirmed some portions of the theoretical model and multi-channel simulations have yielded two major results.

First, *varying the channel/reference coupling ratio was found to have a significant impact on system performance.* For given values of certain parameters, system capacity can be maximized by the proper selection of the channel/reference power ratio. Guidelines have been given for the selection of certain system parameters, such as coupling ratios, to maximize system performance. Specifically, for systems with a large number of channels, this power optimization can bring substantial performance gains over non-optimized systems.

Secondly, *differential length mismatch in the two fibers connecting the transmitter array to the receiver was found to have significant impact on system performance.* It has long been suspected that length mismatch might impose the greatest limit to the multiplexing capacity of the ERL CM system [1, 5] but no quantitative results have been previously published. The results of our analysis have shown that, for a given value of mismatch, there is an optimum laser linewidth that should be used to maximize the system CNR performance and that operation at a linewidth at ove this value can substantially degrade system performance. To compete with other fiber telecommunications multiplexing techniques, tight control over fiber path lengths is required and the need exists for a practical path matching scheme. For example, to obtain a total throughput of 6 Gb/s in an OOK ERL CM system, differential length mismatch must be less than 10 μm.

It appears that until the path matching problem is solved, the ERL CM system will not be a viable technology for high speed communications systems. Some possible ways of approaching a solution to the mismatch problem are:

1) Correct choice of application: The ERL CM architecture may be most effectively applied to optical integrated circuit multiplexing. Since the designer of an optical "chip" has a great deal of control over mechanical lengths, the path mismatch length would be much less and greater multiplexing capacity would be possible with relatively simple optical components. Recently, interest has been shown in applying CM multiplexing principles to high speed (> 10 Gbit/s) interprocessor links in parallel computers [31].

2) Multiplex the reference and channel signals on the same fiber by transmitting the reference and channel bus light components in different polarization planes [32]. In this way, one of the fibers could be eliminated. However, unavoidable birefringence in the fiber would aggravate the mismatch problem and the practicality of this technique is questionable.

3) Develop an electrically variable optical delay device for use at the receiver. In this way a feedback loop could be employed at the receiver to compensate for path length mismatches. In addition, such a device could be used for channel selection and tuning.

While a number of performance results for an ERL CM system have been presented in this thesis, the analysis performed here is by no means exhaustive. Several components of this system require development work and it is anticipated that further performance increases are possible. Some of the areas that need further investigation are:

i) Optimal Receiver Design - The analysis of the digital OOK system in this thesis assumed the use of a 1st order LPF noise filter and a simple decision making circuit in the receiver. In addition, predictions of the BER performance were based on the assumption that the composite noise at the receiver's decision slicer behaved according to Gaussian amplitude statistics. It is expected that the estimated performance could be

increased through a more thorough understanding of the actual noise statistics and the inclusion of a matched filter at the receiver. Since the interference noise is a zero mean process, it is anticipated that the use of an "integrate and dump" or correlation receiver in this CM system, for example, would dramatically increase the SNR of the system.

ii) Transmitter Data Statistics - During development of the system model, it was always assumed that all other interfering channels were transmitting a continuous series of NRZ 1's. Since interference noise is only produced when a channel is transmitting a '1' bit, the system BER will actually be lower in a real system than that predicted in this thesis. Further work is therefore needed to determine the improvement in SNR that would be obtained when the statistics of the transmitter input data are considered.

iii) Receiver Channel "Selector" - Throughout the analysis, the assumption has been made that fiber delay lines could be switched in and out of the system at will. Obviously this is not a trivial feat to accomplish and more work is required to develop practical devices to achieve this function. The optimal solution would be to have an electrically variable optical delay device for the CM receiver. In this way, any desired transmitter channel could be selected and a feedback loop could be employed maintain a strong signal in the midst of environmental fluctuations.

iv) Optical Source Characteristics - the system analyzed in this thesis employed a DFB laser as the head end optical source. While the DFB laser is a reasonable choice for a relatively narrowband optical source (~100 MHz linewidth or less), devices exhibiting broad spectrums (> 1 GHz) are typically multi-moded (in the case of laser diodes) or possess non-Lorentzian spectral characteristics (eg. superluminescent diode) [11]. Several researchers have examined crosstalk in certain CM systems where the optical source had an arbitrary spectral shape [11, 32, 3]. Hence, more work is needed to include the effects of an arbitrary optical spectrum in the system performance analysis in this thesis.

REFERENCES

[1]   J.L. Brooks, R.H. Wentworth, R.C. Youngquist, M. Tur, B.Y. Kim and H.L. Shaw, "Coherence multiplexing of fiber-optic interferometric sensors," *IEEE Journal of Lightwave Tech.*, vol. LT-3, no. 5, pp. 1062-1072, Oct. 1985.

[2]   D.W. Smith, P. Healey, G.P. Fry and K. Clayton, "A frequency chirped heterodyne spread spectrum optical fibre multiple access technique," ECOC 1988 Conference Proceedings, Brighton, U.K.

[3]   J.P. Goedgebuer, H. Porte and A. Hamel, "Electrooptic modulation of multilongitudinal mode laser diodes: demonstration at 850 nm with simultaneous data transmission by coherence multiplexing," *IEEE Journal of Quantum Electronics*, vol. QE-23, no. 7, pp. 1135-1144, July 1987.

[4]   P. Healey, "Dimensioning an optical-fiber spread-spectrum multiple-access communication system," *Optics Letters*, vol. 12, no. 6, pp. 425-427, June 1987.

[5]   R.H. Wentworth, "Theoretical noise performance of coherence-multiplexed interferometric sensors," *IEEE Journal of Lightwave Technology*, vol. 7, no. 6, pp. 941-956, June 1989.

[6]   G.D. Cormack and J.R. Waschuk, "Optical fiber broadband access systems, with and emphasis on coherent options," *Alberta Telecommunications Research Centre internal report*, TR-89-03, May 1989.

[7]   S.A. Al-Chalabi, B. Culshaw, and D.E.N. Davies, "Partially coherent sources in interferometric sensors," *Proc. First Int. Conf. on Optical Fibre Sensors* (IEE), Apr. 1983, p. 132.

[8]   Eugene Hecht, "*Optics*," Addison-Wesley, Reading, Mass., 1987.

[9]   R. W. Tkach and A.R. Chraplyvy, "Phase noise and linewidth in an InGaAsP DFB laser," *IEEE Journal of Lightwave Technology*, vol. LT-4, no. 11, pp. 1711-1716, Nov. 1986.

[10] R.J.S. Pedersen, I. Garrett and G. Jacobsen, "Measurement of the statistics of DFB laser frequency fluctuations," *Electronics Letters*, vol. 24, no. 10, pp. 585-586, May 1988.

[11] J.P. Goedgebuer, A. Hamel, H. Porte and N. Butterlin, "Analysis of optical crosstalk in coherence multiplexed systems employing a short coherence laser diode with arbitrary power spectrum," *IEEE Journal of Quantum Electronics*, vol. 26, no. 7, pp. 1217-1226, July 1990.

[12] A. Yariv, "*Optical Electronics*," Holt, Rinehart and Winston, New York, 1985.

[13] W.A. Gardner, "*Introduction to Random Processes*," MacMillan, New York, 1986.

[14] K. Kikuchi and T. Okoshi, "High resolution measurement of the spectrum of semiconductor lasers," *Japan Annual Review on Electronics, Comp., Telecomm., Opt. Devices and Fibres*, 1982, Ohmsha Ltd., Tokyo, Japan and North Holland Publishing Co., Amsterdam, Netherlands, pp. 51-59, 1982.

[15] Charles H. Henry, "Theory of the linewidth of semiconductor lasers," *IEEE Journal of Quantum Electronics*, vol. QE-18, no. 2, pp. 259-264, Feb. 1982.

[16] B. Daino, P. Spano, M. Tamburrini and S. Piazzolla, "Phase noise and spectral line shape in semiconductor lasers," *IEEE Journal of Quantum Electronics*, vol. QE-19, no. 3, pp. 266-270, March 1983.

[17] J.W. Goodman, "*Statistical Optics*," John Wiley, 1985.

[18] J.O. Binder, "Characteristics of semiconductor lasers with optical feedback," Ph.D. thesis, *University of Alberta*, 1989.

[19] K. Petermann, "*Laser Diode Modulation and Noise*," Kluwer Academic Publishers, 1988.

[20] H.B. Kim, R. Maciejko and J. Conradi, "Effect of laser noise on analogue fibre optic systems," *Electronics Letters*, vol. 16, p. 919-920, Nov. 1980.

[21] B.P. Lathi, "*Modern Digital and Analog Communication Systems*," Holt, Rinehart and Winston, New York, 1983.

[22] L.W. Couch, "*Digital and Analog Communications Systems*," MacMillan, New York, 1987.

[23] N. Schunk and K. Petermann, "Numerical analysis of the feedback regimes for a single-mode semiconductor laser with external feedback," *IEEE Journal of Quantum Electronics*, vol. QE-24, July 1988.

[24] Newport Corp., *Newport Product Catalog*.

[25] B.G. Koehler and J.E. Bowers, "In-line single-mode fiber polarization controllers at 1.55, 1.30, and 0.63 μm," *Applied Optics*, vol. 24, no. 3, pp. 349-353, February 1985.

[26] R.A. Morris, "Automatic gain control for semiconductor laser amplifiers," M.Sc. thesis, *University of Alberta*, 1990.

[27] G.D. Cormack, Personal correspondence, Sept. 1990.

[28] L.E. Richter, H.I. Mandelberg, M.S. Kruger, and P.A. McGrath, "Linewidth determination from self-heterodyne measurements with subcoherence delay times," *IEEE Journal of Quantum Electronics*, vol. QE-22, no. 11, pp. 2070-2074, Nov. 1986.

[29] N.G. Walker and G.R. Walker, "Polarization control for coherent communications," *Journal of Lightwave Technology*, vol. 8, no. 3, pp. 438-458, March 1990.

[30] P.C. Huang, W.E. Stephens, T.C. Banwell and L.A. Reith, "Performance of 4 x 4 optical crossbar switch utilising acousto-optic deflector," *Electronics Letters*, vol. 25, no. 4, pp. 252-253, Feb. 1989.

[31] K.W. Chu and F.M. Dickey, "Optical coherence multiplexing for interprocessor communications," *Optical Engineering*, vol. 30, no. 3, pp. 337-344, March 1991.

[32] J.P. Goedgebuer and A. Hamel, "Coherence multiplexing using a parallel array of electrooptic modulators and multimode semiconductor lasers," *IEEE Journal of Quantum Electronics*, vol. QE-23, no. 12, pp. 2224-2237, Dec. 1987.

[33] W.R. Klein and B.D. Cook, "Unified approach to ultrasonic light diffraction," *IEEE Transactions on Sonics and Ultrasonics*, vol. SU-14, no. 3, pp. 123-134, July 1967.

[34] E.H. Young, Jr. and S.K. Yao, "Design considerations for acousto-optic devices," *Proc. IEEE*, vol. 69, p.54, 1981.

[35] D. Maydan, "Acoustooptical pulse modulators," *IEEE Journal of Quantum Electronics*, vol. QE-6, p.15, 1970.

[36] H. Kuwahara, M. Sasaki, and N. Tokoyo, "Efficient coupling from semiconductor lasers into single-mode fibers with tapered hemispherical ends," *Applied Optics*, vol. 19, no. 15, pp. 2578-2583, Aug. 1980.

[37] Wolfgang Bludau and Rolf H. Rossberg, "Low-loss laser-to-fiber coupling with neglibible optical feedback," *IEEE Journal of Lightwave Technology*, vol. LT-3, no. 2, pp. 294-302, April 1985.

APPENDIX A: ACOUSTO-OPTIC MODULATOR

If acoustic waves are used to perturb an optical medium, it is possible to control the frequency, intensity and direction of an optical beam. In this appendix, we develop theoretical expressions which describe the operation of acousto-optic devices which intensity modulate and frequency shift an incident light beam.

A longitudinal sound wave travelling in an optical medium creates a sinusoidal fluctuation in material density. Since refractive index is proportional to the strain in the material, a sinusoidal perturbation in refractive index results and can be represented by

$$\Delta n(z,t) = \Delta n_p \sin(\omega_s t - k_s z). \tag{A.1}$$

where Δn_p is the peak deviation in refractive index and k_s equals the acoustic radian frequency, ω_s, divided by the acoustic phase velocity, v_s [12]. This perturbation can be used to couple a refracted optical beam to an incident beam. Two main geometries can be used, 1) collinear wave configuration (shown in Figure A.1) and 2) Normal or near normal configuration (shown in Figure A.2).
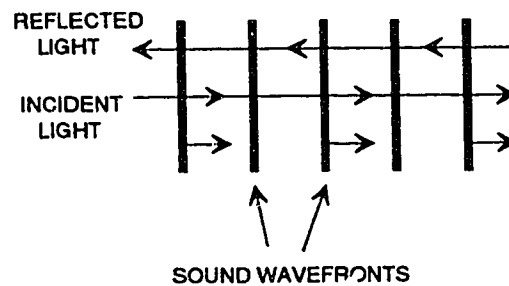
Figure A.1 Collinear wave acousto-optic interaction.
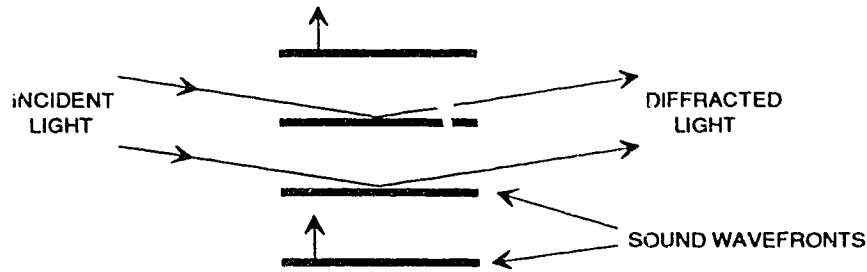
Figure A.2 Near normal acousto-optic configuration.

The collinear configuration is similar to the structure used in distributed feedback lasers (DFB) but is not a practical configuration for a modulation or deflection device. We will therefore only consider the near normal configuration of Figure A.2.

We begin by assuming that our acousto-optic medium is optically isotropic and defining the parameter, Q, where

$$Q = 2\pi \frac{\lambda L}{n\Lambda},$$ (A.2)

λ is the light wavelength, Λ is the sound or acoustic wavelength, n is the refractive index of the medium and L is the width of the acoustic beam. Depending on the value of Q, we will have three different regimes of operation [33]:

Case 1: $Q<<1$ - Raman and Nath regime.

Case 2: $Q\sim1$ - Transition regime.

Case 3: $Q>>1$ - Bragg regime (actual value is $Q > 7$ [33]).

In the Raman and Nath regime (case 1), we analyze the acoustically perturbed medium as a sinusoidal phase grating. Diffracted light will be coupled into multiple orders analogous to the creation of multiple frequency components from phase modulation in FM radio theory. In the transition region, diffraction is a combination of the behavior in cases 1 and 3. In the Bragg regime (case 3), the acoustic perturbation behaves like an amplitude grating. Hence, all diffracted light is coupled into only two orders. Once again

the analogy can be drawn to the production of frequency components resulting from amplitude modulation in AM radio theory. Most practical A/O devices operate in the Bragg regime and all of the following analysis will deal with this regime.

Figure A.3 shows two near-normal geometries that will support Bragg diffraction.
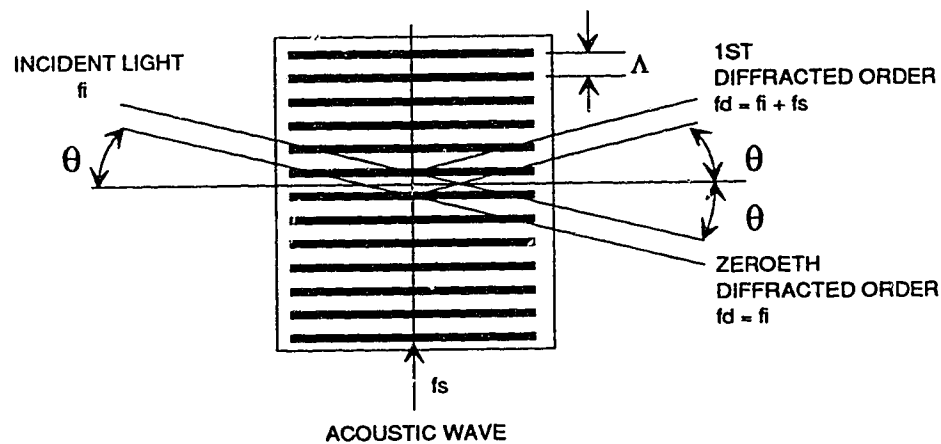
a) Upshifted configuration
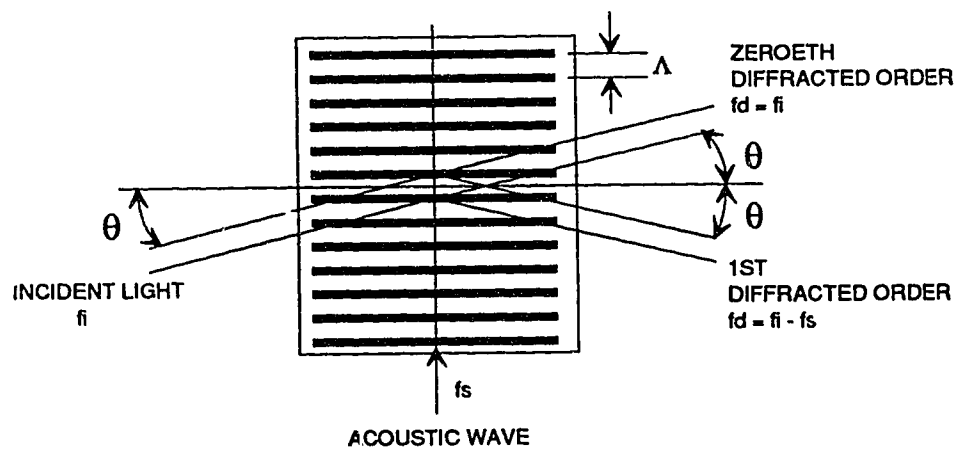
b) Downshifted configuration

Figure A.3 Bragg diffraction geometry showing (a) upshifted configuration and (b) downshifted configuration.

From coupling of modes theory [12], it can be shown that for $\theta = \theta_B$, where θ_B is called the Bragg angle,

$$\sin \theta_B = \frac{\lambda}{2\Lambda n} \tag{A.4}$$

and the frequency of the 1st order diffracted light beam, $'_d$, will be given by

$$f_d = f_i + f_s \tag{A.5}$$

for the *upshifted* configuration where f_i is the frequency of the incident light beam and f_s is the acoustic frequency. For the *downshifted* configuration, the frequency of the 1st order diffracted light beam is given by

$$f_d = f_i - f_s \tag{A.6}$$

Thus an A/O device can be used as a light *frequency shifter*. The frequency of the light in the zeroeth diffracted order will simply equal that of the incident light frequency.

We now denote the intensity of the light in the incident beam by I_i, the intensity of the 1st order diffracted beam by I_1 and the intensity of the 0th order diffracted beam by I_0. It can be shown that the optical power transfer from the incident to 1st order diffracted beam (*diffraction efficiency*) [34] is given by

$$\frac{I_1}{I_i} = \sin^2 (\eta L) \tag{A.7}$$

where $\eta = \pi\Delta n/\lambda$, Δn is the peak deviation in refractive index and $\lambda = \lambda_i \cong \lambda_d$. L is the interaction length of the acoustic beam with the optical beam. The efficiency of throughput from the incident beam to the zeroeth order beam is given by

$$\frac{I_0}{I_i} = \cos^2 (\eta L).$$
(A.8)

η can also be expressed as

$$\eta = \frac{\pi}{\sqrt{2}\lambda} \sqrt{M\, I_a}$$
(A.9)

M is a figure of merit that we define as

$$M = \frac{n^6 p^2}{\rho\, v_s^3}$$
(A.10)

where n is the refractive index of the medium, p is the photoelastic constant, ρ is the mass density, v_s is the speed of sound in the medium and I_a is the acoustic intensity of the sound. Substituting (A.9) into (A.7) we obtain the following expression for the diffraction efficiency

$$\frac{I_1}{I_i} = \sin^2\left[\frac{\pi L}{\lambda} \sqrt{\frac{M}{2}}\ \sqrt{I_a}\right]$$
(A.11)

and the final expression is

$$\frac{I_1}{I_i} = \sin^2\left[\frac{\pi L}{\lambda} \sqrt{\frac{M}{2}}\ \sqrt{\frac{P_a}{A}}\right]$$
(A.12)

where P_a is the acoustic power and A is the cross-sectional area of the acoustic beam [12]. By varying the power of the acoustic signal, we can vary the amplitude of the two diffracted beams. Thus the A/O modulator can be used as a *light intensity modulator*.

The modulation bandwidth of an A/O device is defined as the acoustic modulation frequency at which the effective intensity modulation depth of the 1st order diffracted beam decreases by 3 dB. This frequency is given by

$$f_{3dB} = 0.75 \, v_s \, /D \qquad (A.13)$$

where v_s is the speed of sound in the medium and D is the light beam diameter [34]. Further, it has been shown that the rise time for a Gaussian light beam is given by [35]

$$t_r = 0.64 \, D/v_s \qquad (A.14)$$

APPENDIX B: SUPER2 CURVE FITTING PROGRAM

The Super2 curve fitting program allows measured beatspectrum data from the HP spectrum analyzer to be fit to a function of the form of (3.2.9). The program provides interactive curve fitting in a menu driven, windowed environment.

A Lotus 123[1] spreadsheet called *beat.wkl* is first used to subtract the noise floor from the measured beatspectrum and produce an ASCII data output file consisting of 800 data points (using the *print file* command with *no options* set). The *Super2* program is then executed and the data file is read in with the *Input file* command. At this point, the user is given the option of having the amplitude fitting range automatically selected by the program from the data in the file. System parameters such as delay line length, fit increment and spectrum analyzer frequency increment are then set by the user. The linewidth fitting range is then set by the user and the fit is started with the R (run) command. The program then evaluates the sum of the squares of the errors over the amplitude and linewidth range specified. The linewidth and amplitude for the minimum sum of squares are then stored and the range is reset to frame these values. Consecutive runs can be performed until a local or global sum of squares minimum is obtained. When the user is satisfied with the fit, the fitted curve can be written to an output file using the *Output File* command. This file can then be loaded into the beat.wk1 spreadsheet and the measured data and fitted curve plotted together on the same graph. Note that the Super2 output file will also contain the amplitude and linewidth parameters for the fit.

The following is a program listing of the Super2 program. The program was written and compiled using the Borland Turbo C 2.0 environment.

---

[1] Lotus 123 is a trademark of Lotus Development Corporation.

```
/*                                                   */
/*          SUPER2.C (DSH_FIT7.C)    ver. 1.1        */
/*                                                   */
/*          Darren Blair   Nov 29, 1990             */
/*                                                   */
/*          This program performs a least squares    */
/*          curve fit of the DSH setup using Kikuchi  */
/*          and Okoshi's theory. The residuals are   */
/*          calculated on a LOG scale.               */

/*          WINDOWed version                          */

#include <stdio.h>
#include <dos.h>
#include <conio.h>
#include <math.h>

#define    NO_OF_POINTS    ((unsigned int)(800))
#define fo                  ((double)(40000000))        /* 40 MHz A/O Freq. */
#define PI                  ((double)(3.141592654))
#define RBW                 ((double)(300000))
#define TRUE        1
#define FALSE       0

#define    ULcorner 201
#define URcorner 187
#define    LLcorner 200
#define    LRcorner 188
#define    Hbar     205
#define    Vbar     186

#define STAND1      44,4,35,5
#define STAND2      44,8,35,5
#define STAND3      44,13,35,5

char buf[25*80*2];

char          *input_file[16];        /* Name of spectrum analyzer file */
char          *output_file[16];
double        dB_data [810];
double        lin_data [810];
double        dB_curve [810];
double        lin_curve [810];
double        fint;
double        delta_f_start, delta_f_inc, delta_f_stop;
double        ampl_start, ampl_inc, ampl_stop;
double        ampl_min, delta_f_min, SOS_min, r2;
unsigned int  fit_step;
double        length;           /* delay line length */
int           last_x, last_v, last_width, last_height;

main()        /* MAIN program */
{
```

```c
        init_params();
        menu();
}

init_params()
{
        FILE    *fp;

        strcpy(input_file, "----------");    /* NONE indicates no file loaded */
        strcpy(output_file, "----------");   /*                    */

        if((fp = fopen("superfit.ini", "r")) != NULL)
        {
                fscanf(fp, " %lg", &delta_f_start);
                fscanf(fp, " %lg", &delta_f_inc);
                fscanf(fp, " %lg", &delta_f_stop);
                fscanf(fp, " %lg", &ampl_start);
                fscanf(fp, " %lg", &ampl_inc).
                fscanf(fp, " %lg", &ampl_stop);
                fscanf(fp, " %d", &fit_step);
                fscanf(fp, " %lg", &length);
                fscanf(fp, " %lg", &fint);        /* spectrum analyzer freq. inc. */
        }
        else
        {
                delta_f_start = 200e6;
                delta_f_inc = 10e6;
                delta_f_stop = 250e6;

                ampl_start = -52;
                ampl_inc = 1;
                ampl_stop = -50;

        fit_step = 2;
                length = 1000;
                fint = 1.25e6;
        }

        SOS_min = 1e20;
        ampl_min = 0;
        delta_f_min = 0;

        fclose(fp);
}

save_params()
{
        FILE    *fp;

        fp = fopen("superfit.ini", "w");

        fprintf(fp, "%lg\n", delta_f_start);
        fprintf(fp, "%lg\n", delta_f_inc);
        fprintf(fp, "%lg\n", delta_f_stop);
```

```
            fprintf(fp, "%lg\n", ampl_start);
            fprintf(fp, "%lg\n", ampl_inc);
            fprintf(fp, "%lg\n", ampl_stop);
            fprintf(fp, "%d\n", fit_step);
            fprintf(fp, "%lg\n", length);
            fprintf(fp, "%lg\n", fint);

            fclose(fp);
}

menu()
{
            char choice;

            int start;

            start = TRUE;

            while(1)
            {
            clrscr();

            textcolor(YELLOW);
            cprintf("\n\r\n\r   (I)nput File : %s\r\n\r\n", input_file);

            cprintf("   (A) DELTA F  Start (MHz)   : %lg\n\r", delta_f_start/1e6);
            cprintf("   (B)         Stop (MHz)   : %lg\n\r", delta_f_stop/1e6);
            cprintf("   (C)         Increment (MHz): %lg\n\r\n\r", delta_f_inc/1e6);

            cprintf("   (D) AMPLITUDE Start (dB)    : %lg\n\r", ampl_start);
            cprintf("   (E)         Stop  (dB)    : %lg\n\r", ampl_stop);
            cprintf("   (F)         Increment (dB) : %lg\n\r", ampl_inc);

            cputs("\n\r        MINIMIZED PARAMETERS:\n\r");
            cprintf("            Delta f     = %lg (MHz)\n\r", delta_f_min/1e6);
            cprintf("            Amplitude   = %lg (dB)\n\r", ampl_min);
            cprintf("            SOS         = %lg \n\r", SOS_min);
            cprintf("            R squared   = %lg \n\r", r2);

            cprintf("\n\r   (R)un Curve Fit       (G) Fit Increment = %d", fit_step);
            cprintf("\n\r   (O)utput Curve        (L) Delay line length = %lg", length);
            cprintf("\n\r\n\r   (Q)UIT                (H) Auto Range   (S) Freq Increment = %lg (MHz)", fint/1e6);

            textcolor(CYAN);
            draw_border(80,24);
            textcolor(RED);
            gotoxy(35,1); cputs(" MAIN MENU ");
            textcolor(WHITE);

            if(start == TRUE)
            {
                    sign_on_banner();
                    start = FALSE;
            }
```

```
choice = getch();
switch(choice)                    /* Parse menu option */
{
        case 'I':
        case 'i':
                open_window(1,1,78,23);
                read_data();
                close_window();
                break;

        case 'O':
        case 'o':
                open_window(3,5,40,15);
                write_curve();
                close_window();
                break;

        case 'A':
        case 'a':
                open_window(STAND1);
                cputs("Delta f Start? (MHz) ");
                scanf("%lg", &delta_f_start);
                delta_f_start *= 1e6;
                close_window();
                break;

        case 'B':
        case 'b':
                open_window(STAND1);
                cputs("Delta f Stop? (MHz) ");
                scanf("%lg", &delta_f_stop);
                delta_f_stop *= 1e6;
                close_window();
                break;

        case 'C':
        case 'c':
                open_window(STAND1);
                cputs("Delta f Increment? (MHz) ");
                scanf("%lg", &delta_f_inc);
                delta_f_inc *= 1e6;
                close_window();
                break;

        case 'D':
        case 'd':
                open_window(STAND2);
                cputs("Amplitude Start? (dB) ");
                scanf("%lg", &ampl_start);
                close_window();
                break;

        case 'E':
```

```
case 'e':
        open_window(STAND2);
        cputs("Amplitude Stop? (dB) ");
        scanf("%lg", &ampl_stop);
        close_window();
        break;

case 'F':
case 'f':
        open_window(STAND2);
        cputs("Amplitude Increment? (dB) ");
        scanf("%lg", &ampl_inc);
        close_window();
        break;

case 'G':
case 'g':
        open_window(STAND3);
        cputs("Curve Fit Step Increment? ");
        scanf("%d", &fit_step);
        close_window();
        break;

case 'H':
case 'h':
        autorange();
        break;

case 'R':
case 'r':
        open_window(15,1,60,24);
        curve_fit();
        close_window();
        break;

case 'S':
case 's':
        open_window(STAND3);
        cprintf("Present value is %lg (MHz)\n\r", fint/1e6);
        cputs("New Spectrum analyzer frequency increment? (MHz) ");
        scanf("%lg", &fint);
        fint *= 1e6;
        close_window();
        break;

case 'L':
case 'l':
        open_window(STAND3);
        cputs("Delay Line Length? ");
        scanf("%lg", &length);
        close_window();
        break;

case 'Q':
```

```
                    case 'q':
                            open_window(STAND3);
                            cputs("Save Parameters? (Y/N)\r\n\r\n (ESC) to Return to Menu");
                            gotoxy(23,1);
                            choice = getche();
                            close_window();

                            if ((choice == 'Y') || (choice == 'y')) save_params();
                            if (choice == 27)
                            {
                                    break;
                            }
                            clrscr();
                            textcolor(CYAN | BLINK);
                            cputs("\n\r\n\r    BYE, BYE !!! ... thanks for using SUPERFIT\n\r\n\r");
                            textcolor(WHITE);
                            exit(0);

                    default :
                            open_window(2,18,40,5);
                            cputs("   Unrecognized Command ");
                            wait();
                            close_window();
            }
    }
}

sign_on_banner()
{
            open_window(20,10,40,5);
            textcolor(CYAN);
            cputs("\n\r SUPERFIT-2 v1.2   by Darren Blair ");
            textcolor(WHITE);
            getch();
            close_window();
}

double lin_to_dB(lin)       /* Linear to dB conversion */
double lin;
{
            return(10*log10(lin));
}

double dB_to_lin(dB)        /* dB to Linear conversion */
double dB;
{
            return(pow(10, dB/10));
}

double calc_fn (f, delta_f, lin_ampl, Td)  /* Evaluate the fitting function */
double f, delta_f, lin_ampl, Td;
{
            double a, b, c, d, arg_1, arg_2, PSD;
```

```
a = (1/(delta_f*PI)) / (1 + (f - fo)*(f - fo) / (delta_f*delta_f));
            arg_1 = 2*PI*delta_f*Td;
            arg_2 = 2*PI*(f-fo)*Td;
b = exp(-arg_1);

if (f == fo)
{
            c = 1 + arg_1;
            d = b;
}
else
{
            c = cos(arg_2) + (delta_f * sin(arg_2) / (f-fo));
            d = 0;
}
PSD = lin_ampl*(RBW*a*(1-(b*c)) + d)*delta_f*PI / RBW;
return (PSD);
}


/*
curve_fit()
Least squares curve fitting algorithm. Using a brute force approach,
the SOS (with residuals normalized to the data) is evaluated over a
specified range of parameter space. The best set of parameters are
those that yield the minimum SOS.
*/
curve_fit()
{
            double f, delta_f, lin_ampl, ampl, PSD, error, SOS, Td;
            double mean, sum_of_dev, sum_of_res;
            unsigned int       n;

            if (strcmp(input_file, "**********") == 0)
            {
                    cputs("You must first specify an input Data file!\n\r");
                    wait();
                    return;
            }

            SOS_min = 1e20;
            Td = (1.44 * length) / 300000000;     /* delay time of delay line */
            for (delta_f = delta_f_start; delta_f <= delta_f_stop;
                                            delta_f += delta_f_inc)
            {
                    for(ampl = ampl_start; ampl <= ampl_stop;
                                            ampl += ampl_inc)
                    {
                            lin_ampl = dB_to_lin(ampl);

                            SOS = 0;
                            for (n=1; n<=NO_OF_POINTS; n+=fit_step)
                            {
                                    f = fint * n;
                                    lin_curve[n] = calc_fn(f, delta_f, lin_ampl, Td)
```

```
                                        + calc_fn(-(f), delta_f, lin_ampl, Td);
                    error = (lin_curve[n] - lin_data[n])/lin_data[n];
                    SOS += error*error;
                    if (kbhit() == 1) return;
            }
            if (SOS < SOS_min)
            {
                        SOS_min = SOS;
                        delta_f_min = delta_f;
                        ampl_min = ampl;
            }
        cprintf("Delta f: %lg  Ampl: %lg  SOS: %lg\n\r",
                                    delta_f/1e6, ampl, SOS);

        }
}


gen_curve();    /* Generate theoretical curve to evaluate R2 */
mean = 0;                     /* Calculate mean of data */
for(n=1; n<=NO_OF_POINTS; n++)
{
        mean += lin_data[n];
}
mean /= NO_OF_POINTS;

sum_of_dev = 0;
sum_of_res = 0;
for(n=1; n<=NO_OF_POINTS; n++)
{
        sum_of_dev += ((lin_data[n] - mean)*(lin_data[n] - mean));
        sum_of_res += ((lin_data[n] - lin_curve[n])*(lin_data[n] - lin_curve[n]));
}


r2 = 1 - (sum_of_res / sum_of_dev);

cprintf("\n\n\rDelta f Min   = %lg\n\r", delta_f_min/1e6);
cprintf("Amplitude Min = %lg\n\r", ampl_min);
cprintf("SOS Min       = %lg\n\r", SOS_min);
cprintf("R squared     = %lg\n\r", r2);
autorange();
wait();

}

gen_curve()
{
        unsigned int n;
        double lin_ampl_min, f, Td;

        lin_ampl_min = dB_to_lin(ampl_min);

        Td = 1.44 * length / 300000000;
        for (n=1; n<=NO_OF_POINTS; n++)
        {
```

```
                                    f = fint * n;
                                    lin_curve[n] = calc_fn(f, delta_f_min, lin_ampl_min, Td)
                                            + calc_fn(-(f), delta_f_min, lin_ampl_min, Td);

                    }
}

read_data()          /* Read data from spectrum analyzer file */
{
            FILE        *fp;
            unsigned int n;
            char choice;

            cputs("\nSpectrum Analyzer file? ");
            scanf("%s", input_file);
            cputs("\n\r");

            if((fp = fopen(input_file, "r")) == NULL)
            {
                    cprintf("\nCannot find file: %s\n\n", input_file);
                    strcpy(input_file, "**********");
                    wait();
                    return;
            }

            cputs("Reading file...");
            for (n = 1; n <= NO_OF_POINTS; n++)
            {
                    fscanf(fp, " %lg", &dB_data[n]);
                    lin_data[n] = dB_to_lin(dB_data[n]);

                    cputs(".");
            }

            cputs("\r\n\r\nAutomatic amplitude range from file? (Y/N)");
            choice = getche();
            if ((choice == 'Y') || (choice == 'y')) autorange_init();

            fclose(fp);
}


/*          Function Autorange_init()
            Automatically sets up the initial amplitude range based on data
            values read in from spectrum analyzer file  */

autorange_init()
{

            ampl_start = dB_data[10] - ampl_inc - 3;
            ampl_stop = dB_data[10] + ampl_inc - 3;
}

autorange()
{
            if (delta_f_start != delta_f_stop)
```

```
                {
                            delta_f_start = delta_f_min - delta_f_inc;
                            delta_f_stop = delta_f_min + delta_f_inc;
                }

                if (ampl_start != ampl_stop)
                {
                            ampl_start = ampl_min - ampl_inc;
                            ampl_stop = ampl_min + ampl_inc;
                }
}

write_curve()           /* Write fitted curve to file */
{
            FILE        *fp;
            unsigned int n;

            if (strcmp(input_file, "**********") == 0)
            {
                        cputs("You must first specify an input Data file!\n\r");
                        wait();
                        return;
            }

            cputs("\nFitted Curve File? ");
            scanf("%s", output_file);
               uts("\n\r\n\rGenerating Curve.....");
            gen_curve();

            fp = fopen(output_file, "w");

            cprintf("\n\r\n\rWriting to %s....", output_file);

            fprintf(fp, "Delta_f = %lg (Hz)\n", delta_f_min);
            fprintf(fp, "Amplitude Offset = %lg (dB)\n", ampl_min);
            fprintf(fp, "R squared = %lo\n", r2);

            for (n=1; n<=NO_OF_POINTS; n++)
            {
                        dB_curve[n] = lin_to_dB(lin_curve[n]);
                        fprintf(fp, "%lg\n", dB_curve[n]);
            }
}

wait()
{
            cputs("\n\rHit Any Key to Continue");
            getch();
}

draw_border(width, height)
int width, height;
{
            int         n;
```

```
        gotoxy(1,1);                    cprintf("%c", ULcorner);
        gotoxy(width,1);               cprintf("%c", URcorner);
        gotoxy(1, height);             cprintf("%c", LLcorner);
        gotoxy(width, height);         cprintf("%c", LRcorner);

        for(n=2; n<=(width-1); n++)   /* Horizontal bars */
        {
                gotoxy(n,1);
                cprintf("%c", Hbar);
                gotoxy(n,height);
                cprintf("%c", Hbar);
        }
        for(n=2; n<=(height-1); n++)   /* Vertical Bars */
        {
                gotoxy(1,n);
                cprintf("%c", Vbar);
                gotoxy(width,n);
                cprintf("%c", Vbar);
        }
}


open_window(x, y, width, height)
int     x, y, width, height;
{
        int x1, y1, x2, y2;

        last_x = x;                              /* save info for closing window */
        last_y = y;
        last_width = width;
        last_height = height;

        x1 = x;
        y1 = y;
        x2 = x1 + width - 1;            /* Save existing text */
        y2 = y1 + height - 1;
        gettext(x1, y1, x2, y2, buf);

        window(x1, y1, x2+1, y2);        /* Open window and draw border */
        textcolor(GREEN);
        draw_border(width, height);      /* - notice a slightly larger */
        textcolor(WHITE);                /* right margin is used to avoid */
                                         /* border wraparound */

        window(x1+1, y1+1, x2-1, y2-1);   /* Clear window */
        clrscr();

        window(x1+2, y1+1, x2-2, y2-1);   /* Resize window to leave margin */
        textcolor(WHITE);
}

close_window()
{
        int x1, y1, x2, y2;
```

```
        x1 = last_x;
        y1 = last_y;
        x2 = x1 + last_width - 1;
        y2 = y1 + last_height - 1;
        puttext(x1, y1, x2, y2, buf);
        window(1, 1, 80, 25);
}
```

APPENDIX C: APPARATUS IMPROVEMENTS

As noted in section 4.1, two stages of optical isolation were required to avoid significantly altering the laser's spectral characteristics. Since bulk optical isolators were readily available, the coupling scheme shown in Figure C.1 (a) was used in the experimental system.

Using this technique, high coupling efficiencies could not be obtained for more than a few minutes because the setup was very sensitive to mechanical fluctuations. As a result, the supporting micrometers had to be adjusted regularly to maintain reasonable coupling efficiencies and power levels had to be constantly monitored.

An alternative and better solution would be to use a fiber taper to couple light from the laser into the fiber followed by a pigtailed isolator (Figure C.1 (b)). The work of Kuwahara et al. has shown that single-mode fibers with tapered hemispherical ends can provide laser-fibre coupling efficiencies of more than 35 % [36]. In addition, Bludau and Rossberg have shown that by fusing a specially formed lens to a SM fibre end, coupling efficiencies greater than 40 % can be obtained with power feedback levels on the order of 10^{-7} of the emitted power [37]. Most notably, this technique would greatly simplify the alignment procedure and improve coupling stability.

It is suspected that the dominant external laser feedback in the system was due to the first FC connector at the head end of the system. All optical connectors in the system were standard FC type connectors providing as much as 9 dB of return loss. Feedback within the system could be greatly reduced by replacing these connectors with the recently available FC/APC connectors. These connectors employ a physical contact facet which is angled at 8°, providing a typical return loss of 68 dB (connected or unterminated).
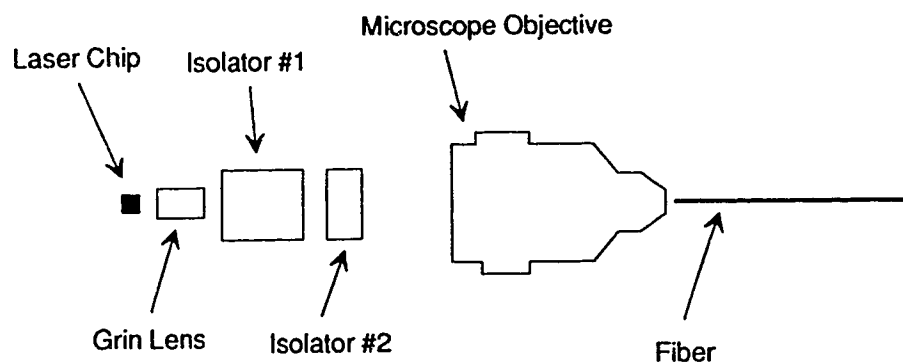
(a) Existing laser-fibre coupling scheme employing bulk isolators
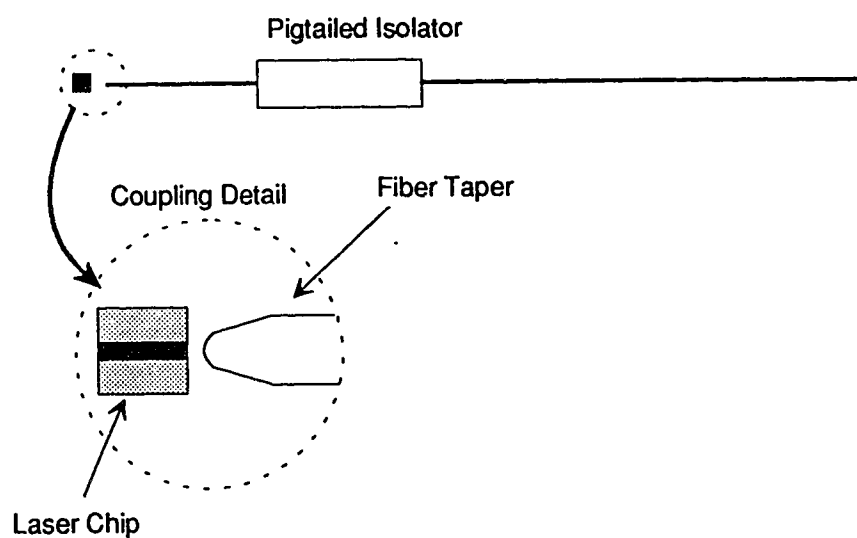
(b) Proposed improved technique employing fiber taper and
pigtailed isolator.

Figure C.1 Coupling technique used in the experiment (a), and proposed coupling
technique (b).

APPENDIX D: THEORETICAL POWER BUDGET

In this appendix, expressions are developed which relate the receiver channel power, P_C, receiver reference power, P_R, and the channel/reference power ratio, Γ, to the system input optical power. The equations that are derived allow for coupler splitting losses and A/O insertion loss throughout the system. Coupler excess loss and fiber attenuation are neglected. However, excess loss and fiber attenuation within the transmitter array is essentially negligible and attenuation in the interconnection fibers between the transmitter array and the receivers can be accounted for by reducing the system input optical power by an amount equal to the fiber attenuation.

Figure D.1 shows an optical power budget diagram of the ERL CM system architecture introduced in Section 3.3. Note that fiber delay lines have been omitted to simplify the diagram.
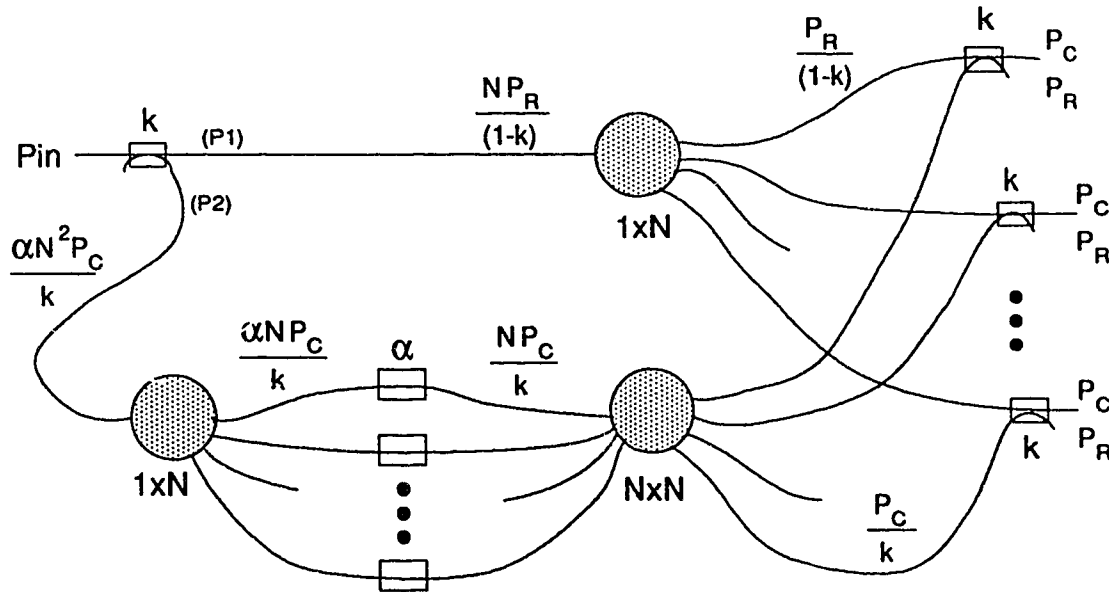

Figure D.1 Theoretical power budget for ERL CM system

The power coupled into the fiber at the head end of the system is denoted by Pin. The power coupling ratio of the first directional coupler at the head end and the receiver couplers is denoted by k. Brooks *et al.* [1] have shown that for an interferometric fiber-optic system involving splitting and recombining of light, the coupling coefficients of the splitting and recombining couplers should be made identical to maximize the power of the final signal. Therefore, the coupling ratio of the head end coupler is made equal to the couplers at the receivers. α is the insertion loss of the A/O modulators (which is assumed to be the same for all modulators) and N is the number of channels supported by the system. From Figure D.1, we can write

$$P1 = (1-k)\,Pin \tag{D.1}$$

and

$$P2 = k\,Pin \tag{D.2}$$

We can also write

$$P1 = \frac{N\,P_R}{(1-k)} \tag{D.3}$$

and

$$P2 = \frac{\alpha\,N^2 P_C}{k} \tag{D.4}$$

Equating (D.1) and (D.3), we have

$$P_R = \frac{(1-k)^2}{N}\,Pin \tag{D.5}$$

and equating (D.2) and (D.4) we have

$$P_C = \frac{k^2}{N^2 \alpha} \, Pin \qquad\qquad (D.6)$$

The ratio of (D.6) to (D.5) gives us the expression for the channel/reference power ratio, Γ:

$$\Gamma = \frac{P_C}{P_R} = \frac{k^2}{(1-k)^2 N \, \alpha} \qquad\qquad (D.7)$$